Evaporation from Nanoporous Membranes for High Heat Flux Thermal Management

by

Daniel Frank Hanks

B.S., Duke University, 2010
S.M., Massachusetts Institute of Technology, 2012

Submitted to the Department of Mechanical Engineering
in partial fulfillment of the requirements for the degree of

Doctor of Philosophy in Mechanical Engineering

at the

MASSACHUSETTS INSTITUTE OF TECHNOLOGY

June 2016

Author ..... Signature redacted
Department of Mechanical Engineering
May 6th, 2016

Certified by ..... Signature redacted
Evelyn N. Wang
Associate Professor of Mechanical Engineering
Thesis Supervisor

Accepted by ..... Signature redacted
Rohan Abyaratne
Chair, Committee on Graduate Students

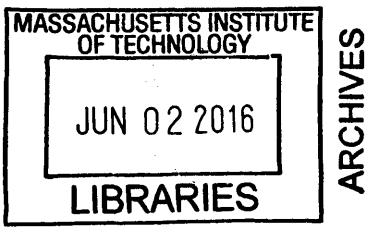

Evaporation from Nanoporous Membranes for High Heat Flux Thermal Management

by

Daniel Frank Hanks

Submitted to the Department of Mechanical Engineering
on May 6th, 2016, in partial fulfillment of the
requirements for the degree of
Doctor of Philosophy in Mechanical Engineering

Abstract

Heat dissipation is a critical limitation in a range of electronic devices including microprocessors, solar cells, laser diodes and power amplifiers. The most demanding devices require dissipation of heat fluxes in excess of 1 kW/cm^2 with heat transfer coefficients more than 30 W/cm^{2}K. Advanced thermal management solutions using phase change heat transfer are the most promising approach to address these challenges, yet current solutions are limited due to the combination of heat flux, thermal resistance, size and flow stability.

This thesis reports the design, fabrication and experimental characterization for an evaporation device with a nanoporous membrane for high heat flux dissipation. Evaporation in the thin film regime is achieved using nanopores with reduced liquid film thicknesses while liquid pumping is enhanced using the capillary pressure of the 120 nm pores. The membrane is mechanically supported by ridges that form liquid supply channels and also serve as a heat conduction path to the evaporating meniscus at the surface of the membrane. The combination of high capillarity pores with high permeability channels facilitates theoretical critical heat fluxes over 2 kW/cm^2 and heat transfer coefficients over 100 W/cm^{2}K.

Proof-of-concept devices were fabricated using a two-wafer stack consisting of a bonded silicon-on-insulator (SOI) wafer to a silicon wafer. Pores with diameters 110 - 130 nm were defined with interference lithography and etched in the SOI. Liquid supply microchannels were etched on a silicon wafer and the two wafers were fusion bonded together to form a monolithic evaporator. Once bonded, the membrane was released by etching through the backside of the SOI. Finally, platinum heaters and Resistive Temperature Detectors (RTDs) were deposited by e-beam evaporation and liftoff to heat the sample and measure the device temperature during experiments, respectively.

Samples were experimentally characterized in a custom environmental chamber for comparison to the model using R245fa, methanol, pentane, water and isopropyl alcohol as working fluids. A comparison of the results with different working fluids demonstrates that transport at the liquid-vapor interface is the dominant thermal resistance in the system, suggesting a figure of merit: $\rho_v h_{fg}\sqrt{RT}$. The highest heat flux recorded was with pentane at q''=518 W/cm^2 at ΔT=28.5 K and the highest heat transfer coefficient recorded was with R245fa at 39.8 W/cm^{2}K not including the substrate resistance. However, the sam-

ples were observed to clog with soluble, nonvolatile contaminants which limited operation to several minutes. The clogging behavior was captured in a mass diffusion model and a new configuration was suggested which is resistant to clogging.

Evaporation from nanopores represents a new paradigm in phase change cooling with a figure of merit that favors high volatility, low surface tension fluids rather than water. The models and experimental results validate the functionality and understanding of the proposed approach and provide recommendations for enhancements in performance and understanding as well as strategies for resistance to clogging. This work demonstrates that nanoporous membranes have the potential for ultra-high heat flux dissipation to address next generation thermal management needs.

Thesis Supervisor: Evelyn N. Wang
Title: Associate Professor of Mechanical Engineering

Acknowledgments

I first thank my adviser, Professor Evelyn Wang, for her persistent support of my research and for stimulating my development as a scientist and engineer. I thank Professor John Brisson for teaching me to approach problems critically, an essential skill for a successful engineer. I also thank Professor Rohit Karnik for important insights and suggestions which guided me through my research. I received exceptional support from the ICECool team of students and postdoctoral researchers regarding the multitude of questions, ideas and debates that arose in my research. In particular, the tireless efforts of Jay Sircar and Zhengmao Lu made the fabrication of devices possible. Dr. Dion Antao was an invaluable resource in construction of the environmental chamber and experimental analysis. I thank Kevin Bagnall for making important contributions with regards to applications and Dr. Banafsheh Barabadi for providing valuable experience in fabrication. Dr. Rishi Raj, Dr. Shankar Naryanan, Dr. Rong Xiao and Dr. Ryan Enright drafted the initial plans for a suspended membrane device and provided mentorship during the early stages of the project. I also thank technicians and staff who were an integral part of fabrication of devices as well as the experimental setup: Dr. Tim Savas and Jim Daley of the NanoStructures Laboratory, Kurt Broderick, Dennis Ward, Bob Bicchieri, Donal Jamieson, Paul Tierney, Bernard Alamariu and Dave Terry of the Microsystems Technology Laboratory, Shiahn Chen and Patrick Boisvert of the Center for Materials Science and Engineering, Andrew Gallant and Scott Spence of Central Machine Shop, Mark Bellanger of the Edgerton Student Shop, Mike Dumaree of the Cryogenics Laboratory and Dr. Ling Xie of the Harvard Center for Nanoscale Systems. I thank my labmates in the Device Research Laboratory for their friendship, technical support and encouragement. I also have tremendous gratitude for my parents who have led by example, set a high standards of achievement and always encouraged me to reach my greatest potential. I thank my wife, Mary, for her patience, especially during the most strenuous phases of my research and for proofreading my thesis. Lastly, I thank the Defense Advanced Research Projects Agency (DARPA) for funding this research through the ICECool Fundamentals program with Dr. Avi Bar-Cohen as program manager.

Contents

List of Figures

List of Tables

Chapter 1

Introduction

1.1 Motivation

Effective heat dissipation has become the primary factor limiting the performance and reliability of high power analog and digital electronics. In particular, gallium-nitride (GaN) semiconductors have reached unprecedented power densities due to advances in material fabrication [1]. The properties of GaN promise improvements across a variety of applications such as wireless communications and radar, particularly for military and aerospace applications [2]. However, due to limited performance of current thermal management solutions, GaN-based high electron mobility transistors (HEMTs) are limited to one tenth of their potential power output to maintain acceptable junction temperatures for device longevity [3]. The thermal challenges arise from the layout and spacial distribution of heat sources: GaN HEMTs exhibit sub-millimeter hot spots in excess of $5\,kW/cm^2$ with background heat fluxes in excess of $1\,kW/cm^2$ over a planar area of 5 to $10\,mm^2$ [4]. A typical layout for a multi-finger GaN HEMT is shown in Figure 1-1a. While the heat flux at the junction may reach 100 kW/cm^2, conduction in a $100\,\mu m$ silicon carbide substrate results in a considerable reduction of the heat flux to 1 kW/cm^2 [5]. Traditional thermal solutions use stacks of highly conductive solid-state thermal spreaders (Cu, CuW, and diamond), thermal interface materials (eutectic solders and filled epoxies) and air-cooled heat sinks or liquid-cooled plates. A simulation of temperature rise and heat flux for a traditional cooling solution [4] is shown in Figure 1-1b. To spur development of practical cooling solutions and realize the electrical potential of GaN electronics, DARPA launched the ICECool (Intrachip/Interchip Enhanced Cooling) program to use a dielectric fluid to dissipate ultra-high heat flux as summarized in Table 1-1 [6, 7]. An intrachip cooling solution refers to a monolithic evaporator and electronic device in which heat is removed at the substrate level rather than from the electronics package, thereby eliminating thermal interface materials. The use of a dielectric fluid is

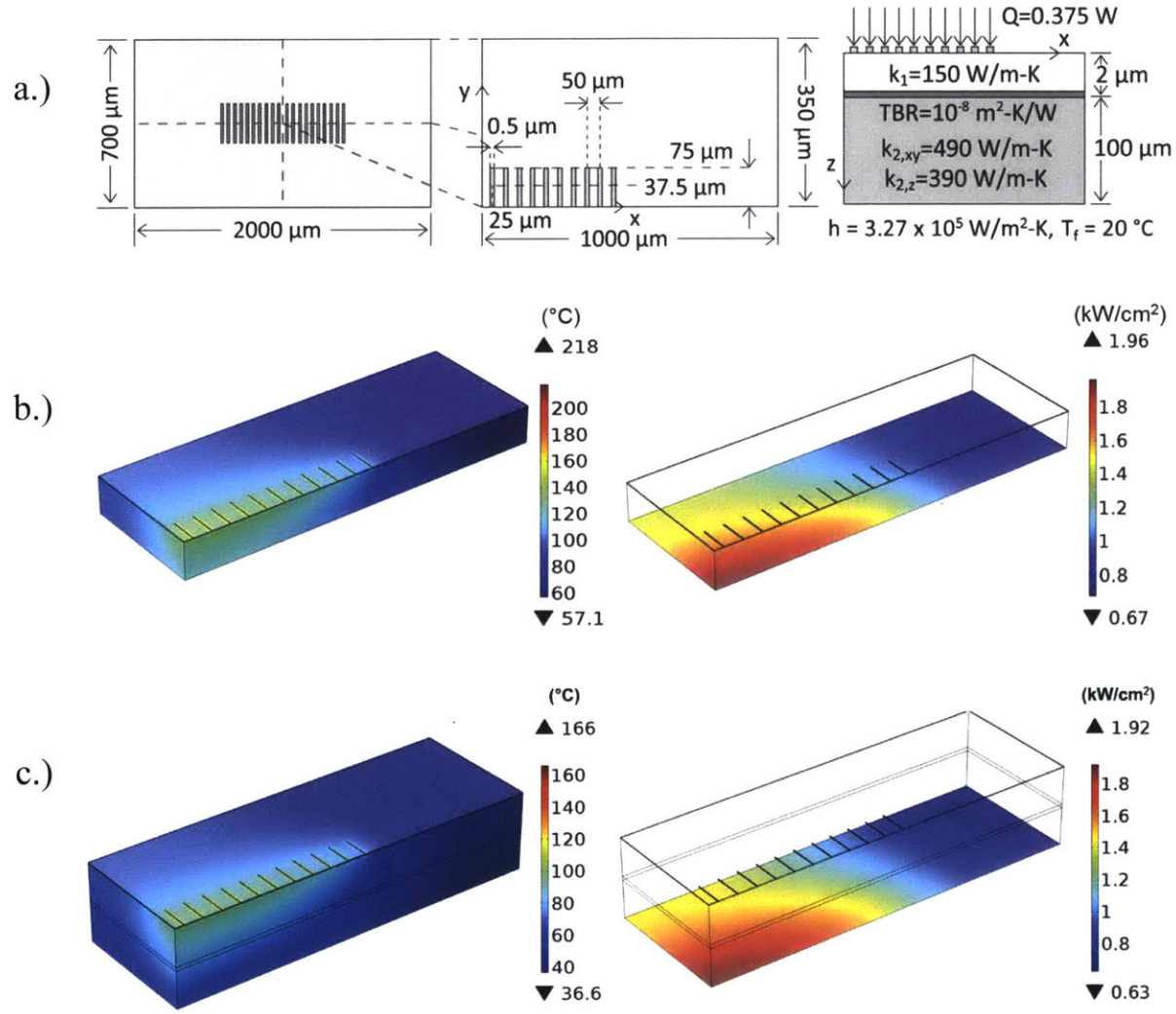

Figure 1-1: a.) Layout of multi-finger GaN HEMT represented by quarter symmetry from [5]. b.) Thermal simulation using traditional SiC heat spreader from [4]. c.) Thermal simulation using monolithic evaporator from [4] resulting in reduction of junction temperature by 42 K.

Table 1-1: DARPA ICECool Fundamentals primary metrics [6]. An evaporation device without boiling will always have a vapor quality of 100%.

Parameter	**Metric**
Vapor quality	>90%
$P_{\text{inlet}} - P_{\text{outlet}}$	$<0.1 \cdot P_{\text{sat}}$
Thermofluidic CoP= $\frac{\dot{Q}}{\dot{W}}$	>30
Heat flux	>1 kW/cm^2
Temperature rise	<30 K
Hot spot flux	>5 kW/cm^2
Hot spot size	200 × 200 µm
Temp. rise of hot spot	<5 K
Reliability	10^4 h

necessary because the flow of a conducting fluid in close proximity to the transistor induces a magnetic field which disrupts electrical device performance. In boiling applications, water typically affords the highest heat transfer coefficient due to its high thermal conductivity since boiling correlations use a Nusselt number to demonstrate that $h \propto k$ [8]. To meet the requirements of Table 1-1 with a dielectric fluid, a new paradigm in thermal management technology is required if phase change heat transfer is to be integrated into the substrate of GaN HEMTs. As shown in Figure 1-1c, computational models predict a 42 K reduction in junction temperature for a heat transfer coefficient of 44 W/cm^{2}K compared to 21 W/cm^{2}K [4]. By absorbing heat only 100 µm from the transistor junction, substantial improvements can be realized in device performance and reliability [5].

1.2 Literature Review

Phase change microfluidic cooling strategies have received significant interest to address the stringent heat flux requirements in high performance systems while significantly reducing size, weight and power. In particular, flow boiling in microchannels has been an active research area [9–15] where typical dissipated heat fluxes of $q'' = 200$ W/cm^2 and heat transfer coefficients of h =10 W/cm^{2}K using water have been demonstrated for exit vapor qualities below 20% [9]. While heat transfer can be improved in the annular flow regime with much

higher exit quality, challenges exist with regards to flow instabilities [10–15]. Despite incorporating surface features and using various water mixtures allowing $q'' = 600$ W/cm^2 and $h = 8.8$ W/cm^{2}K, the performance remains limited by instabilities associated with an increase in fluid density by 1000× during phase change to vapor [16]. The increase in density results in an expanding vapor bubble pushing liquid back out of the inlet, resulting in periodic dryout and large temperature fluctuations. Accordingly, inlet flow restrictors have been proposed which improve stability by distributing flow evenly to multiple channels [17], but lead to significant increases in pumping power requirements. Similarly, single phase cooling has demonstrated $q'' = 790$ W/cm^2 and $h = 11$ W/cm^{2}K in silicon microchannels [18], but the pumping power requirements are impractically high.

Recent developments in passive capillary-pumped vapor chambers and heat pipes have utilized micro/nano-structured wicks, including sintered copper mesh coated with carbon nanotubes [19], titanium nanopillars [20], and oxidized copper microposts [21], to develop high flux evaporators. The performance of such wick geometries is related to the coupling between the capillary pressure and the viscous pressure. The capillary pressure generated by the wick scales as $\Delta P \propto r^{-1}$ according to the Young-Laplace equation where r is the characteristic pore size. Meanwhile, the viscous resistance to liquid transport through the wick scales as $\Delta P \propto r^{-2}$ according to the Darcy-Weisbach equation. The highest critical heat flux (CHF) for wicks with an even distribution of particle sizes is ~500 W/cm^2 using water with 250 - 355 µm particles achieved during nucleate boiling in the wicking structure, but less than 100 W/cm^2 achieved in pure evaporation [22], *i.e.* without nucleate boiling. Since the viscous resistance is proportional to the wicking length, higher CHF values can be achieved with smaller evaporation areas. A study of boiling in ultra-thin (40 µm) inverse opal copper wicks reported 1200 W/cm^2 over an area 0.3 × 2 mm [23]. To reduce the viscous resistance within the wick over larger areas, liquid supply arteries [24] and bi-porosity [25, 26] have been introduced, resulting in $q'' = 600$ W/cm^2 and $h = 20$ W/cm^{2}K over 1 × 1 cm [24]. While increasing the height of the wick structure improves liquid transport for reaching higher critical heat flux, it also increases the thermal resistance of the evaporator. However, the maximum permissible temperature difference in electronics thermal management is effectively fixed due to constraints on the maximum junction temperature and the minimum available ambient temperature. Thus, increasing heat fluxes needs to be addressed with a linearly proportional increase in heat transfer coefficients. In two-phase systems typified by very efficient vapor transport of energy, heat transfer coefficients depend, to a large extent, on the heat conduction characteristics from the substrate to the liquid-vapor interface. This, for example, explains the improved thermal performance of nucleate boiling that occurs in a sintered wick [22] or of the annular flow regime in flow boiling [27].

Evaporation from nanopores has been suggested in previous work for improving both

critical heat flux and heat transfer coefficients. Xiao *et al.* demonstrated sustained negative liquid pressures in alumina membranes with a thickness of 50-100 µm and pores with diameter of 150 nm during evaporation with isopropyl alcohol [28]. Using these experimental results, a theoretical interfacial heat flux of 5 kW/cm^2 was predicted for membranes only 1 µm thick. Narayanan *et al.* demonstrated heat dissipation of 600 W/cm^2 for 1 mm^2 hot spots using 50-100 nm pores in a 60 µm thick alumina membrane and FC-72 as the working fluid. However, the configuration required heat conduction through a continuous liquid layer thus limiting the heat transfer coefficient, and relied on active pumping, instead of capillarity alone, to deliver liquid to the backside of the membrane. Additionally, the vapor transport from the liquid-vapor interface was carried out using advection driven by dry air.

The aforementioned performance requirements suggest the following criteria for a high performance evaporator device: 1) a low conduction resistance layer from the substrate to the liquid-vapor interface, 2) the ability to generate large capillary pressures to supply the requisite liquid for evaporation, 3) an efficient liquid supply architecture that minimizes pressure drop and 4) effective vapor transport from the liquid-vapor interface.

1.3 Description of the System

This thesis presents a membrane-based evaporation approach to high flux thermal management, for dissipating $q'' > 1$ kW/cm^2 with $h > 50$ kW/cm^{2}K and CoP > 100. The CoP is defined as the heat dissipated by the device divided by the work supplied, in this case by liquid pumping. As shown in the cross-sectional schematic of Figure 1-2, liquid enters the device manifold which distributes flow through microchannels. Some liquid bypasses the device while some liquid is drawn into ridge microchannels by the capillarity of membrane pores where it evaporates from the nanoporous membrane surface. Heat is absorbed from the bottom of the device and provides the energy for capillary pumping. The schematic in Figure 1-2 shows two vapor channels and three manifold channels although a larger array of n vapor channels and $n + 1$ manifold channels be arranged to dissipate heat over a larger area.

The proposed concept offers several advantages: the device architecture leverages a thin (~600 nm) nanoporous membrane bonded to a high permeability support structure to decouple the heat dissipation from the pressure drop of the device. With pores of 120 nm diameter, high capillary pressures can be generated even with dielectric liquids to achieve mass flow rates necessary for high flux evaporation. An external pump can drive flow through relatively large manifold channels (100 µm) while the capillary pressure of the pores passively provides much higher pumping power through much smaller ridge channels (2 µm). The fluidic delivery to the evaporative region from the inlet microchannels is self-regulated by the

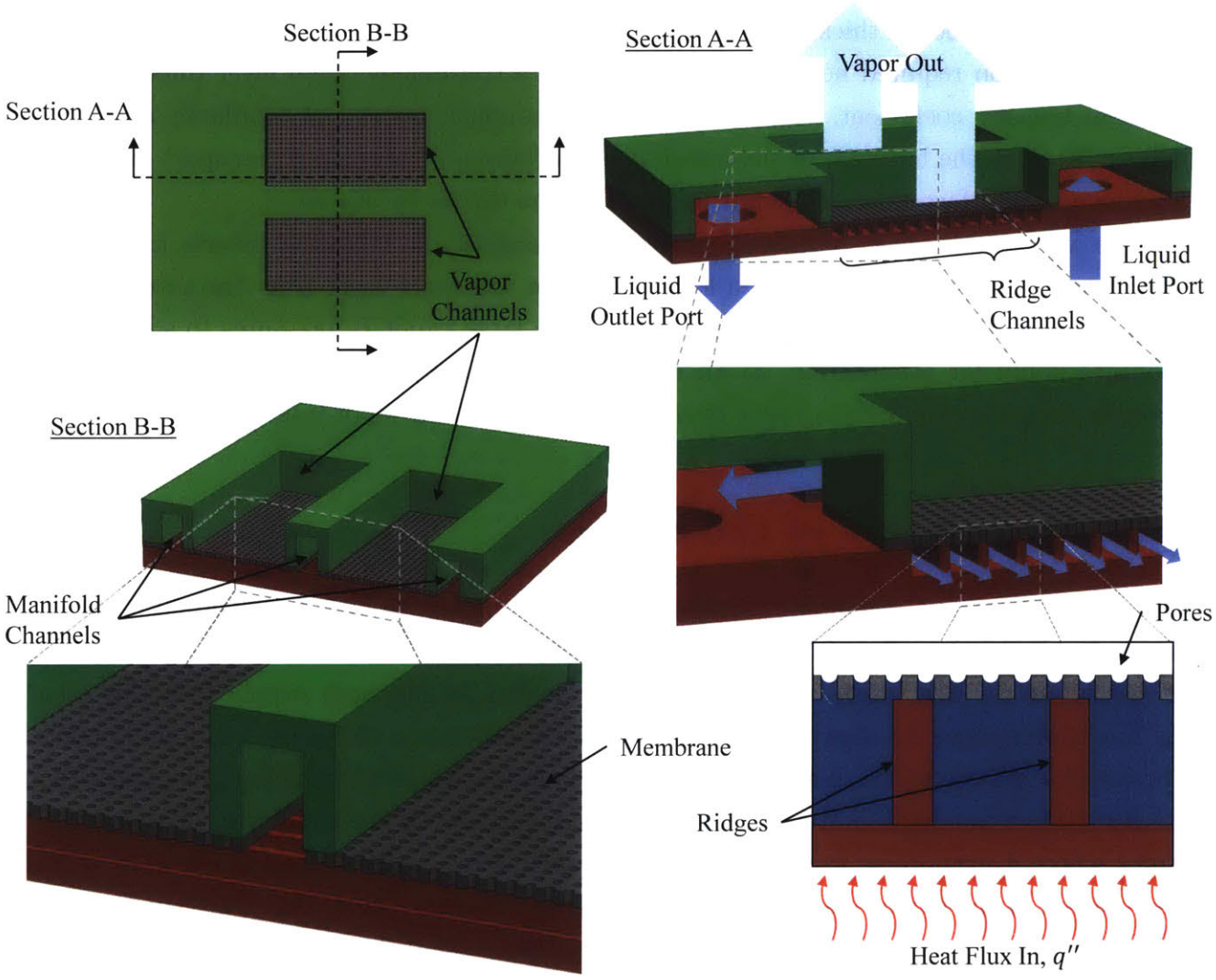

Figure 1-2: Schematic of nanoporous evaporation device: liquid entering the device flows through manifold channels (green structure) which are connected to ridge channels. Liquid is then distributed into ridge channels (red structure) which supply liquid to membrane pores.

capillarity of the membrane and eliminates the need for additional fluidic valves and active control on the chip. Parallel ridges provide both mechanical support for the nanoporous membranes and enhanced thermal conductivity to minimize the thermal resistance between the chip substrate and evaporation region. In addition, reduction in the meniscus size to 100 nm virtually eliminates liquid conduction resistance from the pore wall to the evaporating meniscus. In a macro-sized meniscus, *e.g.,* a bubble with diameter 10 µm - 10 mm, the highest rates of evaporation occur around the liquid-solid-vapor contact line, an area labeled as the thin film region. It is estimated that half of the interfacial flux occurs when the liquid film is about 0.5 µm [29]. By steadily evaporating liquid from pores that are smaller than the thickness of the thin film region, high heat transfer coefficients can be sustained. Furthermore, the implementation of nanopores generates enough capillary pressure to support low surface tension fluids. The interfacial resistance is dependent the volatility of a fluid which is a function of the fluid properties and temperature. High volatility liquids have lower interfacial resistance compared to water, but lower surface tension. Therefore, evaporation from nanopores permits the use of fluids with low surface tension and low interfacial resistance. The combined heat transfer coefficient of the membrane, supported ridge, liquid meniscus and interface can be as high as 50 W/cm^2K, one order of magnitude higher than any state-of-the-art two-phase cooling solution. Furthermore, the overall design can be easily scaled to larger areas by making use of an array of membranes to tackle thermal management needs of multiple devices on the same substrate.

This thesis presents a detailed study of a novel evaporator for a two-phase thermal management solution. A complete thermodynamic cooling cycle, however, involves condensation of the vapor exiting the evaporator and recirculation of the liquid back into the evaporator shown in Figure 1-3 with two variations. While the evaporator must accept heat over small areas (10 - 100 mm^2) at heat high flux, the condenser can be sized much larger (10^3 - 10^5 mm^2) to reject heat at lower heat flux [30]. In Figure 1-3a, the evaporator is combined with a much larger condenser since heat transfer coefficients for air cooling are much lower than evaporation. In Figure 1-3b, the evaporator is combined with a vapor compression cycle which results in a higher temperature in the condenser, allowing the condenser to be much smaller. An evaporator with a perfect exit vapor quality ($x = 1$) is well-suited for integration with a vapor compression cycle compared to an evaporator with flow boiling and low exit vapor quality ($x < 1$). An evaporator with $x < 1$ requires a phase separator or two-phase compressor for the liquid-vapor outlet flow which is impractical [31]. Ultimately, the choice of loop configuration depends on the application requirements. A nanoporous membrane evaporation device is compatible with many loop configurations for thermal management of high power electronics.

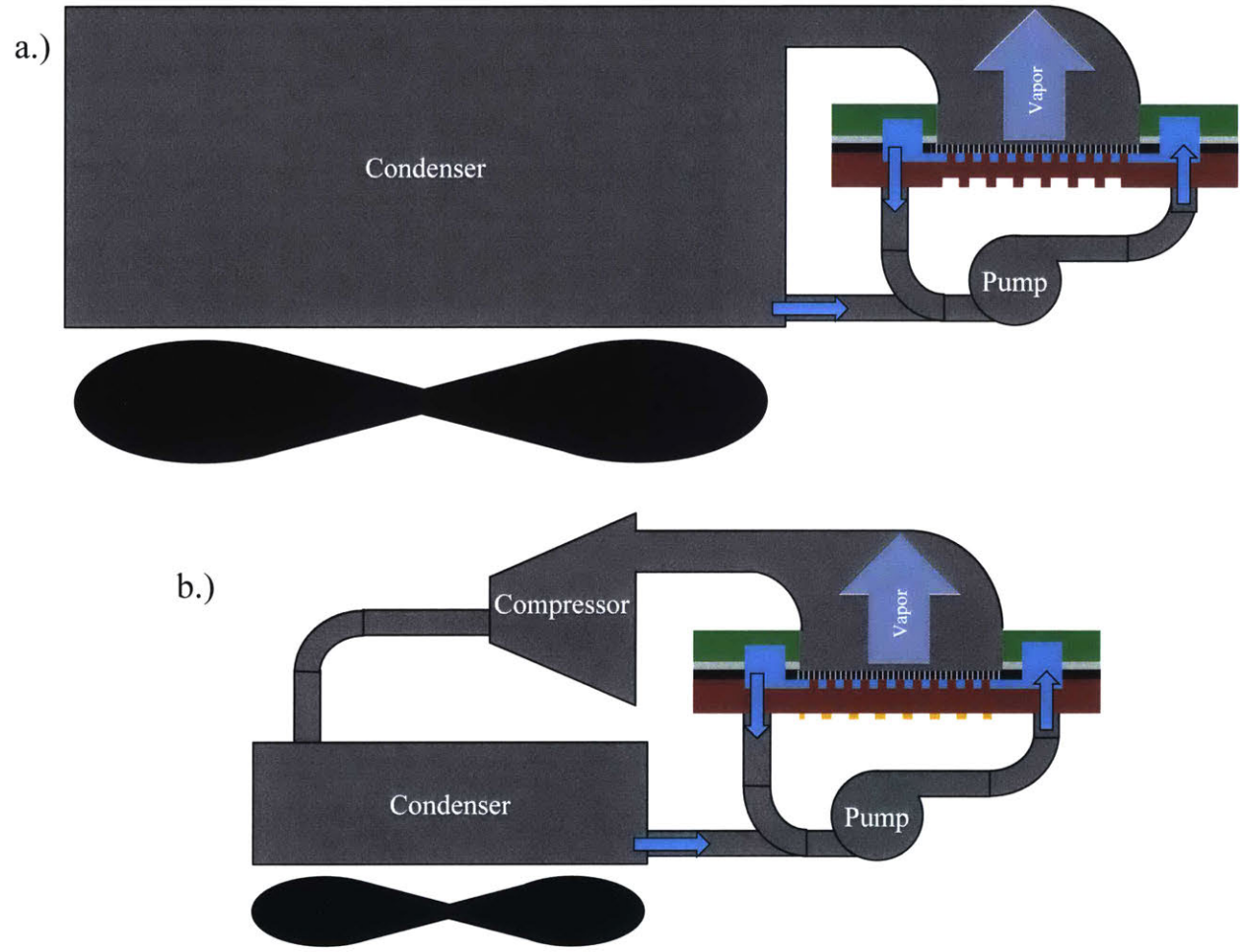

Figure 1-3: Two options for integration into a test loop, which is omitted from this study: a.) Evaporator, condenser and pump in loop. The condenser can be air or liquid cooled and can be arbitrarily sized depending on the system constraints on size, weight and power. b.) A more compact loop includes an evaporator, pump, compressor and a smaller condenser. This approach uses more energy to drive the compressor, but the fan and condenser can be much smaller because the condenser temperature will be higher.

1.4 Thesis Overview

The focus of this thesis is to design, fabricate and experimentally characterize an evaporation device with a nanoporous membrane and identify the impact of its performance for high power electronics cooling. Chapter 1 has introduced the motivation behind a nanoporous evaporation device in the context of past research in phase change cooling. Next, Chapter 2 describes models developed to predict the critical heat flux and heat transfer coefficient which advise the selection of geometries for the membrane structure. Chapter 3 details the procedure used to fabricate prototype devices in the clean room using photolithography, reactive ion etching, wafer bonding and metal deposition. Chapter 4 includes details of the experimental setup, methodology, results and analysis used to understand the physics of evaporation with fabricated samples. Finally, Chapter 5 summarizes the impacts of evaporation from nanoporous membranes and provides suggestions for future work to improve performance and understanding.

Chapter 2

Modeling

The modeling is separated into two components: a hydrodynamic model to predict critical heat flux and a thermal model to predict overall heat transfer coefficient. Each component of the model guides the selection of a working fluid and device geometries including pore size, membrane thickness, ridge channel size and manifold size.

2.1 Hydrodynamic Model

Capillary pumped evaporation structures reach a critical heat flux upon dryout. This process occurs when viscous pressure resistance overcomes the capillary pumping potential which leads to the wick drying out. Therefore, an analytical flow model is used to calculate the viscous pressure drop in each channel of the device and compare it to the capillary pressure of the pores. The flow regime in the pore, ridge and manifold channels depends on the Reynolds number. Assuming a uniform heat flux of $q'' = 1000\,\mathrm{W/cm^2}$, the Reynolds number is calculated for each channel in the fluidic supply network: liquid flow through the pores with diameters of 120 nm and length 600 nm, through the ridge channels which have a cross-section of $2\,\mu\mathrm{m} \times 2\,\mu\mathrm{m}$ and a length of $100\,\mu\mathrm{m}$ and through the larger liquid manifold channels with a cross-section of $100\,\mu\mathrm{m} \times 100\,\mu\mathrm{m}$ which extend 10 mm in length. The pressure drop for fully-developed laminar flow in a circular and square channel can be calculated from the Hagan-Poiseuille equation for Re<2300:

$$\left.\frac{\partial P}{\partial x}\right|_{\mathrm{cir}} = \frac{128\mu\dot{m}}{\pi\rho_L d^4} \tag{2.1}$$

$$\left.\frac{\partial P}{\partial x}\right|_{\mathrm{sq}} = 28.4\frac{\mu\dot{m}}{\rho_L w^4} \tag{2.2}$$

Table 2-1: Summary of liquid pressure drop in pores, ridge and manifold channels using fluid properties at 50 °C and assuming no bypass flow through outlet.

			Water, 1000 W/cm^2		**Pentane, 1000 W/cm^2**	
Channel	**Length**	**Cross-section**	**Velocity**	**ΔP [MPa]**	**Velocity**	**ΔP [MPa]**
Manifold	10 mm	100 µm × 100 µm	0.38 m/s	2.1 kPa	2.6 m/s	4.6 kPa
Ridge	200 µm	2 µm × 2 µm	0.12 m/s	147 kPa	0.84m/s	329 kPa
Pore	700 nm	d_p = 120 nm	0.012 m/s	18 kPa	0.086 m/s	41 kPa

where P is the pressure, μ is the liquid viscosity, $\dot{m}$ is the mass flow rate, x is the distance along the channel, ρ_L is the liquid density, d is the diameter of the pore, and w is the width of the channel. The mass flow rate in the manifold and ridge channels decreases linearly as a function of x as liquid is siphoned into the ridge and pores, respectively. The expressions in Equation 2.1 and Equation 2.2 are then integrated to calculate the total pressure drop in the channel.

$$\dot{m}_{\text{pore}} = \frac{\pi q'' d^2}{4\phi h_{fg}} \text{ with } \phi = \frac{\pi d^2}{4p^2} \tag{2.3}$$

$$\int dP_{\text{pore}} = \int_0^t \frac{128\mu}{\pi \rho_L d^4} \frac{\pi q'' d^2}{4\phi h_{fg}} dx \tag{2.4}$$

$$\Delta P_{\text{pore}} = \frac{32\mu q'' t}{\rho_L \phi h_{fg} d^2} \tag{2.5}$$

$$\dot{m}_{\text{ridge}}(x) = \frac{q'' w(L/2 - x)}{h_{fg}} \tag{2.6}$$

$$\int dP_{\text{ridge}}(x) = \int_0^{L/2} 28.4 \frac{\mu q'' w(L/2 - x)}{\rho_L h_{fg} w^4} dx \tag{2.7}$$

$$\Delta P_{\text{ridge}} = 3.6 \frac{\mu q'' L^2}{\rho_L h_{fg} w^3} \tag{2.8}$$

where ϕ is the porosity of the membrane, p is the pore pitch, t is the thickness of the membrane, h_{fg} is the latent heat of vaporization, L is the length of the ridge channel which has a liquid inlet on each end, therefore the flow length is $L/2$. The viscous pressure drop for each channel is summarized in Table 2-1. Pentane and water were evaluated as candidate fluids

whose performance will be investigated in depth along with isopropyl alcohol, methanol and R245fa in Section 2.2. These fluids represent a large variation in thermophysical properties including surface tension, vapor pressure, latent heat capacity and viscosity. To avoid dry-out, the device was designed such that the viscous pressure loss through the pore and ridge channels is less than the maximum capillary pressure. For a hemispherical liquid meniscus in a pore, the maximum capillary pressure can be calculated by the Young-Laplace equation:

$$\Delta P_{\text{cap}} = \frac{2\sigma \cos(\theta)}{r} \tag{2.9}$$

where σ is the surface tension, r is the pore radius and θ is the contact angle. The contact angle of water on silicon with native oxide is $\theta \approx 45°$ [32] while the contact angle of most low surface tension fluids on silicon with native oxide is $\theta \leq 10°$ [33]. The maximum capillary pressure of pentane in a 120 nm diameter pore is 670 kPa, while the pressure drop for the pore and ridge channels is 370 kPa using liquid properties at 50 °C and a heat flux of 1000 W/cm^2. An illustrative plot of pressure along a streamwise coordinate in the device is shown in Figure 2-1. Although there is a potential for the liquid to reach negative pressure, *i.e.* the liquid is in tension, there are many examples of stable liquids at negative absolute pressure including engineering [28] and in nature [34]. Experimental studies have indirectly measured liquid pressure lower than -10 MPa using water [35].

At the liquid-vapor interface, the liquid is near saturation conditions. Since the capillary pressure at the meniscus allows the liquid pressure to drop relative to the ambient vapor pressure, the liquid is supersaturated (metastable), but will not boil or cavitate unless the superheat is high enough to initiate nucleation [36]. The existence of metastable liquid is a commonality of all heat pipe wicks. Sustained boiling is observed in heat pipe wicks above ~100 W/cm^2 at a superheat of ~5 K [22]. After a transition to boiling, the heat transfer coefficient in sintered copper wicks is observed to increase and boiling is sustained until dryout above 500 W/cm^2. In the suspended membrane presented here, however, the capillarity to stabilize the liquid at large interfacial pressures is only guaranteed when the liquid is pinned at the pores. If boiling is initiated inside the ridge channels, the structure is not expected to sustain boiling as in the case of heat pipes with uniform pore distribution. Therefore, it is important to prevent nucleation in the membrane and ridge channels to ensure continuous liquid supply and stable evaporation at the membrane surface. Nucleation begins at microscopic defect sites on a heated surface which trap air and create a liquid-gas interface for a bubble to grow. For this reason, smooth channel walls and low dissolved gas concentration is desired to deter nucleation in the ridge channels.

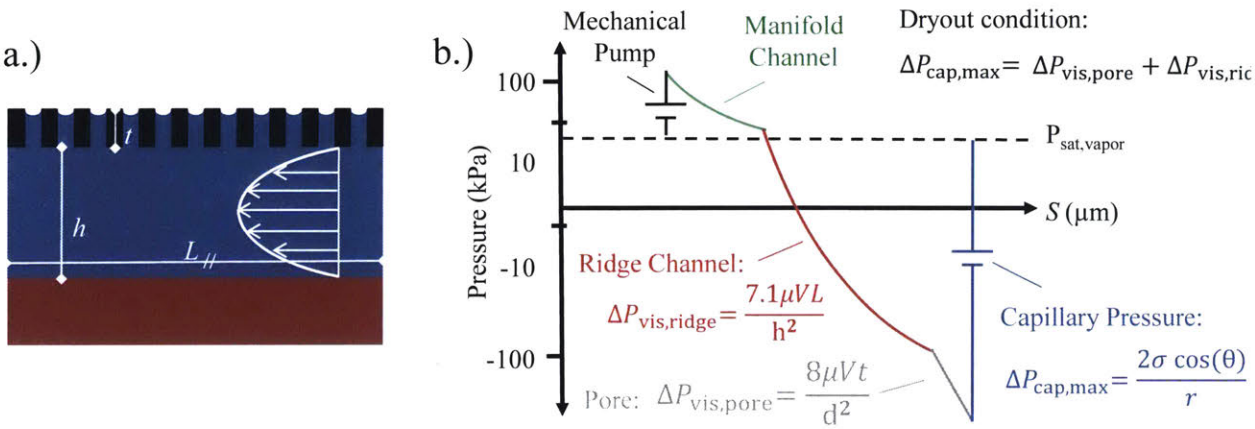

Figure 2-1: a.) Liquid flow in the manifold, ridge channels and pores is laminar, so the pressure drop can be estimated analytically. b.) Schematic of pressure drop along a streamwise coordinate, S: The pressure liquid is driven by an external pump into the manifold, but the liquid flow in the ridge by is driven by capillary pumping at the membrane pores. If the pressure drop is high enough, liquid in the ridges and pores can drop below zero, *i.e.* the liquid is in tension and metastable.

Optimization of Pore Size

Using the hydrodynamic model, a local optimizaiton of pore size can elucidate the benefits of small pores. Equations 2.1 - 2.9 can be combined to predict the dryout heat flux as a function of pore radius:

$$\Delta P_{\text{cap}} = \Delta P_{\text{ridge}} + \Delta P_{\text{pore}} \tag{2.10}$$

$$\frac{2\sigma \cos(\theta)}{r} = 3.6\frac{\mu q'' L^2}{\rho h_{fg} w^3} + \frac{8\mu q'' t}{\rho \phi h_{fg} r^2} \tag{2.11}$$

$$q'' = \frac{2\rho h_{fg}\sigma \cos(\theta)}{\mu}\left(\frac{1}{r}\right)\left(\frac{\phi r^2 w^3}{3.6\phi r^2 + 32 t w^3}\right) \tag{2.12}$$

Setting the partial derivative of heat flux with respect to radius equal to zero, the optimum pore size can be calculated:

$$\frac{\partial q''}{\partial r} = 0 \tag{2.13}$$

$$0 = (3.6L^2\phi r^2 + 32tw^3)(\phi w^3) - (\phi r w^3)(7.1L^2\phi r)$$

$$r = 9.0\frac{tw^2}{L^2\phi} \tag{2.14}$$

$$q''_{\max} = \frac{\rho h_{fg}\sigma\cos(\theta)}{\mu}\left(\frac{5.1w^2\phi}{tw + 9.0\phi L^2}\right) \tag{2.15}$$

The optimization of pore radius, r, leads to practical insights: first, the optimum pore size for maximizing q''_{CHF} is independent of fluid properties. Second, at small r, flow in the pore dominates the overall pressure drop while at larger r, flow in the ridge channel dominates the overall pressure drop. A simulation of critical heat flux as a function of pore size and working fluid based on Equation 2.12 is shown in Figure 2-2 for fluid properties taken at 50 °C and using the ridge geometry specified in Table 2-1. The porosity is fixed at $\phi = 0.372$, therefore the pore pitch scales with the pore diameter. The simulation suggests that water has the highest critical heat flux of any fluid, with heat fluxes above 1 kW/cm^2 also possible with pentane and R245fa when the pore diameter is 34 nm. However, dryout is only one limitation to reaching high heat flux. As shown in the Section 2.2, the temperature rise for water over 30 kW/cm^2 is near the critical point where surface tension and latent heat diminish to zero in contrast to the temperature rise for pentane and R245fa which is much lower. A group of fluid properties can be separated from the geometrical parameters in Equation 2.12. This group has been identified as a figure of merit for fluid selection in heat pipes [37]:

$$M_1 = \frac{\rho_L h_{fg}\sigma\cos(\theta)}{\mu} \tag{2.16}$$

As a result, water is typically the working fluid of choice for heat pipes and vapor chambers, due primarily to its high latent heat and surface tension.

Curvature Pressure

An important limitation to pore size arises from the change in Gibbs free energy associated with a curved surface. The energy to create a curved surface results in a lower vapor pressure at a concave interface and a higher vapor pressure at a convex interface. The Kelvin equation can be used to describe the change in vapor pressure, P_v, above a curved interface relative

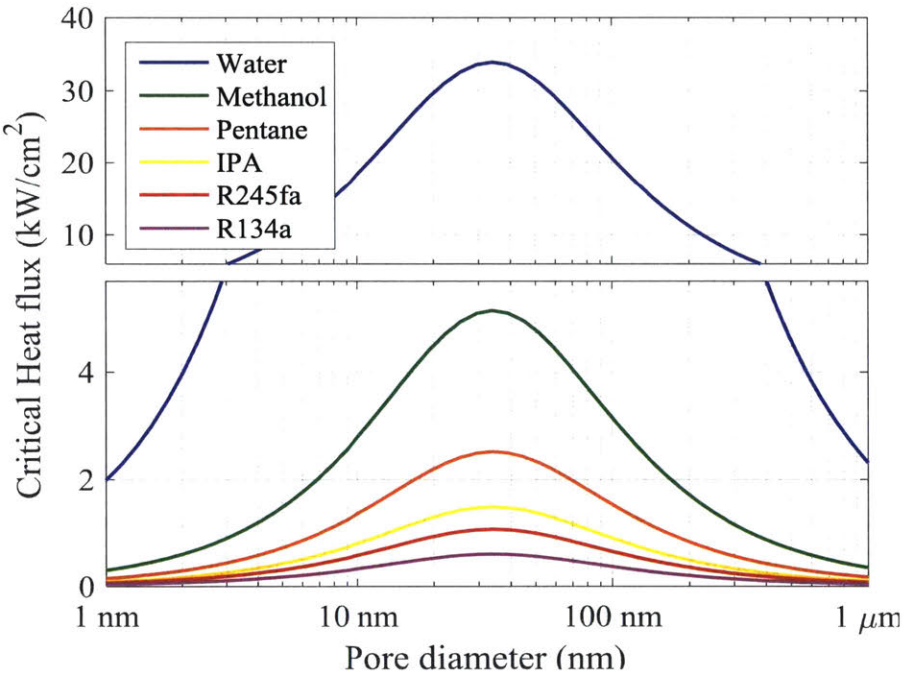

Figure 2-2: For a fixed liquid ridge channel 2 µm wide, 2 µm high and 200 µm long, there exists an optimum pore size for maximizing critical heat flux for various fluids of interest. For this simulation, the porosity was fixed at $\phi = 0.372$, therefore the pore pitch increases linearly with pore diameter. Isopropyl alcohol is abbreviated "IPA".

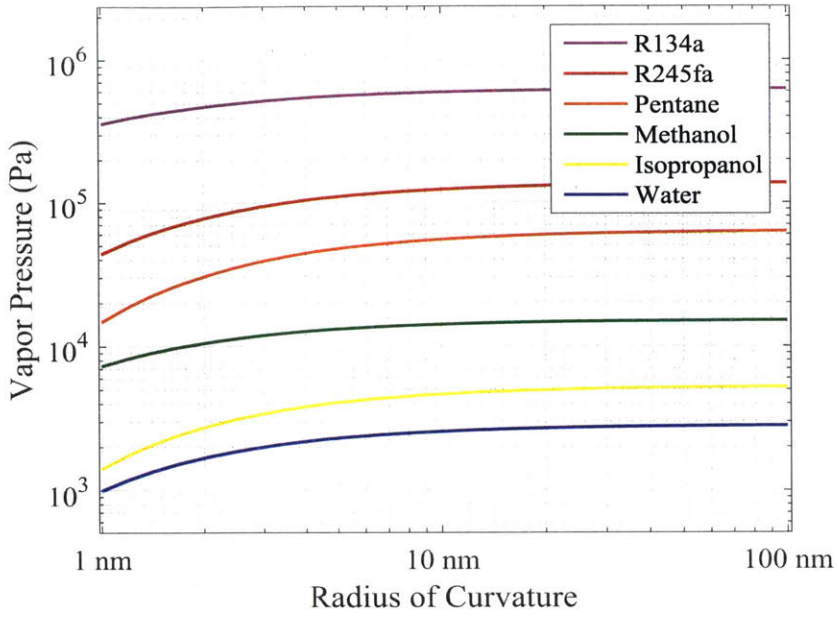

Figure 2-3: For a capillary radius below 10 nm, the reduction in vapor pressure due to curvature cannot be neglected.

to the saturation vapor pressure, P_{sat}, for a flat interface:

$$\frac{P_v}{P_{\text{sat}}} = \exp\left(-\frac{2\sigma V_m}{rRT}\right) \tag{2.17}$$

where V_m is the molar volume of the liquid, r is the radius of curvature and R is the ideal gas constant. The change in vapor pressure for a range of capillary radius from 1 nm - 100 nm is shown in Figure 2-3. For a pore with 100 nm diameter ($r = 50$ nm), the vapor pressure is reduced by only 1 - 3%. For a pore with 10 nm diameter ($r = 5$ nm), the vapor pressure is reduced by a considerable 11 - 23%.

2.2 Thermal Model

While the hydrodynamic model predicts the CHF due to dryout, the overall heat transfer coefficient depends on conduction through the membrane structure and liquid film as well as the interfacial resistance. The temperature rise of the substrate with uniform heat flux was modeled using COMSOL Multiphysics finite element analysis to predict the overall heat transfer coefficient [4]. Due to the symmetry of the structure, the problem can be reduced to a control volume which contains the ridge, ridge channel and membrane as shown in Figure 2-4. Heat convection and conduction in the liquid is insignificant compared to conduction in

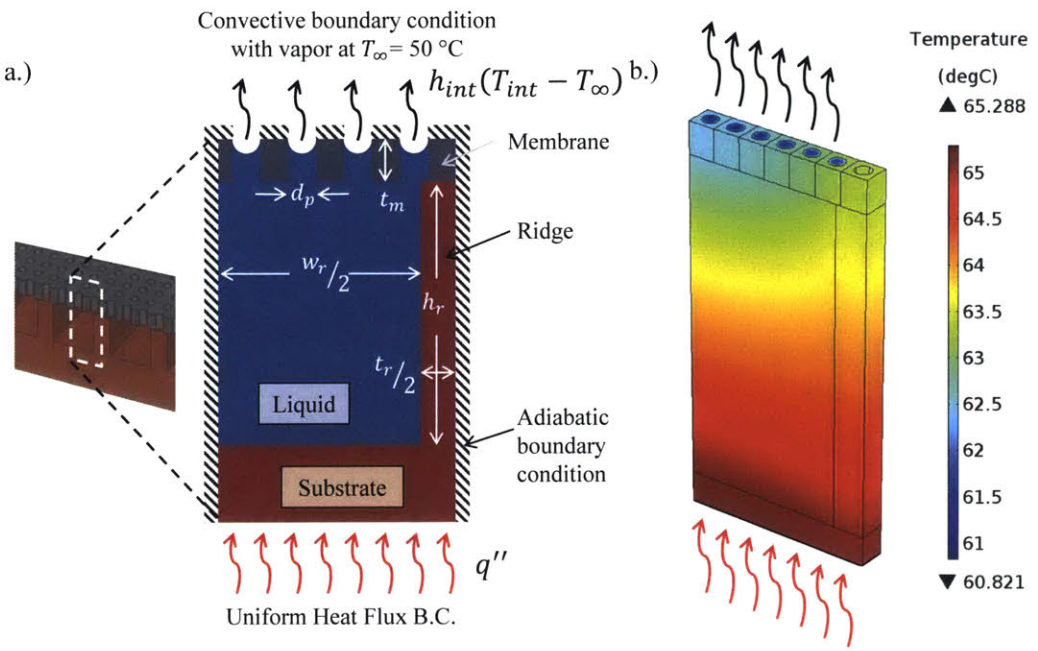

Figure 2-4: a.) Thermal model domain for predicting overall heat transfer coefficient. Only half of the ridge channel and half of the membrane span are considered due to symmetry. b.) Temperature plot of unit cell reveals that the ridge, membrane, liquid and interface each represent a significant thermal resistance.

the ridge. Therefore, any cross-section along the length of the ridge is assumed to have the same temperature profile and it can be assumed that the front and back faces are adiabatic. The left and right faces are adiabatic to represent mirrored conditions while the front and back faces are adiabatic to represent repeating boundary conditions. Sensible cooling effects are not considered because the thermal entry length is small ($\sim 10\,\mu$m) relative to the total length of the channel. Thermal conductivity values of silicon were assumed equal to bulk values, k=130 W/m-K, except in the ridge and membrane where values of k=39.2 W/m-K and k=18.2 W/m-K were applied, respectively, to reflect non-continuum heat transfer due to scattering of phonons in microstructures [38–40].

The heat transfer coefficient at the liquid-vapor interface was modeled by solving the Boltzman transport equation using a method by Labuntsov and Kryukov [41] and appling it to the pore geometry using a method by Lu, *et al.* [42]. Using this approach, the model captures sub-continuum effects in the vapor phase due to Knudsen flow and captures non-equilibrium effects due to deviation from classical kinetic theory. The accommodation coefficient, $\hat{\sigma}$, is an input to the interfacial transport model and represents the probability of a liquid molecule escaping into the vapor phase when it has sufficient energy. The accommodation coefficient for most nonpolar fluids is $\hat{\sigma} = 1$, however values reported for water range

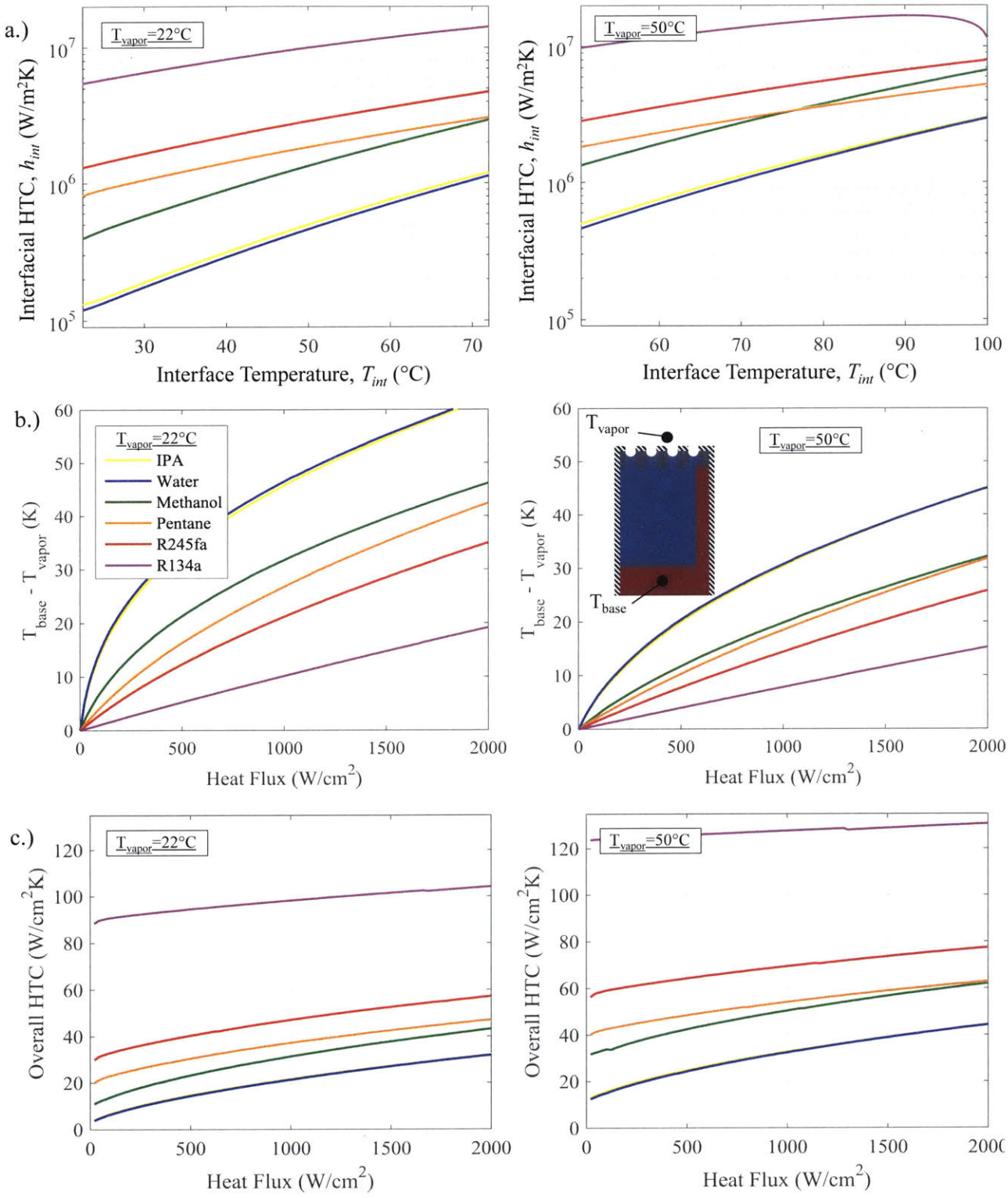

Figure 2-5: a.) Interfacial heat transfer coefficient used as a boundary condition for the finite element model at $T_v = 22\,^{\circ}\mathrm{C}$ and $T_v = 50\,^{\circ}\mathrm{C}$. b.) Model predictions for temperature rise as a function of heat flux at $T_v = 22\,^{\circ}\mathrm{C}$ and $T_v = 50\,^{\circ}\mathrm{C}$. c.) Overall heat transfer coefficient including resistance in ridge, membrane, liquid film and interface at $T_v = 22\,^{\circ}\mathrm{C}$ and $T_v = 50\,^{\circ}\mathrm{C}$. Plots b. and c. assume $d_{\mathrm{pore}} = 130$ nm, $\phi = 0.3318$, $h_{\mathrm{ridge}} = 2\,\mu\mathrm{m}$ and $t_{\mathrm{mem}} = 600$ nm. Isopropyl alcohol is abbreviated "IPA".

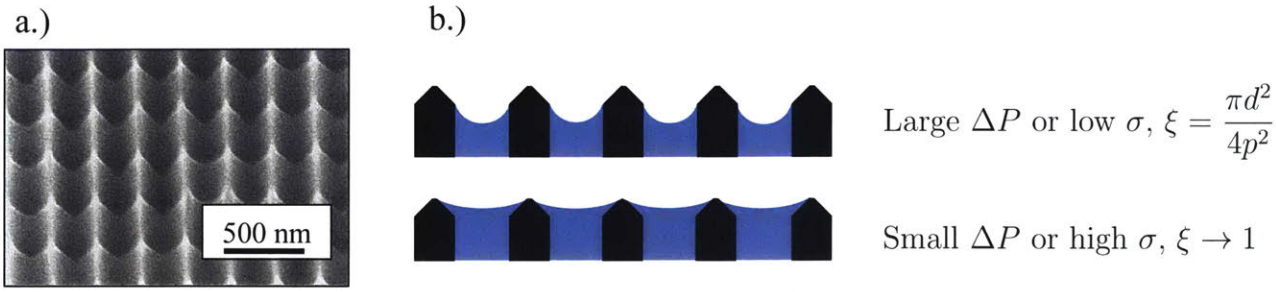

Figure 2-6: The wetting morphology of liquid at the membrane pores can have a large impact on the heat transfer coefficient. a.) a SEM image with 45° tilt shows the uneven membrane surface. b.) The limiting cases of the liquid area fraction are shown schematically.

from 0.02 to 1.0 [43]. Due to the controversy in the literature regarding the accommodation coefficient, especially with water, all models used $\hat{\sigma} = 1$. The interfacial heat transfer coefficient is plotted in Figure 2-5a for six working fluids at $T_v = 22\,°\text{C}$ and $T_v = 50\,°\text{C}$. The trend for all fluids rises with temperature as the saturation vapor pressure increases, with the exception of R134a which approaches its critical point $T_c = 101\,°\text{C}$. Both the temperature and choice of working fluid have a major impact on the interfacial heat transfer coefficient which is summarized by a second figure of merit identified by Lu, *et al.* [4] which suggests that the rate of heat transfer at the interface is proportional to the flux of molecules leaving the interface times the energy per molecule:

$$M_2 = \rho_v h_{fg} \sqrt{RT} \tag{2.18}$$

In previous evaporation structures, the conductivity of the liquid or solid structure was the primary thermal resistance. However, evaporation from nanopores enters a new regime in which the solid and liquid conduction resistances are small compared to the interfacial resistance.

The results of the complete thermal model are plotted in Figure 2-5b for water, isopropanol, methanol, pentane, R245fa and R134a for a structure with $h = 2\,\mu\text{m}$, $d_p = 130\,\text{nm}$, $t_m = 0.7\,\mu\text{m}$ and $T_v = 22\,°\text{C}$. The choice of working fluid has a strong impact on the overall thermal resistance of the device because the interfacial resistance is large relative to the conduction resistance in the ridge, membrane and liquid meniscus. Since the interfacial resistance accounts for 80 - 94 % of the total thermal resistance depending on the fluid, the wetting morphology of liquid at the membrane surface can have a large impact: if the pore walls are rounded as shown in Figure 2-6, the liquid may spread and the effective area fraction of liquid will be larger than the porosity as measured by the pore diameter. While the actual effective area fraction of liquid depends on the complex shape of pores, the upper bound is $\xi = 1$ and the lower bound is $\xi = \phi$. These limiting cases are plotted with

experimental results in Chapter 4.

The overall heat transfer coefficient of the evaporator, *i.e.* the heat flux divided by the tempertaure rise, is shown in Figure 2-5c and 2-5d. This metric is most useful for an electronic packaging engineer to determine the junction temperature rise with a monolithic evaporator device as modeled in Figure 1-1b.

Selection of Working Fluid

The fluids with the highest q''_{CHF} typically have the lowest interfacial heat transfer coefficient, as in the case with water. Conversely, the fluids with the highest interfacial heat transfer coefficient typically have the lowest q''_{CHF}. In general, this is because high molecular attraction leads to high surface tension and low volatility. High surface tension is necessary for high q''_{CHF} while high volatility promotes low interfacial resistance. A plot of 15 candidate working fluids is shown in Figure 2-7 with each fluid normalized by the figures of merit for water. Dielectric fluids are indicated with black markers and text while conducting fluids are indicated with gray. The figure of merit for maximizing q''_{CHF} comes from Equation 2.12 while the figure of merit for maximizing the interfacial heat transfer coefficient, h_{int}, is shown in Equation 2.18. From the assortment of 15 fluids in Figure 2-7, six fluids were selected for analysis which span a large range of properties: water, isopropyl alcohol, methanol, pentane, R245fa and R134a. Water and methanol are not dielectric liquids, but their unique properties demonstrate the range of performance that can be expected from nanoporous membrane evaporation. All of these fluids are investigated experimentally with the exception of R134a which operates at higher vapor pressure than the experimental apparatus can accommodate.

Among the fluids investigated experimentally, pentane, methanol and isopropyl alcohol are flammable with auto-ignition temperatures of 260 °C, 470 °C and 399 °C, respectively. Although pentane is dielectric and is expected to yield high critical heat flux and heat transfer coefficients, it is also a highly flammable liquid, however, the quantities needed for an evaporation device are small (10 mL $\sim$ 100 mL), reducing the risk of damage due to fire. A nonflammable candidate fluid is R245fa which is dielectric and has similar properties to pentane.

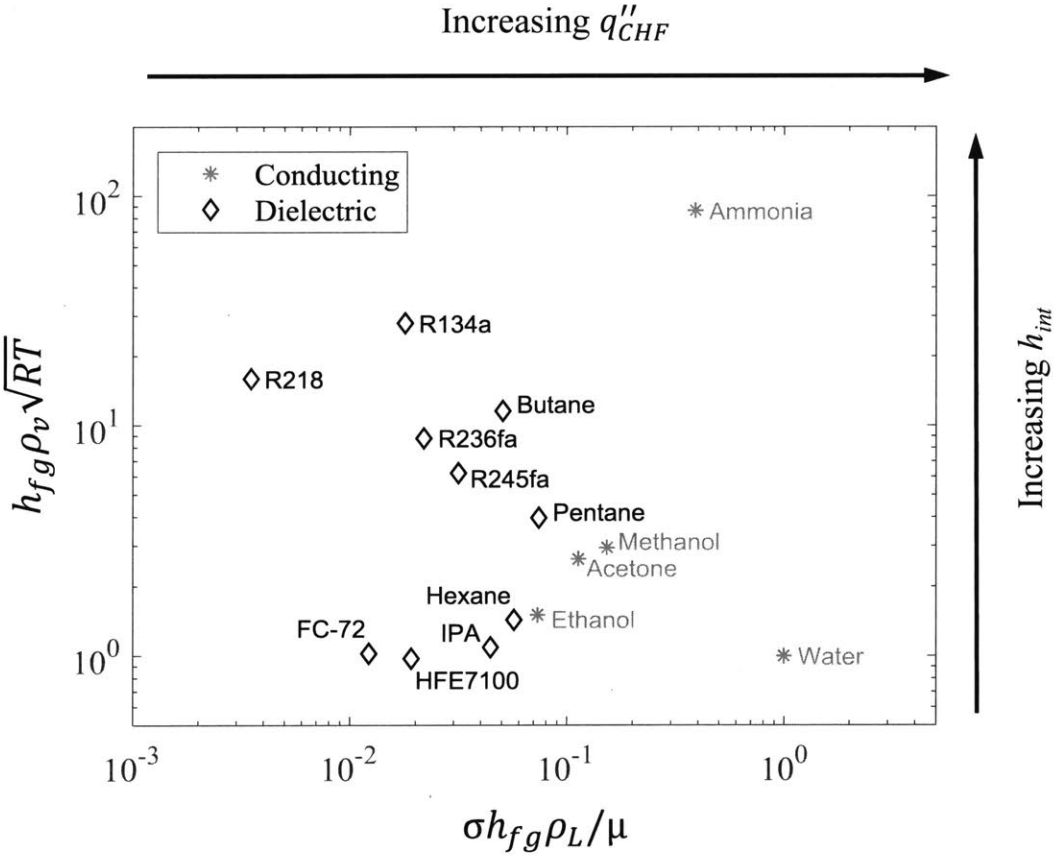

Figure 2-7: Comparison of figure of merit for critical heat flux and heat transfer coefficient for 15 common refrigerants and heat transfer fluids [44, 45] normalized by water.

2.3 Chapter Summary

A model was developed to estimate the critical heat flux based on the balance of capillary pressure at the membrane pores and viscous pressure in the supply channels. Using 120 nm pores and 2 µm supply channels, the estimated critical heat flux is over 1000 W/cm^2 using water, methanol, and pentane as working fluids. To predict the overall heat transfer coefficient, a thermal model using finite element analysis was developed which accounts for sub-continuum effects in the vapor and silicon as well as non-equilibrium effects at the liquid-vapor interface. The thermal model suggests that a new figure of merit applies to evaporation from nanopores: $\rho_v h_{fg}\sqrt{RT}$, representing a paradigm shift from conventional evaporation devices with pore sizes from 10 - 100 µm. Pentane and R245fa were identified as candidate working fluids for achieving a high heat transfer coefficient (50 W/cm^{2}K) at high heat flux (1000 W/cm^2).

Chapter 3

Microfabrication

In this chapter, the methods to fabricate suspended nanoporous membranes for experimental characterization are described. The pores fabricated for this prototype should be small enough to access the benefits of thin film evaporation from nanopores which is possible with 120 nm pores even though smaller pores may enable enhanced performance. The prototype devices were designed with a platform that is scalable to larger heater and membrane areas according to application requirements. Silicon was used to test the first prototype evaporation devices due to the substantially larger knowledge base of silicon fabrication and readily available materials in silicon. All fabrication was carried out in the MIT Microsystems Technology Laboratory and NanoStructures Laboratory, each maintaining a class-100 clean room environment.

3.1 Overview

The devices were fabricated using a two-wafer stack consisting of an SOI wafer bonded to a silicon wafer as shown in Figure 3-1. Interference lithography was chosen to define the pores based on its high uniformity, low defect density and fast exposure time. We first defined a pattern for 120 nm holes on the device layer with a 200 nm pitch. Also on the SOI wafer, the manifold was etched through the device layer, buried oxide and handle layer. On the silicon wafer, trenches were etched, which serve as liquid supply microchannels. Next, the SOI wafer and silicon wafer were fusion bonded together to form a monolithic evaporation structure. Platinum heaters and resistive temperature detectors (RTDs) were deposited 200 nm thick by electron beam evaporation and liftoff. Gold was deposited over platinum to to form electrical contact pads and metal traces for improving localization of heating. A film of silicon nitride was deposited using PECVD before the platinum and after the gold for electrical insulation. The membrane was released by etching through the backside of the

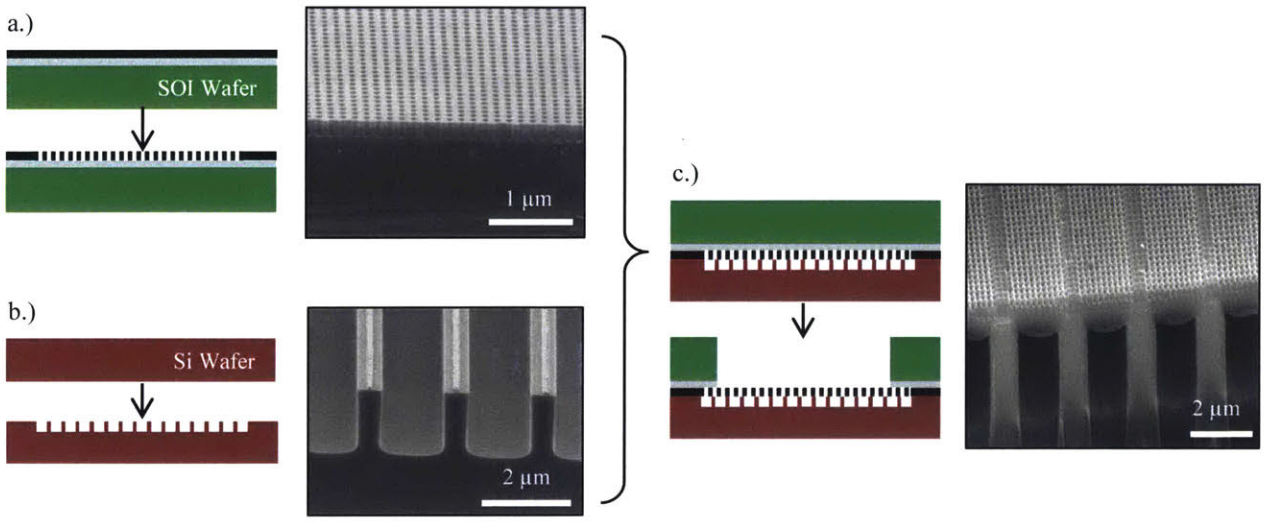

Figure 3-1: Overview of fabrication procedure using cross-section AA from Figure 1-2. The procedure is described in more detail in Section 3.3 .

SOI using the buried oxide as an etch stop. The liquid inlet and outlet ports were etched through the silicon wafer to interface with the liquid manifold. Each procedure is described in depth in Section 3.3.

3.2 Design of Fabrication Procedure

Alternative approaches are presented to define a pattern for nanopores and to create a suspended membrane structure. The design of resistive heating elements and RTDs is presented with considerations for dielectric breakdown, electromigration and RTD measurement sensitivity.

Approaches to Fabricate Nanopores

The most practical techniques to fabricate large, uniform arrays of sub-micron pores are based on lithography and dry chemical etching into silicon. Uniformity is paramount because the largest pore coincides with the location of dryout while smaller pores exhibit high pressure drop and low interfacial area. With this in mind, fabrication techniques were investigated with three key objectives: high uniformity, scalability to large areas and feasibility of fabrication time.

With contact photolithography limited to resolving features no smaller than 1 µm and projection photolithography limited to features no smaller than 0.5 µm, the most widely used

clean room tool to define features as small as 20 nm is electron beam lithography in which a focused ion beam writes a computer-generated pattern into a thin layer of photoresist. While the resolution and ability to customize the pore pattern using e-beam lithography is advantageous, the writing times necessary for patterning the entirety of a single 150 mm wafer is cost (>$100,000) and time (>1 month) prohibitive. Nano-imprint lithography is also capable of defining 10 nm features over an entire wafer in minutes, however it requires a master wafer that is typically patterned using electron beam lithography. Block copolymer self-assembly can be used to create lithography patterns with 20 nm to 70 nm periodic features in minutes over $\sim$ 1 cm^2 [46], but the defect density is too high for a nanoporous evaporation device where a single defect can lead to a dryout failure. It is conceivable to use a double exposure technique with a 0.65 µm projection lithography system to fabricate 0.32 µm features (similar to the techniques used by the semiconductor industry) but these still are too large to validate the concept. Using interference lithography, trillions of holes can be patterned across a 150 mm wafer in minutes with no defects. With a 325 nm light source, interference patterns can be created with 200 nm pitch and 80 to 150 nm pores. Therefore, interference lithography was chosen based on its high uniformity, low defect density, and fast exposure time.

Approaches to Fabricate Suspended Membrane

The fabrication of a thin membrane of 100 nm pores suspended over a support structure at this scale has never been accomplished. The most straightforward approach to creating a suspended membrane structure is to bond a membrane to an array of trenches to form liquid channels. Although etching 100 nm pores and bonding silicon wafers are developed technologies, the combination of these techniques presents challenges with achieving reliable bonds. Ultimately this approach was chosen and the details are listed in Section 3.3. However, alternative approaches to forming a suspended membrane structure were considered which do not involve a sensitive, low-yield fusion bonding process. In the first approach, shown in Figure 3-2, a 1 µm layer of silicon nitride is formed on a silicon wafer by deposition or doping. Next, nanopores are etched using interference lithography or another patterning method. Then an array of metal strips is deposited over the membrane pores which serves as a wet etch mask for carving out the liquid supply channels. Two candidates for wet etch chemistry are KOH and TMAH which isotropically remove silicon but not silicon nitride or metals. After the wet etch, the metal is removed yielding the desired structure. In the second alternative approach, shown in Figure 3-3, the microchannels are formed using the Silicon-on-Nothing method developed by Sato, et al. [47, 48] in which sub-micron pores merge by surface diffusion during hydrogen annealing at 1100 °C. In the next step, another array of nanopores is etched into the surface to form a suspended membrane structure as

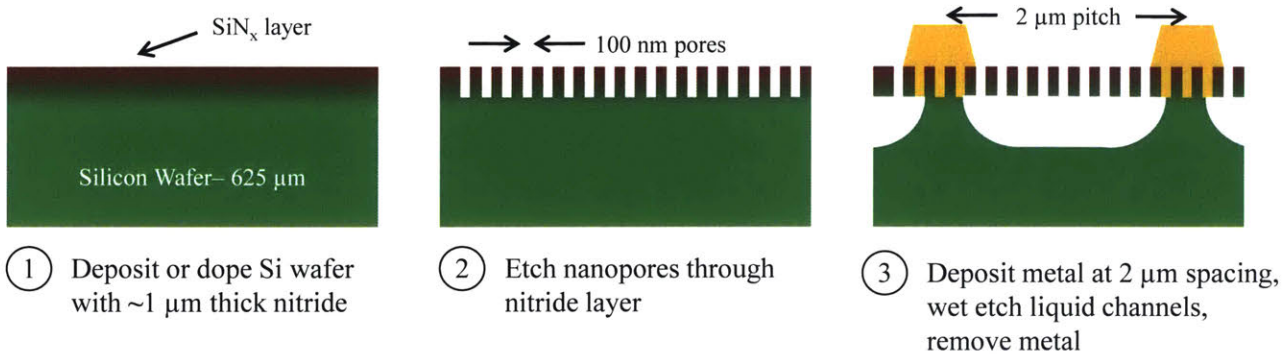

Figure 3-2: First alternative method to fabricate suspended membrane: first, deposit or dope silicon wafer with $\sim 1\,\mu m$ of nitride. Second, etch nanopores using interference lithography and RIE. Next, deposit a $2\,\mu m$ grating of metal and wet etch silicon underneath nitride. Finally, remove metal with wet etch.

shown in Figure 3-3. Although these approaches avoid fusion bonding, they are undeveloped technologies. Furthermore the heat transfer coefficient may suffer since the membrane thermal conductivity will be lower if it is made of silicon nitride rather than silicon.

Heater and RTD Design

To characterize the heat transfer performance of the samples, thin film platinum heaters and resistive temperature detectors (RTDs) were deposited on the back side by metal evaporation. This method is preferable to a heater block with embedded cartridge heaters and temperature sensors because it eliminates thermal interface resistance and allows for spatial resolution of temperatures based on RTD placement on the sample. A serpentine pattern of platinum is used to generate a uniform heat flux under the membrane only. The RTDs are arranged inside a bend of the serpentine heater pattern to measure the substrate temperature as close to the heaters as possible. The layout of heaters and RTDs is shown in Figure 3-4 for a sample with 25 vapor channels. The heaters and RTDs are insulated on top and bottom with Si_3N_4 dielectric.

The size of the serpentine heater pattern is determined by the vapor channel width and substrate thickness. Since the substrate would ideally be only $100\,\mu m$ thick, the width of the heater pattern was set to $50\,\mu m$ to achieve more uniform heat dissipation at the membrane. The space between strips of metal is also set at $50\,\mu m$ to allow for RTDs to be placed within

Figure 3-3: Second alternative method to fabricated suspended membrane: first, etch 100 nm pores using interference lithography as well as additional lithography step to block pores at 2 μm pitch. Second, anneal wafer according to method by Sato, et al. [47, 48] until pores merge to minimize surface energy. Finally, etch nanopores up to the depth of the liquid channels.

the heater pattern. The thickness of the heater was determined by material and processing constraints: deposition by e-beam evaporation of platinum more than 200 nm thick has a tendency of detaching from the substrate even when using an adhesion layer. The heat flux generated from a thin layer of platinum with cross-section 50 μm × 0.2 μm can be calculated using Ohm's Law, normalized by unit area:

$$\dot{Q} = i^2 R \tag{3.1}$$

$$R = \rho_e \frac{L}{wt} \text{ with } L/w = 2 \tag{3.2}$$

$$j \equiv \frac{i}{wt} \tag{3.3}$$

$$q" = \frac{\dot{Q}}{L^2} = \frac{i^2 \rho_e}{wtL} = \frac{1}{2} j^2 \rho_e t \tag{3.4}$$

where i is current, R is resistance, ρ_e is electrical resistivity ($1.06 \times 10^{-7}\,\Omega\,\text{m}$ for platinum), j is current density, and geometrical parameters are defined for a unit cell in Figure 3-5. For $w = 50\,/\text{um}$, $L/w = 2$, maximum thickness of 200 nm and resistivity of platinum, a current of $i = 0.307$ A is needed to reach 1000 W/cm^2 regardless of the total length of the heater. For a larger heated area, the serpentine pattern will be longer and have higher total resistance. For a heated area of 0.5 cm^2, the resistance is $5302\,\Omega$ and 1628 V is required to reach 0.307 A. To reduce the risk of electrical arcing, which can occur as low as 500 V, the heaters are divided into four heating zones on all samples so that a total of 1.23 A at 407 V is used to reach 1000 W/cm^2 over 0.5 cm^2.

The minimum thickness of Si_3N_4 required to prevent dielectric breakdown is determined

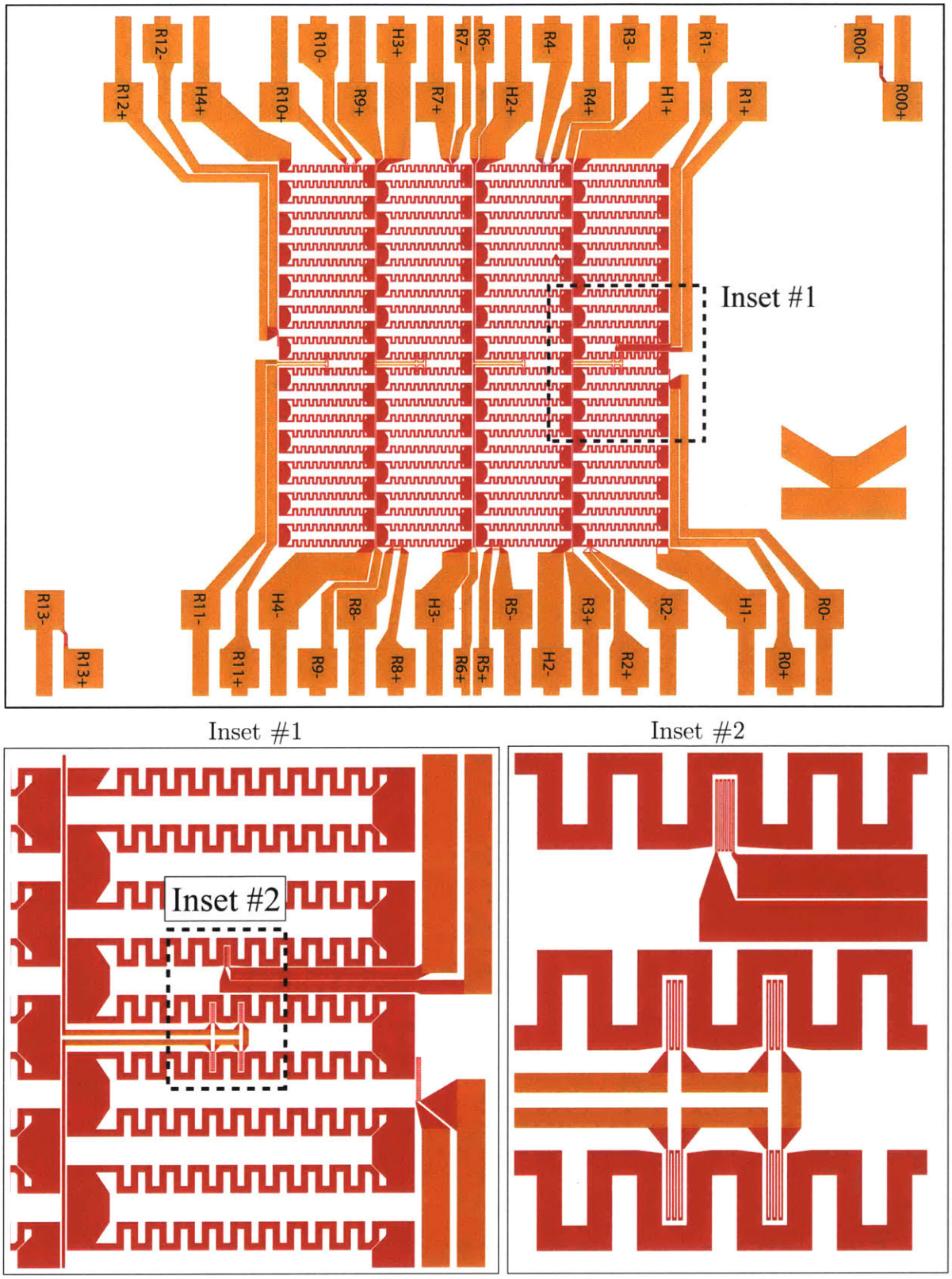

Figure 3-4: Top image shows heaters and RTDs (platinum) in red with traces and contact pads (gold) in yellow for sample with 25 vapor channels, each 200 µm wide and 10 mm long. Inset images show detail of RTD circuits.

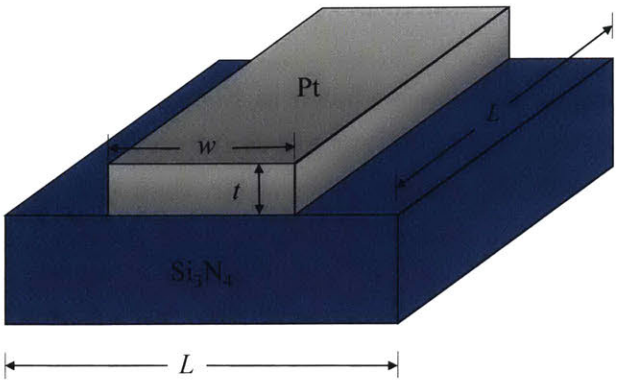

Figure 3-5: Unit cell of heater pattern: given material properties, metal thickness and spacing, the heat flux is exclusively a function of current density. If the current density is too high, the metal will fail due to electromigration.

by the dielectric strength of Si_3N_4 which is 1.0 MV/m for films deposited using PECVD. For a heater at 407 V, the minimum thickness is 0.407 µm.

Failure in metal circuits can occur by electromigration due to high current densities. Using Eq. 3.4 with the given material properties and geometric constraints, a current density of $j = 3.1 \times 10^6$ A/cm^2 is expected at $q'' = 1000$ W/cm^2. The mean time to failure ($MTTF$) in hours by electromigration is estimated empirically by Black's equation [49]:

$$MTTF = \frac{Awt}{j^2} \exp\left(\frac{Q}{kT}\right) \tag{3.5}$$

where A is an empirically determined constant (4.12×10^{15} for thin films), j is the current density in A/cm^2, Q is the activation energy for lattice diffusion in the metal (1.26 eV for platinum [50]), k is Boltzman's constant and T is the metal temperature. At T=100 °C, $j = 3.1 \times 10^6$ A/cm^2, t=200 nm and w=50 µm, the mean time to failure is 4×10^{12} hours, more than enough for a prototype device.

The resistance of RTDs should be large enough for accurate measurement, yet fabrication constraints limit the width of the pattern that can be defined by contact photolithography to $\sim$ 1.5 µm. Ideally, the RTD should be small such that it measures a localized temperature. Platinum is an excellent candidate material due to its large temperature coefficient (0.0391 K^{-1}) and resistance to corrosion. Commercially available platinum RTDs and RTD measurement devices have $R = 100 \sim 1000\ \Omega$. Using a pattern with a width, $w = 2$ µm, and a total length, $L = 1.54$ mm, the RTD can fit into the 50 µm × 150 µm space between bends of the heater pattern and resulting in a resistance of 408 Ω. A schematic of the RTD pattern is shown in Figure 3-4.

3.3 Fabrication

An overview of the fabrication process is shown in Figure 3-6. The suspended nanoporous membrane devices were fabricated by etching pores into a Silicon-on-Insulator (SOI) wafer and etching liquid supply channels into a silicon wafer, then bonding the two together. The membrane was "released" by etching the SOI wafer from the back side. Platinum heaters and resistive temperature detectors (RTDs) were deposited on the back side of the silicon wafer using photolithography, e-beam metal deposition and liftoff. The details of each step are described in the following sections.

Etching Nanopores

The membranes were fabricated by etching 100 nm pores into a thin-film silicon-on-insulator (SOI) wafer which is comprised of a $0.2 \sim 1.0\,\mu m$ thick "device layer" of crystalline silicon which has been fusion bonded to a crystalline silicon"handle layer" with a $1.0\,\mu m$ thermally grown oxide sandwiched in between. This "buried oxide" layer served as an etch stop during a later fabrication step, the vapor channel etch. The most common type of SOI wafer is fabricated by bonding two silicon wafers, each with thermally grown oxide layers, and then polishing the device layer to a desired thickness with a tolerance of $\pm 0.5\,\mu m$. This thickness tolerance is too high since the target thickness for membranes is less than $1\,\mu m$. Instead, thin-film SOI wafers were used in which the device layer is formed by bombardment of ions to a precise depth, followed by fusion bonding to a handle wafer and fracture of the device layer at the bombardment depth. This method yields a thickness tolerance of $\pm 0.01\,\mu m$, enabling excellent uniformity in membrane thickness.

Since dielectric fluids exhibit low surface tension, sub-micron pores are needed to generate sufficient capillary pressure for ultra high heat flux evaporation. Interference lithography was selected as a technique for patterning a mask which could be used in conjunction with dry plasma etch to fabricate a large array of 100 nm pores. Using interference lithography, trillions of holes can be patterned across a 150 mm wafer in minutes with no defects. A recipe developed in the MIT NanoStructures Laboratory was used [51] with a 325 nm He-Cd laser. The pitch, p, of an interference fringe pattern can be calculated by the equation

$$p = \frac{\lambda}{2\sin(\theta)} \tag{3.6}$$

where λ is the wavelength of light and θ is the incident angle of light measured from the surface normal vector as shown in Figure 3-7. For a laser wavelength of 325 nm, the largest incident angle for repeatably resolving features is 54 degrees resulting in a 200 nm pore pitch. By adjusting exposure and etch parameters, the pore diameter can be modulated

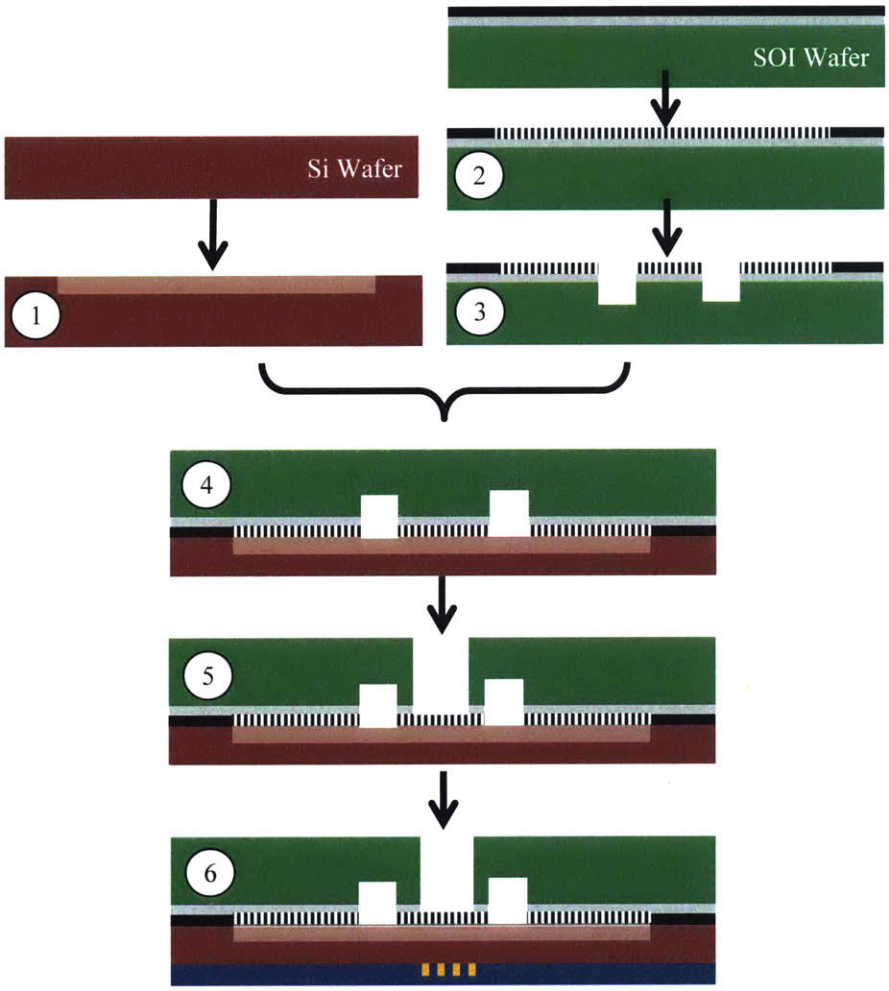

Figure 3-6: Overview of fabrication process: Ridge channels are etched into a silicon wafer (1). Nanopores (2) and manifold channels (3) are etched into an SOI wafer. The wafers are bonded together (4) and the membrane is released by etching from the backside of the SOI wafer (5). Finally, platinum heaters and RTDs are deposited (6) on the backside of the silicon wafer, insulated by Si_3N_4.

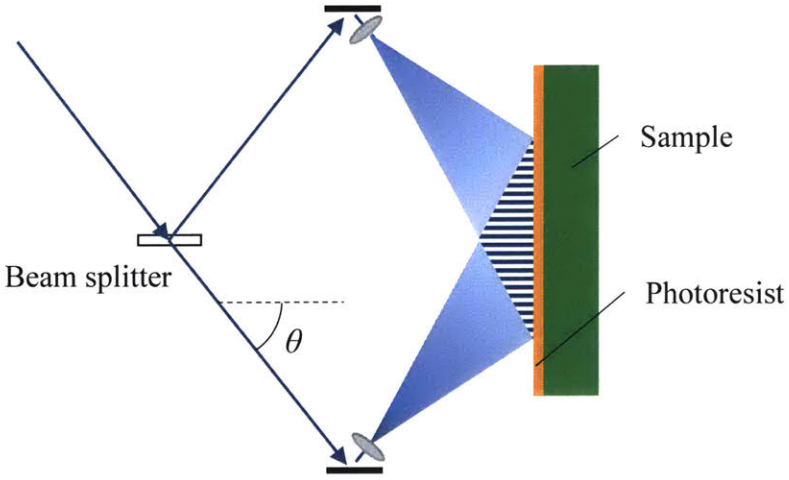

Figure 3-7: Exposure setup for interference lithography: two laser beams were expanded and cast upon a sample coated in photoresist, creating an interference pattern. After the first exposure, the sample was rotated 90 degrees then exposed again to create a grid pattern for etching pores.

from 80 nm to 150 nm at a fixed 200 nm pitch. A pre-exposure stack was first fabricated using a combination of spin coating and electron beam deposition resulting in a structure that minimizes reflections during exposure.

The first layer of the pre-exposure stack was 50 nm of SiO_2 deposited by e-beam evaporation which served as the hard mask for the pore etch. Next, an anti-reflection coating or ARC (Brewer Science, XHRiC-16) was spin coated and baked to yield a layer 170 nm thick. The wafer was then covered by a second layer of e-beam SiO_2 with a thickness of 20 nm. Next, an adhesion layer was spin coated onto the SiO_2 using ARC diluted with PGMEA to a thickness of 10 - 20 nm. Finally, a negative tone photoresist (OHKA THMR-iN PS4) was spin coated and baked to a thickness of 200 nm. A schematic of the final stack is shown in Figure 3-8.

Following preparation of the exposure stack, the wafer was mounted to a stage and exposed to two expanding beams of monochromatic, coherent laser light as shown in Figure 3-7. A single exposure results in a 1-D array of lines. Rotating the sample 90 degrees and exposing a second time results in a grid pattern which was used to etch pores. Following exposure, the photoresist was post baked and developed to remove unexposed regions of photoresist.

After the photoresist was developed, the pore pattern was transferred into a SiO_2 hard mask using three etches as shown in Figure 3-9 below. From $1 \rightarrow 2$ the wafer was etched in a charge-coupled plasma reactive ion etch (CCP RIE) using CF_4 to transfer the pattern into the SiO_2 interlayer. From $2 \rightarrow 3$ the pattern was transfered to the ARC using O_2. From

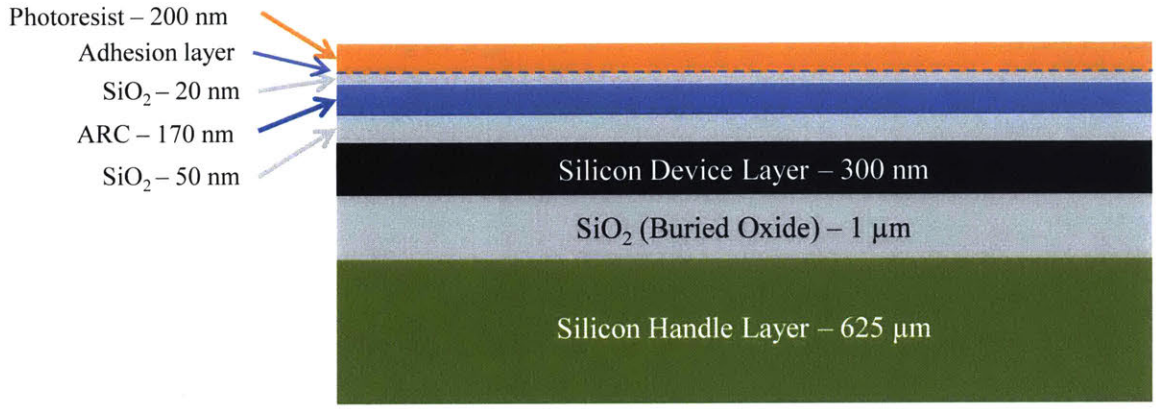

Figure 3-8: Schematic of Silicon-on-Insulator wafer with interference lithography stack in preparation for exposure.

$3 \rightarrow 4$ the ARC pattern was transferred into the SiO_2 hard mask using CF_4. Lastly, pores were etched in the silicon device layer of the SOI using HBr and O_2 in an inductively coupled plasma reactive ion etch (ICP RIE) tool. The final etch process stopped at the buried oxide of the ARC since HBr has very high chemical selectivity to etching silicon faster than silicon dioxide.

After the pores were etched through the membrane, some SiO_2 hard mask remained. The oxide surface had to be removed since it was too rough for fusion bonding and would create a thermal resistance to the suspended membrane structure. Removal of the SiO_2 hard mask using dry chemical etch with CHF_3 resulted in a surface which was also too rough for fusion bonding. Instead, a wet etch using buffered oxide etch ($HF + NH_4F$) was used to remove the SiO_2 hard mask, but first the pores were plugged to prevent HF from etching the buried oxide layer, thus undercutting the membrane as shown in Figure 3-10. To plug the holes, a polymer coating (ARC) was first spin coated on the wafer. Next, the coating was partially etched to expose the SiO_2 hard mask at the top of the pores but not the buried oxide layer at the base of the pores. Next, the wafer was dipped in BOE to remove the SiO_2 and finally, the remaining polymer was removed with O_2 plasma. The result is a wafer completely covered in a uniform array of 100 nm pores with a top surface as smooth as a prime wafer which can be fusion bonded to another prime wafer.

Liquid Manifold Channels

After etching pores into the device layer of the SOI wafer, manifold channels were etched through the device layer, buried oxide layer and into the handle layer to a depth of 140 µm.

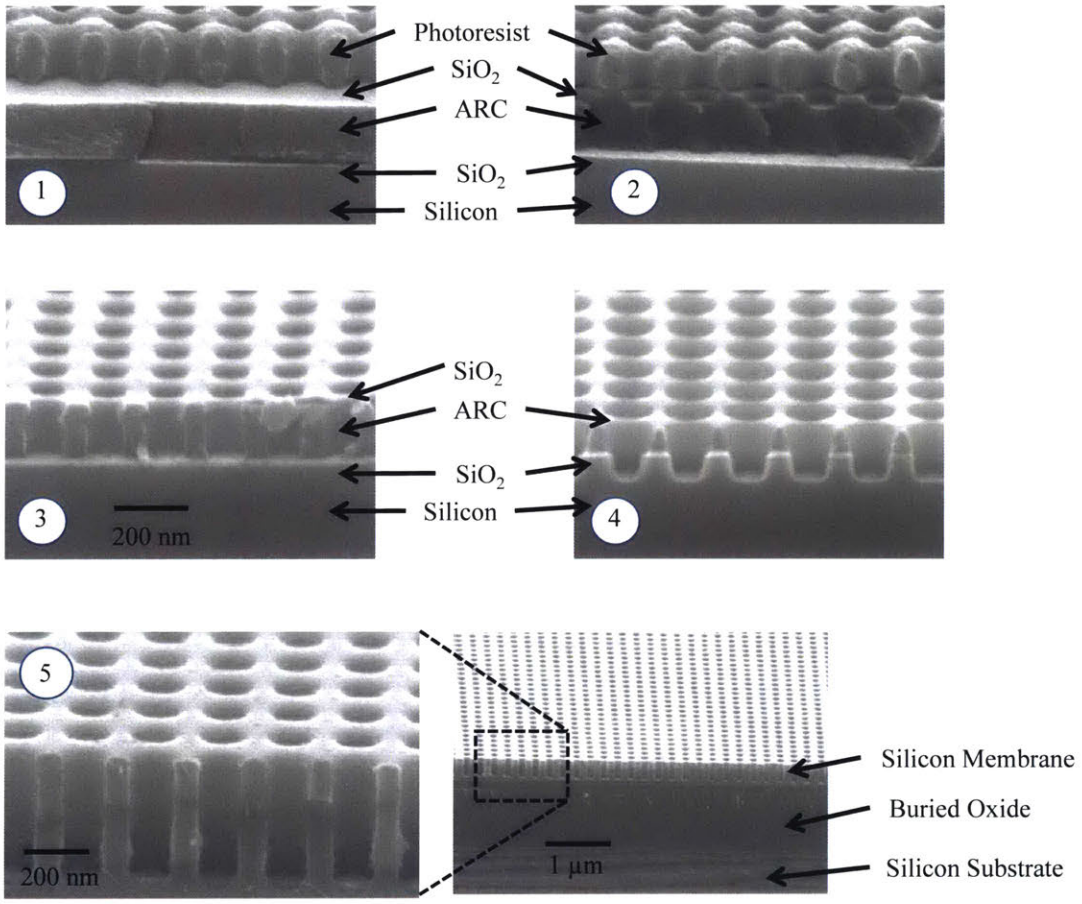

Figure 3-9: In three dry etch steps, the interference pattern was transferred from the photoresist to the SiO_2 interlayer to the ARC and finally to the SiO_2 hard mask. Using a 50 nm SiO_2 hard mask, the underlying silicon can be etched up to 800 nm deep using HBr plasma.

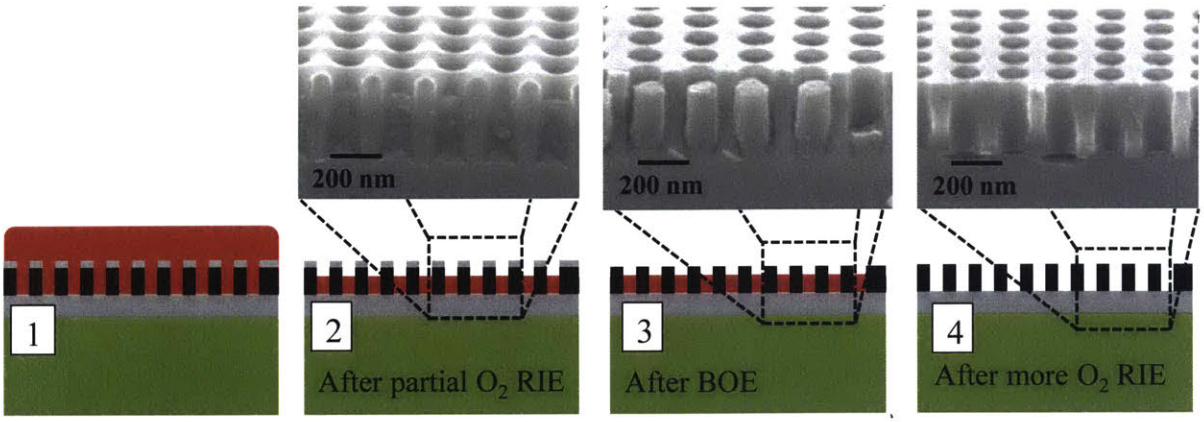

Figure 3-10: Wet etching process to remove hard mask without undercutting membrane. Step 1: spin coat organic polymer into pores. Step 2: partially etch polymer with oxygen plasma. Step 3: dip sample into BOE wet etch solution. Step 4: remove polymer entirely with oxygen plasma.

The pattern was created using 9 µm thick resist (AZ P4620, MicroChemicals) and contact photolithography. To form the manifold channels, the device layer was first etched with SF_6 plasma in an ICP RIE. Then, the buried oxide was wet etched using a buffered solution with a 7:1 ratio of NH_4F+HF. Finally, trenches were etched into the silicon handle layer using the Bosch process of alternating SF_6 etch gas with C_4F_8 passivation gas to yield high aspect ratio sidewalls as shown in Figure 3-11. The photoresist was stripped with a 3:1 solution of H_2SO_4+H_2O_2 in preparation for wafer bonding.

Liquid Ridge Channels

The liquid channels directly under the membrane were fabricated on a separate, double-side polished wafer. A layer of photoresist 1 µm thick (SPR700-1, Megaposit) was coated and patterned using projection photolithography. Trenches were etched in an ICP RIE using a simultaneous mixture of etch (SF_6) and passivation (C_4F_8) gases which yielded smoother sidewalls than the alternating Bosch process. The photoresist was stripped in oxygen plasma and the back side was patterned and etched 0.5 µm deep with marks to align metal and vapor channels patterns since liquid channels were concealed after bonding.

Wafer Bonding

The most critical fabrication step was bonding the membrane of the SOI wafer to the etched ridge channels to form a suspended membrane structure with good strength, low thermal interfacial resistance and a hermetic seal. Silicon fusion bonding, an established process

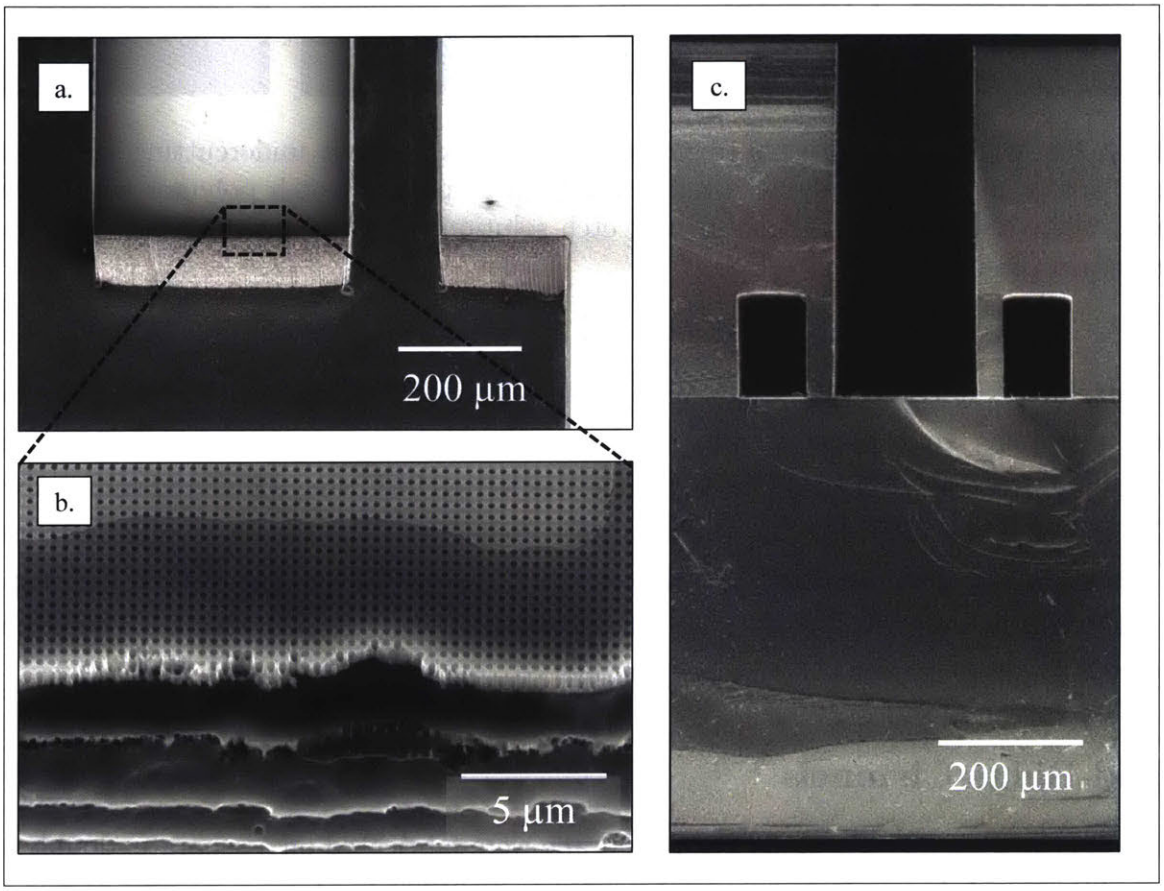

Figure 3-11: Manifold channels etched into SOI wafer: a.) manifold channels after bonding b.) membrane is undercut by only 5 µm following wet etch c.) cross-section of SOI bonded to silicon wafer showing high aspect ratio etch profile.

in MEMS fabrication, is known to be extremely sensitive to cleanliness, surface chemistry, surface roughness and wafer flatness. The process of bonding nanoporous membranes to ridge structures is even more challenging due to low solid fraction of the membrane (70%) and ridge structure (20%) which ultimately created low contact area (14%) for the bond.

A cleaning procedure was developed to systematically prepare wafers for bonds which exhibit low defect density, low stress and high strength. First, wafers were cleaned in a 3:1 solution of H_2SO_4 + H_2O_2 to remove residual photoresist and particles, then a 5:1:1 solution of H_2O + NH_4OH + H_2O_2 at 80 °C to remove other organic residue, then a 50:1 solution of H_2O + HF to remove the native oxide, then a 6:1:1 solution of H_2O + HCl + H_2O_2 at 80 °C to remove ionic contaminants. After the wet clean, the bond surfaces were activated with oxygen plasma to enhance Van der Waals adhesion. Finally, the wafers were cleaned once again in a 3:1 solution of H_2SO_4 + H_2O_2, rinsed in water a 80 °C and dried in a spin-rinse-dryer.

Immediately after the cleaning procedure, the wafers were mounted into an alignment tool (EVG620) with spacers between the wafers and transferred into a wafer bonding chamber (EVG501) which was evacuated to 10^{-3} torr using a turbomolecular pump. Next, a pin inside the bonding chamber pressed the centers of the wafers together and the spacers were removed to allow the wafers to adhere using Van der Waals forces. After venting the chamber, the wafers were inspected for particles or air bubbles using an IR camera (silicon is transparent in IR). If defects were present, the wafer pairs were separated by dipping into water. If there were no visible defects, the wafer pairs were annealed in a tube furnace at 900 °C for 4 hours in N_2 gas. The vacuum during wafer adhesion was necessary to prevent expansion of trapped gases inside pores and liquid channels during the anneal.

Metal Deposition

Platinum heaters and resistive temperature detectors (RTDs) were fabricated directly on the substrate to avoid thermal contact resistance. The back side of the ridge wafer was prepared by depositing 0.5 µm Si_3N_4 as electrical insulation using plasma-enhanced chemical vapor deposition (PECVD). Silicon nitride was used because it has a high dielectric strength (1 V/nm) and relatively high thermal conductivity (~10 W/m-K) compared to silicon dioxide (~1 W/m-K). The Si_3N_4 surface was coated with negative tone photoresist (Futurrex, NR71-1500PY) for the first metal liftoff pattern using contact photolithography. After developing the resist, the wafer was briefly exposed to oxygen plasma as a "descum" procedure to promote metal adhesion by removing residual organics on the Si_3N_4 surface. The wafers were then coated with 25 nm titanium for adhesion and 200 nm of platinum by electron beam deposition (Temescal Semiconductor, VES 2550). The wafers were soaked in acetone overnight to dissolve photoresist and lift off excess metal. Next, the wafer was annealed at

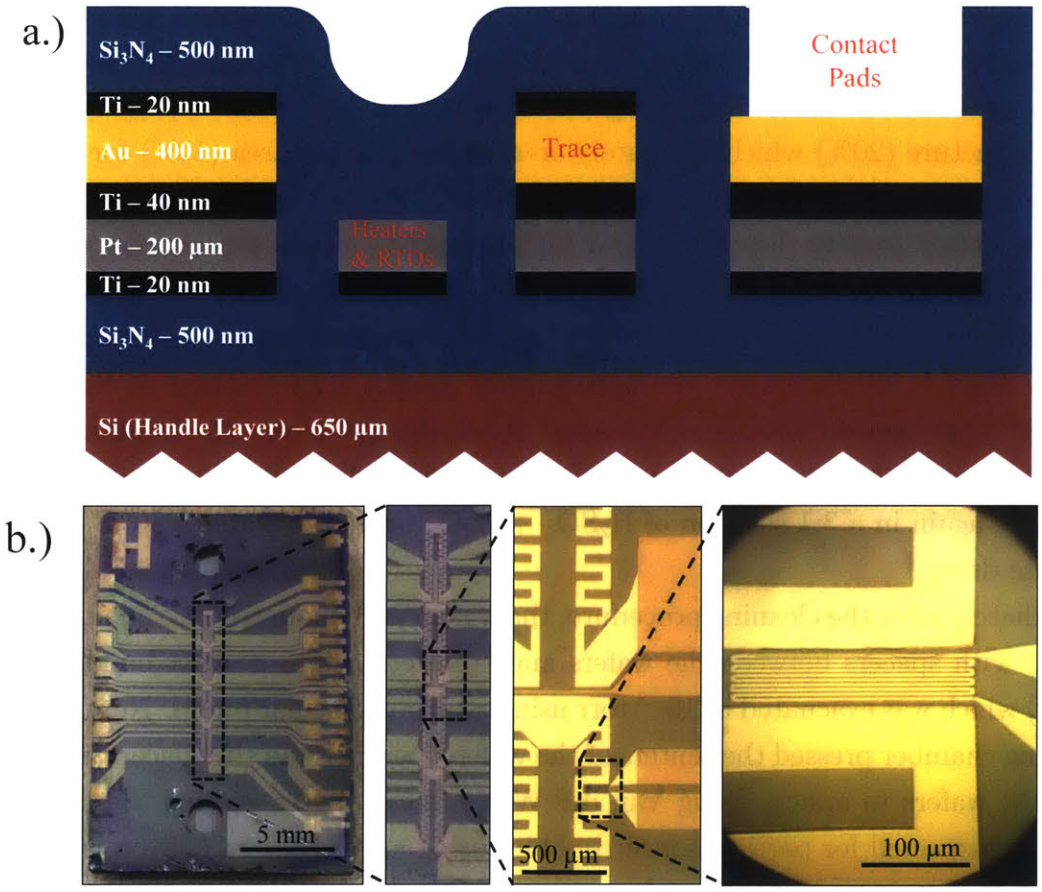

Figure 3-12: a.) Cross-sectional schematic of dielectric and metal layers. b.) Images of fabricated metal pattern: gold squares are contact pads, green regions are gold traces under Si_3N_4, large, pink, serpentine patterns are platinum heaters and fine, yellow, serpentine patterns are RTDs.

300 °C in N_2 gas to assist grain boundary diffusion in the platinum. The lift-off process was repeated with another layer of photoresist, deposition of 400 nm gold, and lift-off in acetone to form the metal traces and contact pads. The wafers were coated again with 0.5 µm Si_3N_4 using PECVD to protect the metal and prevent electrical arcing at high voltage. Finally, the Si_3N_4 was etched over the contact pads only using a contact photolithography mask and thick resist (MicroChemicals, AZ P4620). A cross-section is shown schematically in Figure 3-12a and top-down images are shown in Figure 3-12b.

Vapor Channel and Liquid Port Etch

The vapor channel etch is the process to "release" the membrane from the handle layer. Despite efforts to minimize stress during bonding and low-stress dielectric deposition, bonded

wafers were too bowed to fit properly over an electrostatic chuck for etching the vapor channels. The stress was so high that many ordinary processes caused wafers to fracture. The stress was mitigated by dicing the bonded wafers into samples using a die saw (Disco, DAD3240). Then, the handle side of the SOI wafer was patterned using contact photolithography for vapor channels and the samples were mounted to a carrier wafer with photoresist as an adhesive. The vapor channels were etched in an ICP RIE using the Bosch process (SPTS, Rapier DRIE) through the full thickness of the handle layer (650 µm) until the buried oxide layer was reached. Silicon dioxide has a high etch selectivity to silicon (100:1) in SF_6, but the buried oxide layer is only 1 µm thick. To prevent overetch, the RIE has an endpoint detection module which monitored the exhaust etch gas composition to determine when the buried oxide was reached. After the buried oxide is initially detected, the etch continued for a short time to etch the full depth at the edges of the vapor channel. The samples were unmounted and cleaned using a 3:1 solution of $H_2SO_4 + H_2O_2$. At this point, the membrane pores, ridge channels and manifold channels were still sealed since the buried oxide layer covered the pores.

The liquid inlet and outlet ports were patterned on the same side as the metal heaters using contact photolithography and etched in an ICP RIE using the Bosch process (SPTS, Rapier DRIE) through the full thickness of the silicon wafer (650 µm) until the manifold was exposed. There is no etch stop for the ports, but an overetch up to 510 µm is acceptable. At this point, the membrane pores, ridge channels and manifold channels were no longer sealed. Therefore, all further processing was done without liquid to avoid contamination in the high-capillarity structure. Photoresist from the port etch was removed using oxygen plasma.

The removal of the buried oxide layer was reserved as the final fabrication step for protection of the membrane. The oxide layer was etched in a CCP RIE (Plasmatherm) using CHF_3 which has a 3:1 selectivity for etching SiO_2 to Si which reduces the risk of overetch. After the buried oxide was removed, the membrane was partially etched to reveal the pores which, for some samples, did not penetrate the full thickness of the device layer as shown in Figure 3-13a. A cross-section using focused ion beam (FIB) of the suspended membrane structure is shown in Figure 3-13b. A coating of debris from FIB milling appears to plug the membrane from the bottom, however Figure 3-13c shows a view from the top in which the ridges are visible through the membrane pores.

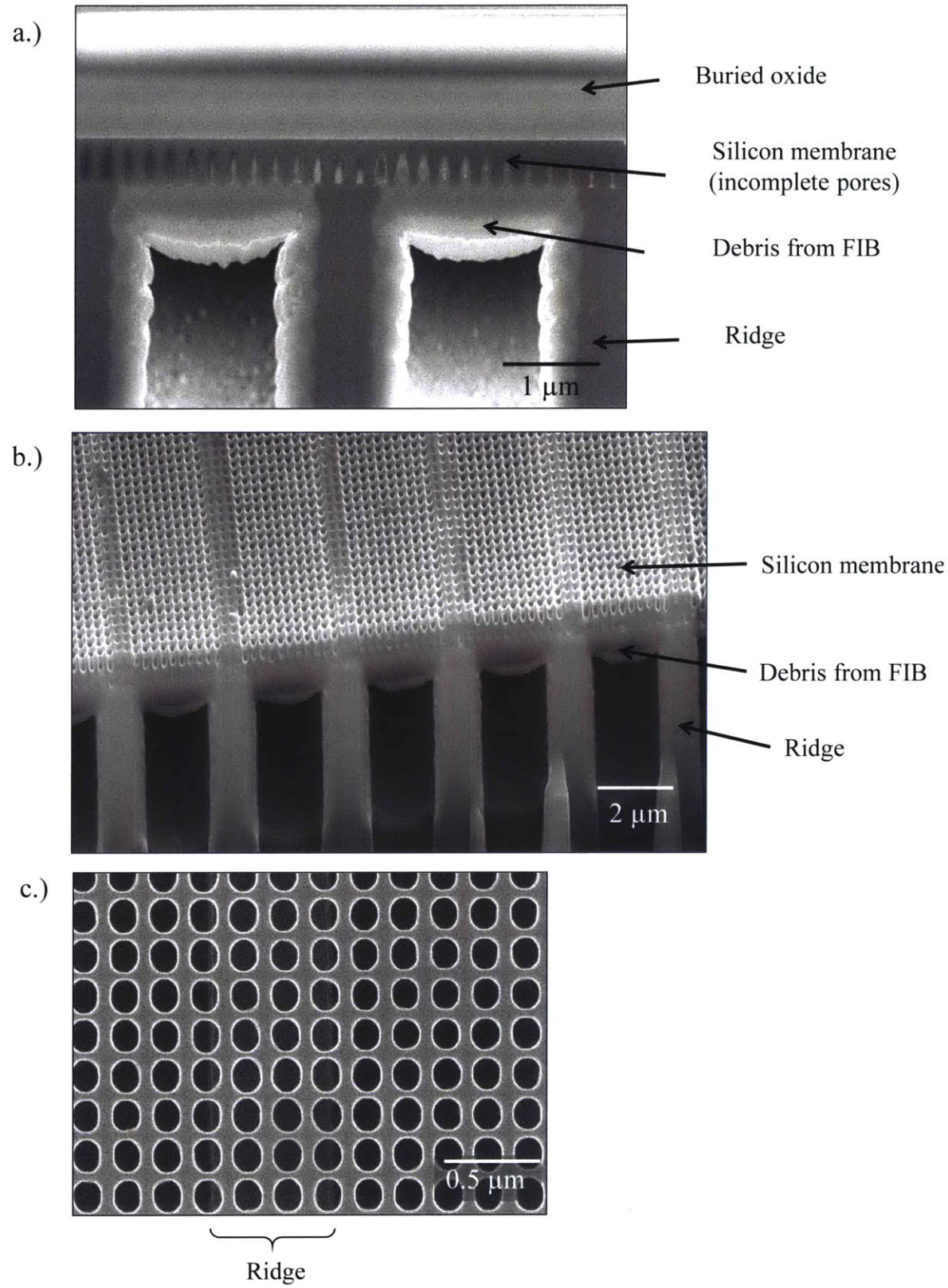

Figure 3-13: a.) Focused ion beam (FIB) cross-section of bonded membrane before buried oxide layer etch. b.) FIB cross-section after buried oxide layer etch. c.) Top-down view of membrane after buried oxide etch: ridges can be seen through pores.

Table 3-1: Step-by-step fabrication procedure for suspended nanoporous membrane devices as shown schematically in Figure 3-6

Step	Process	Description
①	Etch Ridge Channels	Pattern ridge channels with stepper projection photolithography and etch 2 µm with RIE, pattern alignment marks and etch 1 µm with RIE
②	Etch Nanopores	Pattern pores with interference lithography, transfer pattern into SiO_2 hard mask, etch with $HBr+O_2$ in ICP RIE, remove hard mask with BOE
③	Etch Manifold	Pattern manifold with contact lithography and etch 140 µm deep with DRIE
④	Wafer Bonding	Clean SOI and Si wafer with $H_2SO_4+H_2O_2$, O_2 plasma activation, align in bonder at 1×10^{-3} torr, anneal in furnace at 900 °C
⑤	Metalization	Deposit 0.5 µm low stress Si_3N_4 with PECVD, pattern photoresist for 200 nm Pt e-beam deposition and lift-off, repeat for 400 nm Au, deposit 0.5 µm more Si_3N_4, pattern openings for contact pads and etch 0.5 µm Si_3N_4 to reveal pads
⑥	Vapor Channel Etch	Pattern vapor channels with thick photoresist, etch handle with DRIE up to buried oxide etch stop
⑦	Port Etch	Pattern ports with contact photolithography and etch 650 µm deep with DRIE
⑧	Buried Oxide Etch	Etch buried oxide with CHF_3 to reveal membrane pores

3.4 Characterization

Three samples were successfully fabricated with no defects, completely bonded membranes and intact heaters. The samples were characterized for pore size, porosity and membrane size prior to experimental validation. Each sample was 18 mm × 24 mm × 1.2 mm in total size with vapor channels 10 mm × 0.2 mm, but they were distinguished by the number of vapor channels (1, 2 and 25) and therefore, total membrane area (0.02, 0.04 and 0.5 cm^2). Accordingly, the size of the heaters matched the size of the membrane area and the samples had 2, 3 and 26 manifold channels to distribute liquid into any of 5,000 ridge channels underneath the membrane of each vapor channel. A summary of samples that were successfully fabricated is shown in Table 3-2.

There are advantages to each sample configuration. While samples with smaller membrane areas have relatively large parasitic heat loss when normalized to the membrane area, there is a lower risk to overheat when the channels dry out because the total applied heat is

low. Because some defects in the membrane occur in randomized locations, a sample with a small membrane area is more likely to be completed without defects. Since the geometry of the membrane and ridge structure are almost identical for all samples, the overall heat transfer coefficient which is dominated by evaporation, is expected to be independent of the number of vapor channels. The exact membrane dimensions were measured in the SEM (Figure 3-14) to corroborate model predictions with experimental behavior of membrane devices.

Table 3-2: Summary of samples used for experiments

Sample ID	**# of vapor channels**	**width of membrane**	**membrane total area**	**pore size**	**porosity**
G	1	172.6 µm	0.017 cm^2	109.4 nm	0.242
H	2	163.1 µm	0.032 cm^2	135.7 nm	0.378
K	25	169.7 µm	0.424 cm^2	122.1 nm	0.295

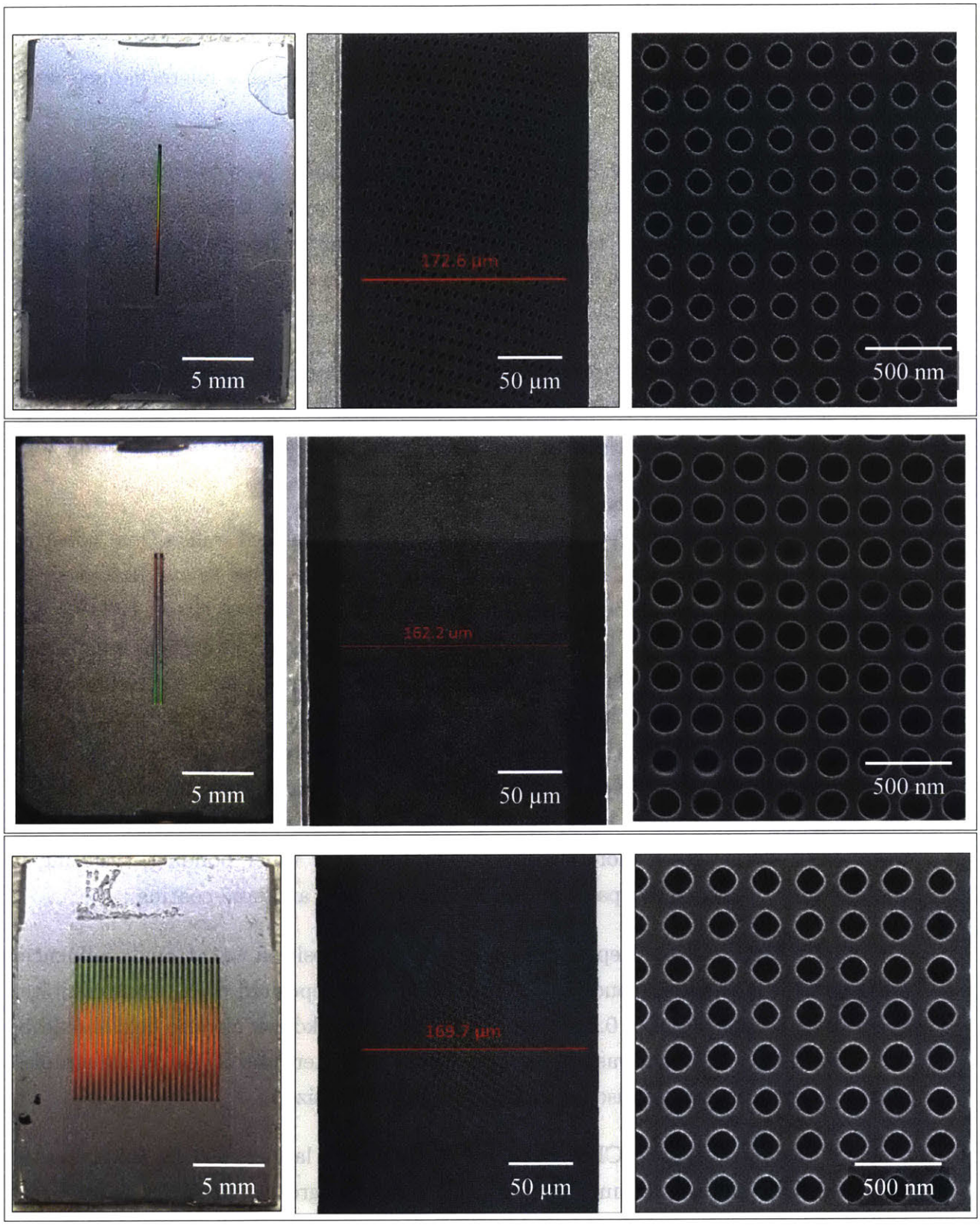

Figure 3-14: Images of samples with 1, 2 and 25 vapor channels. Variation in the width of membrane at the bottom of the vapor channel and variation in pore size are caused by changes in etch time during the final step to reveal the membrane.

3.5 Fabrication Challenges

The fabrication of an ultra-thin nanoporous membrane bonded to a microchannel array presented many challenges:

- **Interference Lithography Exposure:** As the expanding laser beam is incident on the wafer during exposure, the intensity varies across the wafer. If the variation between the two beams is too large, there is not enough destructive interference and no pores are defined. This limited the size of the pore pattern to only 100 mm, under-utilizing the full area of the 150 mm wafer.

- **Wafer Bonding:** The most critical step in the fabrication procedure is wafer bonding. A high quality bond is vital for thermal conductivity and structural support. All steps leading up to wafer bonding were performed with the objective of promoting high quality bonds.

- **Wafer Stress:** Wafer bow, caused by uneven stress, prohibited wafers from adhering during the bonding process. After bonding, stress imbalances led to wafers fracturing. Since the SOI wafer includes a buried oxide which was formed at $\sim$ 1000 °C, the wafers have a tendency for high stress after the bond anneal. Most SOI wafers have an oxide on the handle wafer, thermally grown simultaneously with the buried oxide, which balances the stress with the buried oxide. For initial fabrication attempts, the device layer was thinned with thermal oxidation and buffered oxide etch ($HF+NH_4F$). However, the buffered oxide etch removed the oxide layer on the handle wafer without removing the buried oxide layer, causing wafer bow due to unbalanced stress. The unbalanced stress was a more significant problem after wafer bonding, resulting in fracturing of bonded wafer pairs during PECVD, ashing and spin-coating.

- **Dielectric Deposition:** Repeatability of dielectric deposition was strongly influenced by the PECVD chamber conditions and history. The deposited Si_3N_4 films exhibited breakdown at 100 V across 0.5 µm even though the breakdown electric field should be 10^9 V/m. The breakdown was not uniform across all heaters and RTDs on the samples, therefore the existence of discreet pinholes was hypothesized.

- **Aspect Ratio of Vapor Channels:** Since the handle layer is 650 µm thick and the manifold walls are only 50 µm thick, an aspect ratio of greater than 10:1 is necessary to prevent destruction of the manifold walls.

- **Etch Uniformity of Vapor Channels:** This task is complicated by having a variety of vapor channel sizes (200, 500 and 1000 µm). Larger features tend to etch faster.

In addition, a single vapor channel etches faster than an array of 25 vapor channels. Within an array of 25 vapor channels, the channels at the edge etch faster than those at the middle.

- **Buried Oxide Etch Uniformity and Selectivity** The highest selectivity for dry etching SiO_2 to Si is with CHF_3. Since the buried oxide is at the bottom of a deep trench, the etch was transport limited and etch rates at the center of the channel were higher than at the edges. In the future, etching using HF vapor may improve the process, as long as the HF vapor does not remove the native oxide that bonds the membrane to the ridges.

- **Pore Etch:** The etch rate of pores using HBr + O_2 becomes slower as the etch depth increases. Before the pores are etched a full 1 µm, redeposition occurs at the pore surface leading to a pore profile that is not straight. The etch depth is difficult to measure without breaking the wafer. In addition, the pore hard mask etch resulted in a passivation layer in the silicon device layer which could not be etched by HBr + O_2. The passivation layer was removed before etching with HBr using a short pre-etch (30 s) with CF_4 + O_2 without exposure to atmosphere between etches.

- **Platinum Deposition:** Adhesion of platinum films more than 250 nm in thickness was unreliable. The resistivity of the platinum films was over 2× higher than bulk values, even though thin film conductivity effects do not occur in metal films over 10 nm thickness. An anneal at 350 °C yielded slight improvements. Feature sizes below 3 µm were difficult to control across the wafer due to nonuniform exposure intensity.

3.6 Chapter Summary

Devices were fabricated using silicon micromachining with geometries according to the system level model, described in Chapter 2. A repeatable process was developed for creating nanopore arrays with low defect density. A hierarchical fluidic network was created to supply working fluid to the membrane to sustain continuous thin film evaporation while minimizing viscous pressure losses in the device. The fluidic network is hermetically sealed together with the nanoporous membrane with high yields. Thin film platinum heaters and sensors were deposited to emulate the ultra-high heat fluxes of high power electronic devices. This work is a platform to test feasibility of evaporation from nanoporous membranes.

Chapter 4

Experimental Characterization & Analysis

Experiments were conducted to validate and characterize evaporation from nanoporous suspended membrane devices. We built a custom environmental chamber to test our fabricated samples in pure vapor ambient conditions. The chamber was used to maintain precise control of working conditions such that the experimental data could be appropriately compared to model predictions. The sample RTDs were calibrated for high accuracy temperature measurement at the backside of the sample. Parasitic heat loss due to sensible cooling and conduction were calculated to extract evaporative heat flux from the total input heat flux. The substrate temperature rise was recorded for a range of evaporative heat fluxes up to 500 W/cm^2. Experiments were conducted with five working fluids: water, isopropyl alcohol, methanol, pentane and R245fa. High volatility fluids such as pentane and R245fa yielded higher heat transfer coefficients than low volatility, high surface tension fluids such as water. Model predictions showed good agreement with experimental data over the range of heat fluxes until clogging degraded performance. The results demonstrate that evaporation from nanopores operates in a unique regime that is restricted by emission from the liquid-vapor interface rather than conduction in the liquid and evaporation structure.

4.1 Setup

Environmental Chamber

A custom experimental apparatus was designed and built for testing fabricated devices in pure vapor conditions. The chamber is cylindrical with a diameter of 30 cm, made from 304 stainless steel and can operate under vacuum down to 0.3 Pa and positive pressure up to 1.7 MPa. Flanges are sealed with either indium wire or Viton fluoroelastomer as gasket materials. Metal seals (indium wire gasket, tube compression fittings, copper VCR gaskets and silver-coated copper CF gaskets) are used wherever possible to reduce outgassing

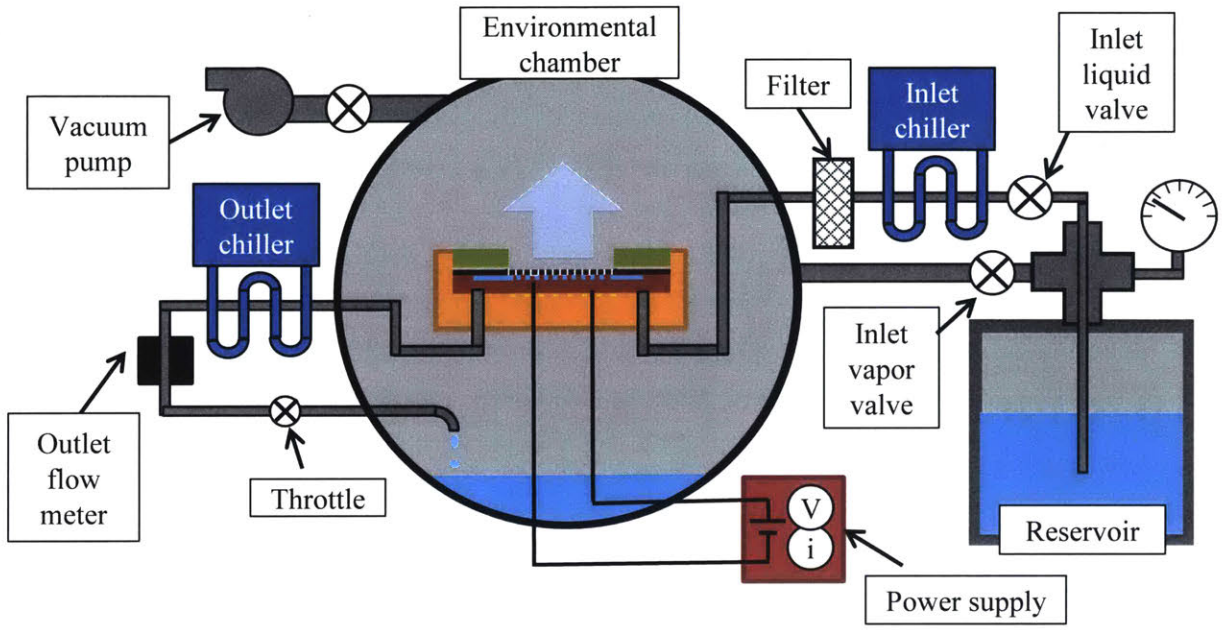

Figure 4-1: Schematic of experimental setup. Liquid from reservoir flows through inlet chiller, 0.5 µm filter, then into the sample manifold channels. Some liquid is evaporated from the membrane while some liquid bypasses the membrane and flows through a chiller, flow meter, throttle valve and drains into the chamber.

and leaching from elastomer gaskets. There are two viewports made from sapphire for visualization during evaporation.

As shown in Figure 4-1, the working fluid began in the reservoir which has a volume of 2.5 L. The reservoir was made from an 8" CF half-nipple and contained no elastomer materials. During an experiment, the reservoir was heated to pressurize it and deliver liquid into the chamber. To maintain purity of the fluid, no external pumping was used. The liquid passed through a chiller to subcool it to 19 °C and prevent nucleation as the pressure dropped. A thermocouple (TMQSS-062, Omega) and pressure transducer (PX319, Omega) were used to measure temperature and pressure of the inlet liquid before it flowed through a 0.5 µm filter (SS-2TF-05, Swagelok) and then entered into the chamber and subsequently the test device. While some liquid evaporated and eventually condensed on the chamber walls, the remaining liquid flowed through the device, exited the chamber, flowed through a chiller and a flow meter (L-series, Alicat) which measured the outlet flow rate, temperature and pressure. Finally, the liquid passed through a throttle valve and then back into the chamber. The throttle valve, along with the reservoir, controlled the pressure in the liquid manifolds of the device and outlet flow rate. If the liquid manifold pressure was too high, liquid would flood the membrane and thin film evaporation would not occur. Conversely, if the manifold

pressure was too low, liquid in the manifold channels would boil and the system would dry out. To purge the membrane of nonvolatile contaminants between evaporation experiments, the throttle valve can be closed to force liquid through the membrane pores and flush contaminants. The vapor temperature was monitored by thermocouples (TMQSS-062, Omega) inside the chamber while the vapor pressure was monitored by a capacitance manometer (628D12TBE1B, MKS Instruments). Images of the chamber, reservoir and instrumentation are shown in Figure 4-2. The chamber was wiped clean with acetone, methanol and isopropyl alcohol using a lint-free cloth before each experiment.

Sample Holder

The sample holder facilitated the electrical and liquid connections to the sample. It was comprised of a block and clamp plate (Figure 4-3), both made from Ultem, a polyetherimide with high dielectric strength, low thermal conductivity (0.12 W/mK), good machineability and a working temperature range up to 170 °C. The block accommodated up to 46 spring-loaded, gold-coated pins which contacted gold pads at precise locations on the sample to power heaters and measure RTD resistances. A thermocouple for calibrating RTDs contacted the back side of the sample. The block also encompassed two stainless steel tubes (4.8 mm diameter) for inlet and outlet liquid flow. The tubes were thick-walled (1.2 mm) to accommodate a gasket made from either Viton fluoroelastomer or indium wire. O-rings made with Viton are chemically inert, stable up to 230 °C and exhibit low thermal conductivity. As with many elastic polymers, Viton gaskets have finite permeability and swell when absorbing solvents such as methanol, pentane and R245fa, introducing a risk of leaching contaminants. Gaskets made from indium wire, like most metals, are practically impermeable to gases and liquids and inert to all organic solvents. The high conductivity of indium, however, causes twice as much parasitic heat loss compared to Viton gaskets. Although indium is a very soft material, its lack of elasticity can cause leaks, for example, when the test block expands at high temperature. Both materials were used during evaporation experiments despite their imperfections.

Degassing

If the concentrations of dissolved, noncondensible gases (*e.g.*, N_2, O_2, CO_2, *etc.*) is too high, nucleation is more likely when the working fluid rises in temperature and drops in pressure as it flows into the ridge channels. Unlike nonvolatile contaminants, a finite concentration of dissolved gases can be tolerated in the liquid since the gases eventually exit the membrane at the liquid-vapor interface. According to Henry's Law, the concentration of a particular gas in solution is proportional to the partial pressure of the gas. Thus, the concentration of gases

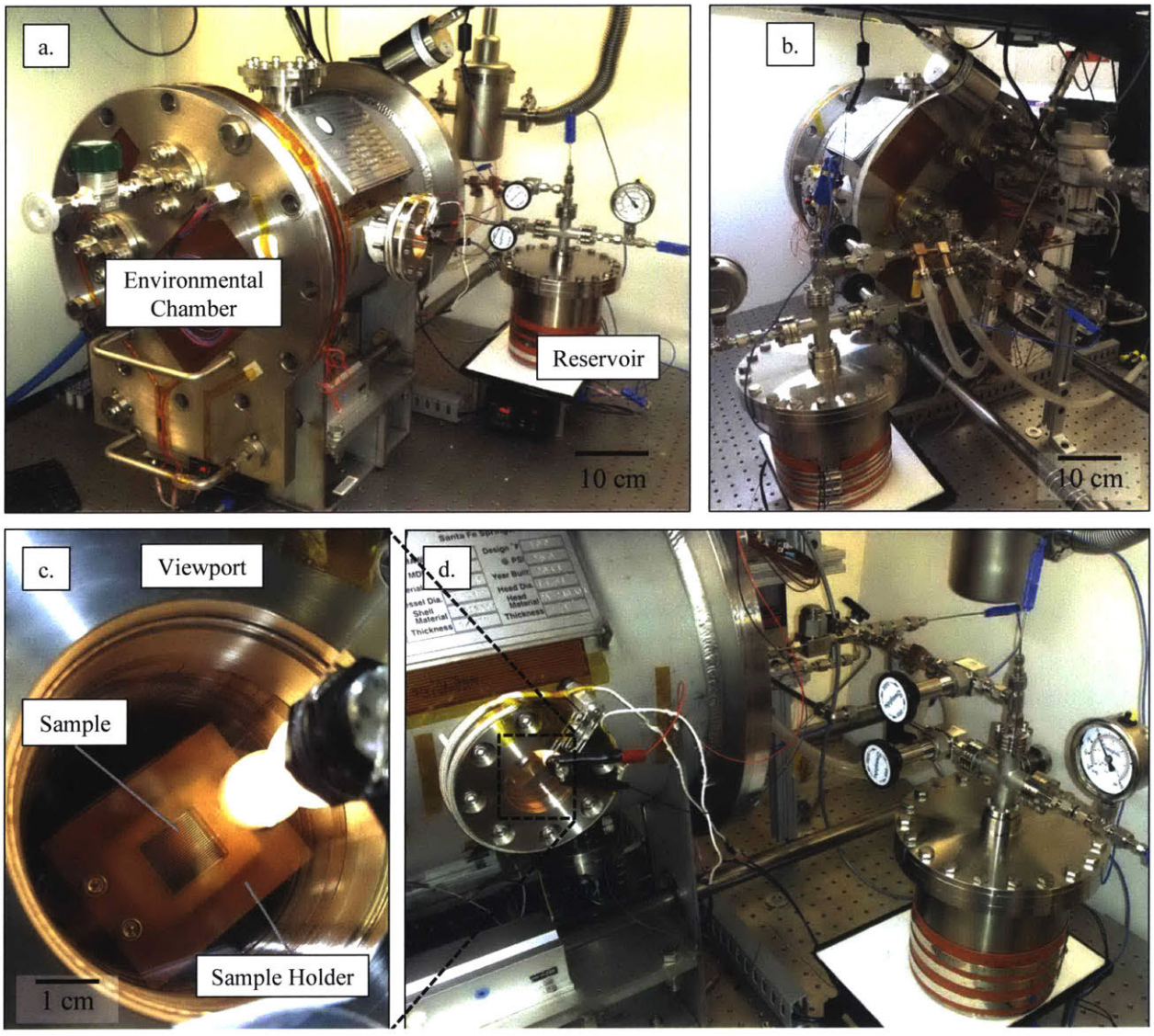

Figure 4-2: Images of a.) front side of environmental chamber, b.) back side with electrical and fluid feedthroughs, c.) viewport and fabricated sample, and d.) side view.

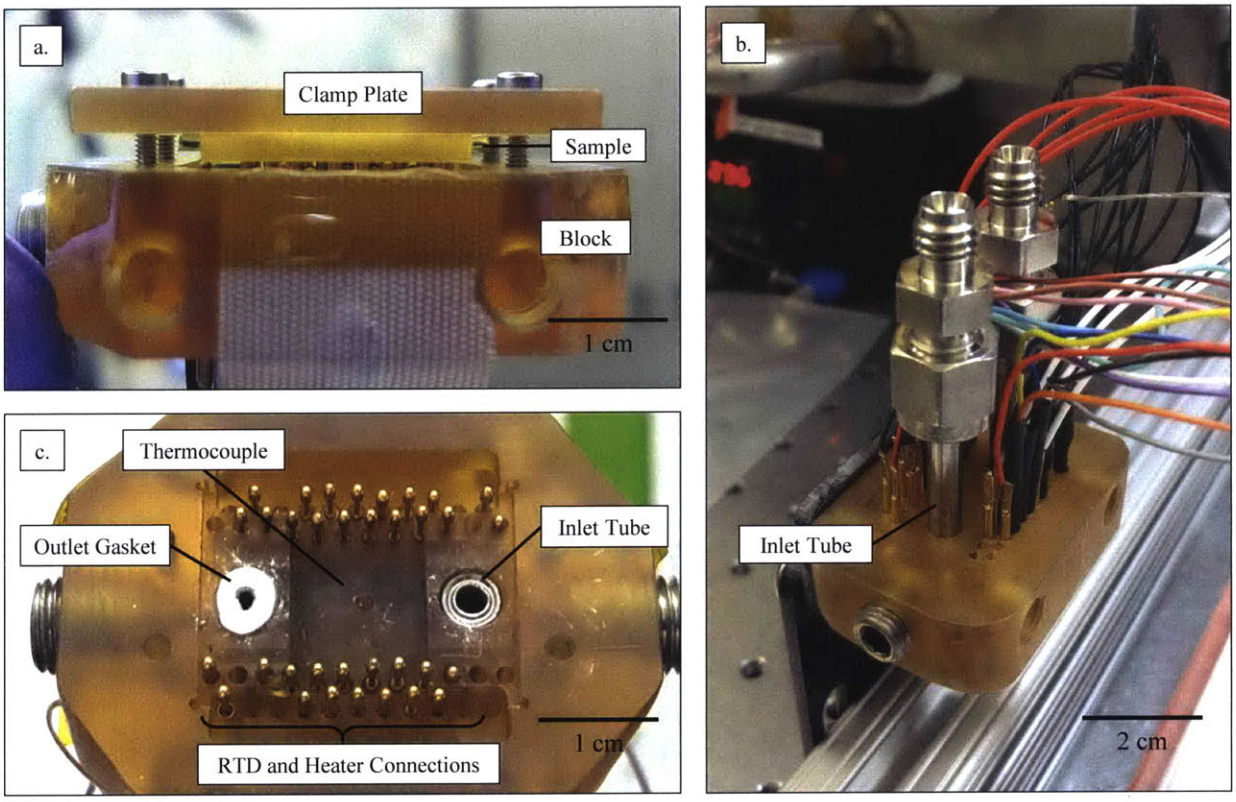

Figure 4-3: a.) Side view of sample before clamping into fixture b.) back side with electrical connections and tubes c.) pogo pins and tube connections. The thermocouple used to calibrate the sample is in the center. In this image, the left tube has an indium wire gasket, while the right tube has no gasket.

dissolved in the liquid can be indirectly quantified by subtracting the calculated saturation temperature from the measured total pressure. This technique is limited, however, by the accuracy of pressure and temperature measurement as well as temperature gradients. A more precise method was used to quantify dissolved gas concentration according the following procedure:

1. Evacuate the chamber to a base pressure $\leq$ 1 Pa (the sensitivity of the capacitance manometer). Close the valve between the vacuum pump and the cold trap. Close the valve between the chamber and the cold trap.

2. Open the vapor valve between the reservoir and the chamber to release vapor and non-condensible gases into the chamber. Wait until the chamber pressure rises to 1000 Pa to limit the loss of fluid from the reservoir. Close the vapor valve.

3. Open the valve between the chamber and the cold trap to condense vapor but not noncondensible gases from chamber. As noncondensible gases accumulate in the cold trap, vapor must diffuse through a layer of noncondensibles to condense.

4. The pressure decays exponentially with time. As a standard for repeatability, wait 2 minutes and record chamber pressure which reflects the remaining noncondensible gases.

When the final pressure reading matched the base pressure of 1 Pa and no more noncondensible gases could be detected, the fluid was ready for distillation. Because the capacitance manometer has an accuracy of ± 1 Pa, this method had much higher resolution than subtracting saturation pressure from total pressure.

Distillation

The current channel configuration is prone to clogging by nonvolatile contaminants as described in Section 4.6. While insoluble contaminants such as solid particles can be removed using commercial filters with mesh sizes as small as 0.05 µm, the only way to remove soluble contaminants is by adsorption or distillation. Purification of water and water soluble compounds is possible with adsorption on a polymer or activated carbon material [52]. However, current adsorbents are not well suited for removing soluble contaminants in solvent solutions such as pentane, R245fa, isopropyl alcohol and methanol. Therefore, distillation was used to improve fluid purity. The liquid was distilled using two reservoirs as shown in Figure 4.1 according to the following procedure:

1. Clean reservoir #2 with acetone, then methanol, then isopropyl alcohol in ultrasonicator.

2. Connect the vapor valve of reservoir #1 to the vapor valve of reservoir #2 with a bellows tube.

3. Evacuate the air from reservoir #2 and from the connecting bellows tube through the liquid valve, then close liquid valve.

4. With both vapor valves open, heat reservoir #1 and cool reservoir #2. The mass of transferred fluid can be measured on a scale.

5. Close all valves and disconnect bellows tube.

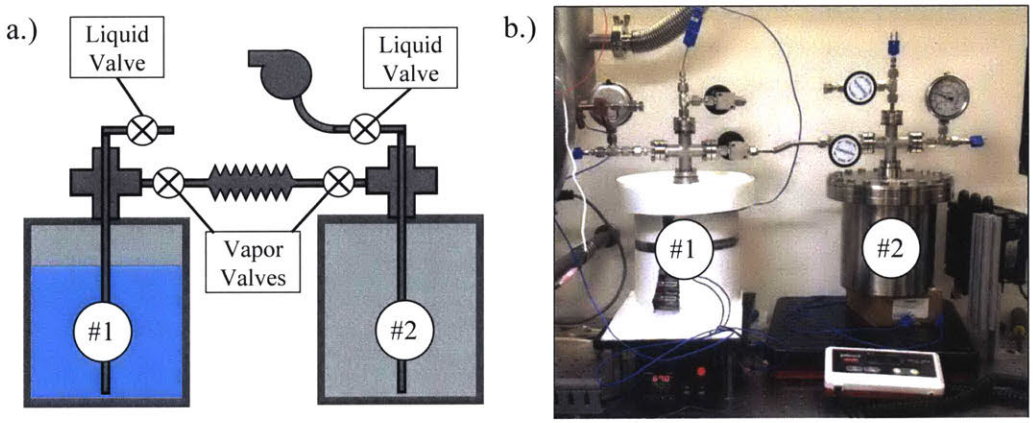

Figure 4-4: a.) Schematic of distillation procedure. Degassed liquid from reservoir #1 evaporates and condenses in reservoir #2 to purify working fluid of nonvolatile contaminants. b.) Image of distillation process where reservoir #1 is heated using a silicone heat sheet and PID controller while reservoir #2 is cooled with a 20 W fan.

Before distillation, the liquid has a nonvolatile contaminant concentration (also called non-evaporation residue concentration) of 1 - 5 ppm, as specified by the chemical suppliers (Sigma Aldrich and Alfa Aesar). Depending on the liquid viscosity, surface tension and vapor pressure, approximately 10$\sim$20 mL of liquid film remains in the reservoir after dumping the bulk of the liquid during Step 1. Since 2 L of liquid will condense in the reservoir during distillation, there is a potential for $100\times - 200\times$ improvement in purity, provided that liquid does not boil in reservoir #1 and splash liquid into reservoir #2. In practice, measurements using high pressure liquid chromatography (HPLC) suggested that fluid purity improved by only $2\times$, likely due to liquid splashing during boiling.

Thermocouple and RTD Calibration

The most important measurements to evaluate performance of a heat dissipation device are the applied heat flux and temperatures at two locations: first, the location of heating, *i.e.*, on

the substrate where the heaters are located, and second, at the location of heat dissipation, *i.e.* the vapor temperature since the condenser is not considered in this study. Temperatures on the substrate were measured using custom RTDs which were fabricated using photolithography, e-beam deposition of platinum and lift-off simultaneously with fabrication of thin-film platinum heaters as described in Section 3.3. The resistance of each RTD was measured using a cDAQ module (NI 9226, National Instruments) designed specially for RTDs which used 0.1 mA current excitation for each channel.

Since each metal deposition was unique in width and thickness due to variability in lithography and deposition, respectively, samples needed to be individually calibrated before evaporation experiments. The custom RTDs were calibrated in the environmental chamber using a T-type thermocouple as a reference point. The thermocouples were themselves calibrated in a water bath (Lauda Eco). However, the sample was not immersed in the water bath to avoid contamination. Instead, the sample was mounted into the chamber with a calibrated thermocouple touching the back side of the sample. The chamber was insulated and then heated from room temperature to 80 °C in increments of 10 - 15 °C. At each temperature set point, the heaters were allowed 2 hours to reach thermal equilibrium before temperature and electrical resistance data were recorded. A linear regression was performed to calculate RTD temperature as a function of the resistance as shown in Figure 4.1. The calibration results in less than 0.1 K deviation between the measured resistance and linear fit.

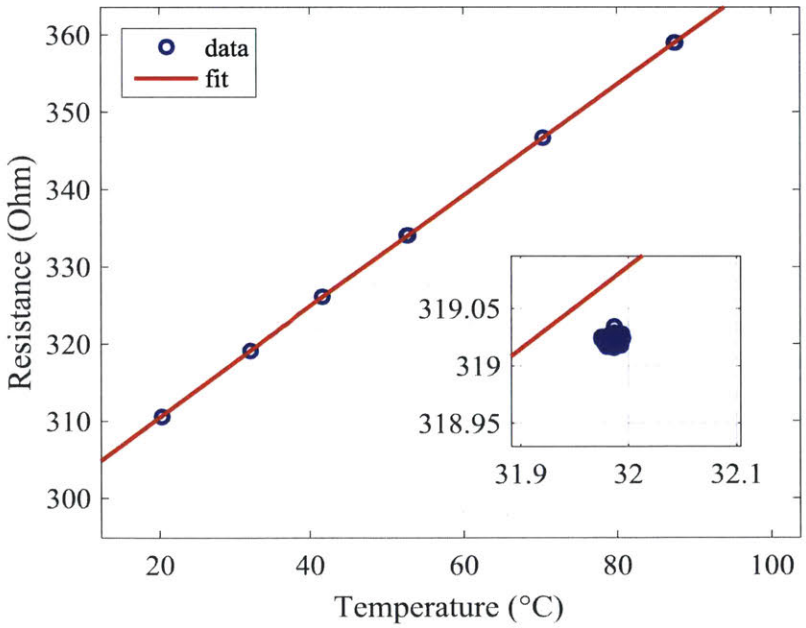

Figure 4-5: Example calibration of RTD-10 for Sample G. The linear fit has a good correlation with less than 0.1 K deviation from the measured temperature as shown in the insert at 32 °C.

Error Propagation

We estimated the uncertainty in temperature measurement using custom RTDs by accounting for a combination of four factors:

1. **Error in the reference thermocouple.** As specified by the manufacturer, ± 0.5 K in the range of 0 to 125 °C.

2. **Error in measuring electrical resistance of RTDs.** As specified by data acquisition hardware (NI 9226, National Instruments), ± 0.02 K.

3. **Resistance of wire trace on sample.** The RTDs were intended to measure changes in temperature at precise locations in proximity to the heaters. The highest resistance in the RTD circuit was where the metal pattern was serpentine and narrow, only 2 - 3 µm wide. While the wires connecting the sample to the DAQ card had a negligible resistance of ~1 Ω, the metal trace leading from the contact pad to the serpentine section, as defined by the RTD design in Figure 3-4, had a finite resistance. Since the ratio of trace-to-serpentine resistances was up to 25:1, it follows that the actual temperature could diverge from the calibrated value by up to 4% if the temperature of the serpentine pattern changed but the trace did not. From modeling conduction in the substrate, the temperature of the trace was expected to rise half as high as the serpentine section, so the maximum deviation was ±0.02 K per degree temperature rise.

4. **Temperature non-uniformity during the calibration.** The sample was calibrated in the environmental chamber which is made of stainless steel, insulated with 3.2 mm fiberglass cloth and heated using adhesive polyamide heaters with four independent PID temperature controllers (Omega, CN-7800). During calibration, the temperatures measured at the sample, sample holder, and liquid tubes were observed to span 1.3 °C at 80 °C, implying that there may be temperature gradients during calibration. This uncertainty was represented by ±0.022 K per degree which corresponds to a gradient of 0 K at room temperature and 1.3 K at 80 °C.

In summary, the uncertainty in temperature measurements was $\pm(0.52 + 0.042 \cdot \Delta T)$ K. As shown in Section 4.4, this uncertainty was acceptably low to draw conclusions from the experimental data.

4.2 Procedure

After calibration, the sample was mounted in the sample holder which was then mounted inside the environmental chamber. The chamber was wiped cleaned with acetone, methanol

and isopropyl alcohol, then sealed and evacuated with a two-stage rotary vane pump (Adixen, Pascal Series 2010SD) until a base pressure of 1 Pa is reached. Between the chamber and the vacuum pump was a cold trap filled with liquid nitrogen to prevent vacuum pump oil mist from entering the chamber and to prevent liquid in the chamber from entering the pump. After base pressure was reached, the valve to the vacuum pump was closed and the vapor supply valve to the reservoir was opened, filling the chamber with saturated vapor. Next, the liquid supply valve was opened, filling the inlet tube, liquid channels, outlet tube, flow meter, and throttle valve with liquid. When the working fluid had filled all of the liquid channels and the temperatures had stabilized, the sample was ready for evaporation experiments.

System Priming

A priming procedure was used to initialize thin film evaporation from the nanoporous membrane. Specifically, the vapor channel needed to be cleared of excess liquid for proper vapor removal at the membrane surface, as shown in Figure 4-6. Before priming, pressurized liquid was forced through the pores and drained off the side of the sample. Figure 4-7 shows the sample temperature, heat flux, inlet pressure and outlet flow rate over time during priming. After heat was applied to the sample, the inlet liquid valve was closed and liquid ceased to flood over the membrane allowing the excess liquid in the vapor channel to dry up. When the liquid-vapor interface reached the membrane surface, thin film evaporation began and the sample temperature dropped. Capillary forces stabilized the meniscus at the membrane pores to maintain thin film evaporation. At this point, the liquid supply valve was opened, corresponding to a rise in inlet pressure in Figure 4-7c, and liquid did not re-flood the vapor channel as long as the liquid was still evaporating. If the priming heat flux was too high, the sample temperature would rise too quickly before the excess liquid could dry and liquid in the manifold channels would boil. For methanol using sample H with 0.04 cm^2 of heated area, a heat flux of 300 W/cm^2 can be used for priming without boiling in the manifold channels. Figure 4-7b shows the heat flux during priming was 290 W/cm^2 and after priming it was increased to 680 W/cm^2.

Stable Operating Conditions

The device can only function if the inlet and outlet conditions are properly set. If the inlet pressure, P_{in}, is too high, liquid will flow out of the membrane faster than it can be evaporated, leading to a flooding failure. The meniscus cannot stabilize in an advancing state if the liquid exhibits a wetting contact angle ($< 90°$), a ubiquitous property of dielectric liquids. Conversely, if the inlet pressure is too low, nucleation is more likely to occur, particularly in the manifold where channel size effects are less effective in suppressing nucleation. The

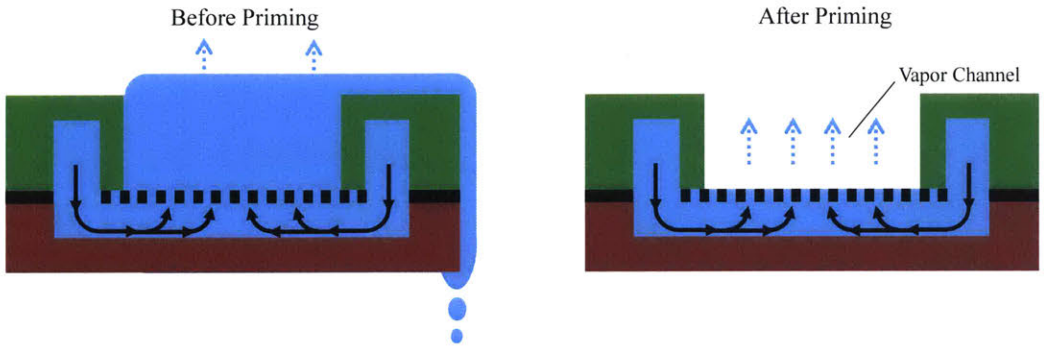

Figure 4-6: Between experiments liquid flows out of the membrane, flushing out contaminants. To begin a new experiment, the excess flooded liquid must be removed by a priming procedure involving evaporation at low heat flux.

onset of these instabilities can be calculated and summarized in a regime map for a given working fluid, device geometry and operating conditions.

Flooding at high inlet pressures is a mechanical instability which can be determined in a method similar to the hydrodynamic model in Section 2-1. If the liquid pressure in the membrane, $P_{\text{liq,mem}}$, is greater than the vapor pressure above the membrane, the device will flood:

$$P_{\text{liq,mem}} - P_{\text{vap}} < 0 \tag{4.1}$$

$$P_{\text{liq,mem}} = P_{\text{in}} - \Delta P_{\text{non-evap}} - \Delta P_{\text{pore}} \tag{4.2}$$

The liquid pressure under the membrane can be calculated based on the pressure drop in the non-evaporating segment of the ridge channel, $\Delta P_{\text{non-evap}}$, and pore, ΔP_{pore}, which are both low Reynolds number flows (Re=10 and 0.01, respectively).

$$P_{\text{in}} < P_{\text{vap}} + \Delta P_{\text{non-evap}} + \Delta P_{\text{pore}} \tag{4.3}$$

$$\Delta P_{\text{non-evap}} = \frac{28.4 \mu \dot{m} l_{\text{wall}}}{\rho h^4} \tag{4.4}$$

$$\Delta P_{\text{pore}} = \frac{32 \mu \dot{m} t_m}{\rho d_{\text{pore}}^4} \tag{4.5}$$

where l_{wall} is defined in Figure 4-8. In this system, the mass flow rate is governed by the

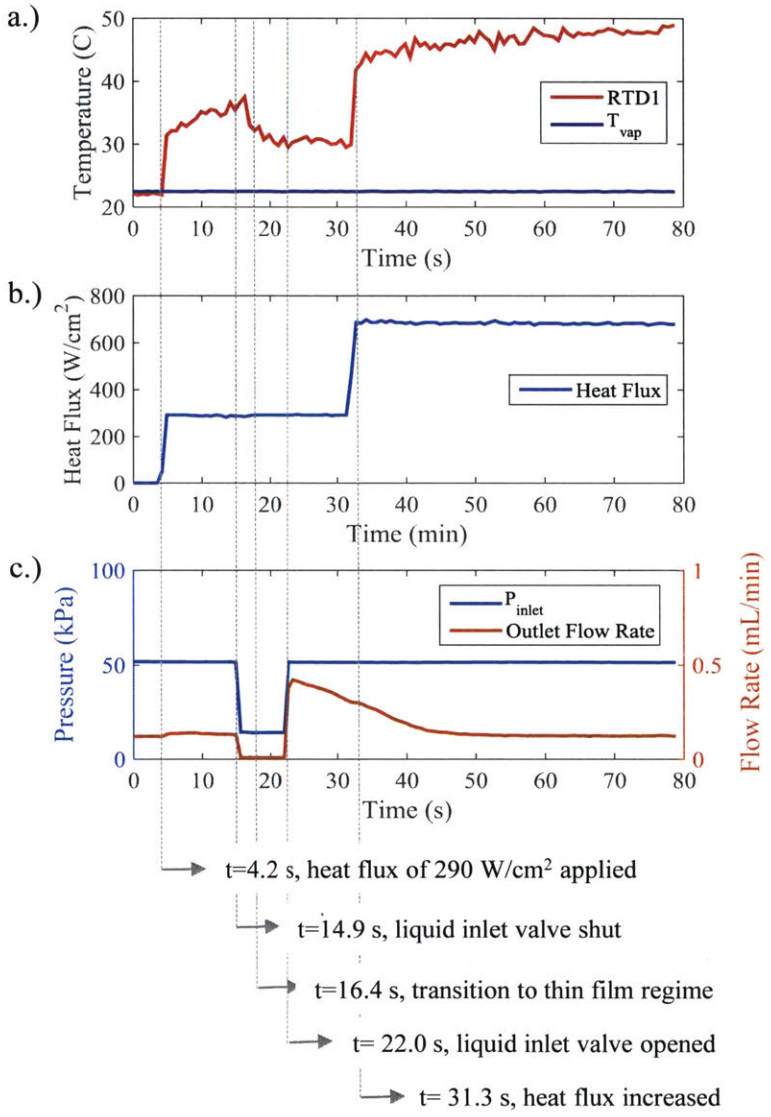

Figure 4-7: a.) Time series of temperature during priming procedure to start system in thin-film evaporation using methanol. b.) A low heat flux is applied and c.) the outlet flow rate and inlet pressure drop as the liquid supply valve is closed to evaporate excess liquid which has flooded the membrane. The liquid interface recedes and pins at the membrane surface, transitioning to thin film evaporation accompanied by a drop in temperature. The liquid supply is resumed and heat flux can be increased.

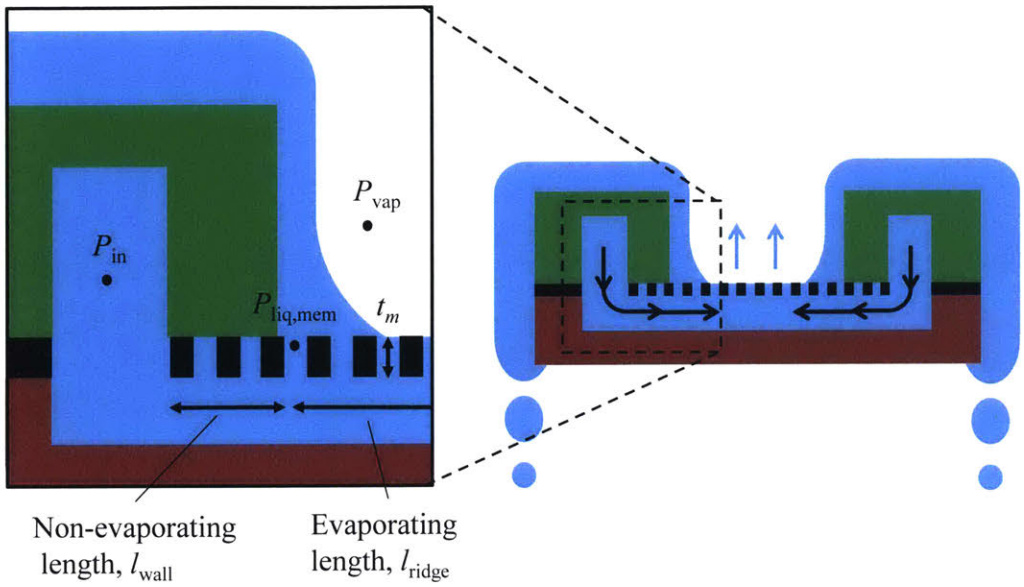

Figure 4-8: The manifold pressure, P_{in}, needs to be selected such that liquid does not flood the membrane. The onset of flooding depends on the pressure drop along the non-evaporating length of channel, l_{wall}, and the pressure drop is determined by the evaporative heat flux.

evaporative heat flux since flow to the pores is capillary driven, *i.e.* self regulating.

$$\dot{m} = \frac{q'' l_{ridge} h}{2 h_{fg}} \tag{4.6}$$

where μ is viscosity, $\dot{m}$ is mass flow rate in a single ridge channel, l_{wall} is the non-evaporating length of the ridge channel (see Figure 4-8), ρ is density, h is height and also the width of the ridge channel, t_m is thickness of the membrane and d_{pore} is diameter of the pore. Finally, the inlet pressure, P_{in}, for stability can be expressed as a function of the applied heat flux (Eq. 4.7).

$$P_{in} < P_{vap} + \frac{q'' l_{ridge} h}{2 h_{fg}} \left(\frac{28.4 \mu l_{wall}}{\rho h^4} + \frac{32 \mu t_m}{\rho d_{pore}^4} \right) \tag{4.7}$$

where l_{ridge} is the evaporating length of the ridge channel and h_{fg} is the latent heat. The results are plotted in Figure 4-9 as the blue curve which delineates the boundary between Region I when the system is prone to flooding instability and Region II when the system is stable.

The second instability which must be considered when prescribing inlet conditions is due to boiling in the manifold and occurs when the inlet pressure fails to suppress nucleation because it is lower than the local saturation pressure (Eq. 4.8). The local saturation pressure is

a function of the manifold wall temperature, which can be estimated using the thermal model in Section 2.2. If the substrate thickness is small, the wall temperature can be estimated using the overall heat transfer coefficient, h, from the base of the ridge to ambient vapor. This method is similar to Hsu's model [36] which describes the onset of nucleation in pool boiling based on the surface temperature, which is governed by natural convection. However, whereas the onset of nucleate boiling occurs at $\Delta T \approx 5\,^{\circ}\mathrm{C}$ and $5\,\mathrm{W/cm^2}$, the onset of boiling in ridge channels is expected at higher heat fluxes due to a high heat transfer coefficient, low dissolved gas concentration and surface tension effects which suppress nucleation.

$$P_{\text{in}} < P_{\text{sat}} = fn\left(T_{\text{manifold}}\right) \tag{4.8}$$

$$T_{\text{manifold}} = \frac{q''}{h(T)} + T_{\text{vap}} \tag{4.9}$$

As shown in Figure 4-9, the green data points from experiments do not cross the boundary of flooding instability but several experimental data points cross the boundary of boiling instability. Although Eq. 4.9 accurately describes the upper bound of inlet pressure for stability, the lower bound is not a strict criterion because liquid can exist in a metastable, supersaturated state. Nonetheless, the lower bound is a useful starting point for experimentally determining the lower limit of inlet pressure.

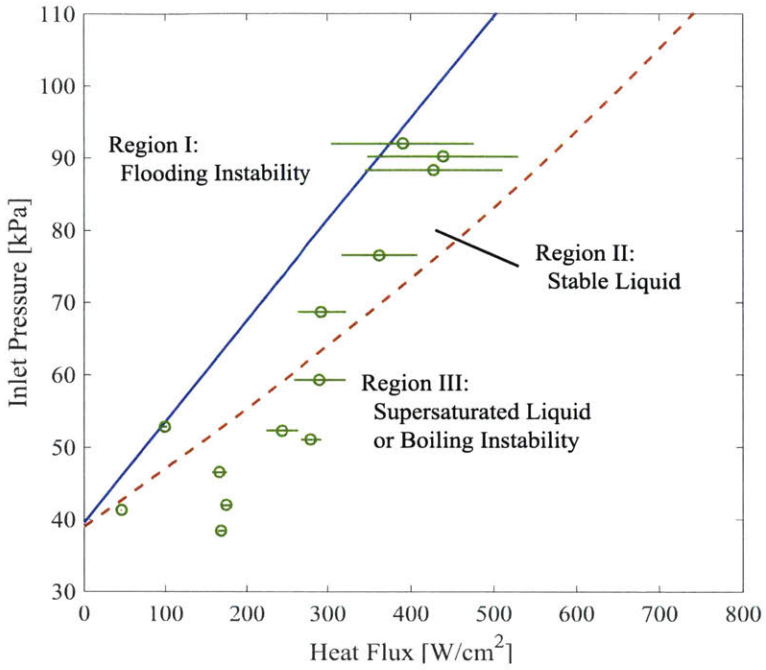

Figure 4-9: Regime map for evaporation with methanol using sample H. If the inlet pressure is too high, liquid will flood the membrane. Conversely, if the inlet pressure is too low, liquid in the manifold channels will boil and the membrane will dry out.

4.3 Data Analysis

From an experiment such as the one shown in Figure 4-7, it is desired to capture behavior of the system during thin film evaporation. Specifically, the temperature rise of the substrate and heat dissipation by evaporation can be used to calculate the overall heat transfer coefficient.

Because of the unsteady nature of the experiment due to clogging in the membrane, as described in Section 4.6, true steady state is never reached. Therefore, to make use of the data, we performed an analysis of characteristic time scales as summarized in Table 4-1 to validate that the temperature gradients in the sample resembled steady state behavior even though the membrane was slowly clogging and the parasitic heat loss was unsteady. The values in Table 4-1 are calculated for methanol at a typical heat flux of 600 W/cm^2. The problem is less severe at lower heat flux because the time to clog pores is longer while the time to heat the sample holder does not change with heat flux.

Based on these values, the best time to capture temperature rise and heat flux data is after the sample has reached a steady temperature distribution ($t \gg 1$ s) but before clogging has caused significant degradation in evaporation ($t \ll 300$ s). Since the sample holder takes more time to reach a steady temperature distribution than the time it takes for the

Table 4-1: Order-of-magnitude estimates for relevant time scales during experiment calculated with methanol using a relatively high heat flux of 600 W/cm^2 to represent a worse case scenario.

Time Scale	**Formula**	**Value**	**Notes**
time to heat sample	$t_s = \frac{m_s c_p \Delta T}{\dot{Q}} = \frac{(1.31)(0.7)(25)}{(24)}$	1 s	Assuming sample is adiabatic and spatially uniform in temperature, m_s is mass of sample in grams
time to prime	$t_p = \frac{h_{\text{vap.ch.}} \rho_{\text{liq}} h_{\text{fg}}}{q''} = \frac{(0.065)(0.77)(1100)}{(600)}$	0.1 s	Assuming all of applied heat is transferred to liquid in vapor channels, $h_{\text{vap.ch}}$ is the height of the vapor channel (0.065 cm)
time to dry out	$t_d = \frac{h_{\text{ridge}} \rho_{\text{liq}} h_{\text{fg}}}{q''} = \frac{(2 \times 10^{-4})(0.77)(1100)}{(600)}$	3×10^{-4} s	Assuming liquid recedes from membrane pores and liquid in ridge channels is evaporated without re-supply from manifold
time to clog pores	$t_c = \frac{h_{\text{ridge}} \rho_{\text{liq}} h_{\text{fg}}}{q'' \chi_c} = \frac{(2 \times 10^{-4})(0.77)(1100)}{(600)(1 \times 10^{-6})}$	300 s	The time to completely fill membrane and ridge channels with contaminants, assuming uniform distribution accumulates in ridge channel, χ_c is volumetric concentration of contaminants
time to heat sample holder	N/A	2000 s	Experimentally determined during dry heating, see Figure 4-10

membrane to clog, special consideration is required to estimate the transient behavior of parasitic heat loss to the sample holder as described in the next section.

Heat Flux Measurement

While the heat applied to the sample is measured accurately to $\pm$ 0.01 W/cm^2 using a digital multimeter (2001, Keithley), the portion of applied heat flux that is dissipated by evaporation, sensible cooling and parasitic conduction needs to be estimated to make appropriate comparisons between the data and model since the model accounts for only heat transfer by evaporation.

Sensible Cooling

The fraction of applied heat that is dissipated by sensible cooling can be be estimated using experimentally determined quantities and Eq. 4.10, which is derived from conservation of energy:

$$q''_{SC} = \frac{\dot{m}\ c_p}{A}\left(T_{\text{outlet}} - T_{\text{inlet}}\right) \tag{4.10}$$

$$\dot{m} = \dot{m}_{\text{evap}} + \dot{m}_{\text{bypass}} \tag{4.11}$$

$$\dot{m}_{\text{evap}} = \frac{q''_{\text{evap}} A}{h_{fg}} \tag{4.12}$$

where q''_{SC} is the heat flux due to sensible cooling, $\dot{m}$ is the total inlet mass flow rate, c_p is the specific heat capacity, $\dot{m}_{\text{evap}}$ is the evaporated mass flow rate, $\dot{m}_{\text{bypass}}$ is the outlet mass flow rate, and A is the area of the membrane. Since q''_{evap} is being used to calculate q''_{SC} to estimate q_{evap}, Eq. 4.12 needs to be computed iteratively. Using this method, it is assumed that the liquid flowing through the manifolds cools the sample uniformly across the heated area and that the heat transfer coefficient is high enough ($\sim 10^4$ W/m^{2}K) that $T_{\text{outlet}} \approx T_{\text{sample}}$. In reality, there is slightly higher sensible cooling near the inlet due to entrance effects, but the error introduced with this estimate is low since the sensible cooling is a small fraction of the total applied heat.

Parasitic Heat Loss

Since the time for the membrane to clog ($\sim$ 300 s) is faster than the time for the sample holder to reach a steady temperature profile ($\sim$ 2000 s), the sample temperatures do not reach a true steady state. Thus, the parasitic heat loss is unsteady. To account for the time-dependent heat loss, an effective heat transfer coefficient for the heat loss is experimentally

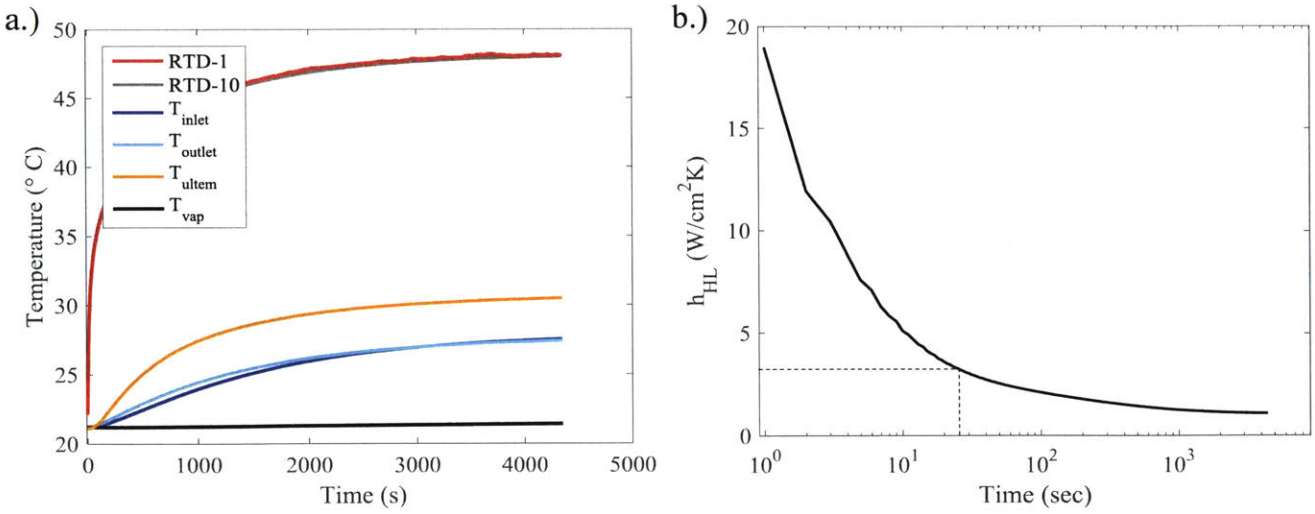

Figure 4-10: a.) Temperature response during heating at 0.6 W or 30 W/cm^2 in dry atmosphere to determine parasitic conduction. b.) Effective heat transfer coefficient for heat loss as a function of time based on the RTDs used to measure temperature during the evaporation experiment (RTD-1 and RTD-10). At $t = 26$ seconds, the parasitic heat loss during evaporation is 3.2 W/cm^2 for every degree of temperature rise.

determined by applying a constant heat flux to the sample in a dry atmosphere and recording the rise in temperature over time as shown in Figure 4-10a. Rather than build a finite element model to capture 3-D spreading effects in the Ultem sample block, copper contact pins, Viton gaskets and stainless steel tubes and then make assumptions about contact resistances, we can experimentally determine the heat losses through the multiple pathways by heating the sample in a dry atmosphere. An effective heat transfer coefficient, h_{HL}, for the unsteady heat conduction is

$$h_{HL} = \frac{q''_{HL}}{T_{\text{dry}} - T_\infty} \tag{4.13}$$

where q''_{HL} is the heat loss during heating in dry atmosphere, T_{dry} is the temperature of the sample as measured by the RTDs while heating in dry atmosphere, and T_∞ is the ambient temperature. The sample temperature rise, T_{dry}, was experimentally measured using RTD-1 with a constant applied heat of 0.6 W and is shown in Figure 4-10a. The heat transfer coefficient representing the parasitic loss was calculated using Equation 4.13 and the result is shown in Figure 4-10b.

The heat loss estimate using Figure 4-10 is a good approximation for a single step rise in heat flux. In most experiments, there are two or more step rises in heat flux corresponding to the priming procedure described in Figure 4-7. The heat loss estimate can be calculated as a piecewise function for each rise in heat flux. Figure 4-11 and Eq. 4.14 give an example of a

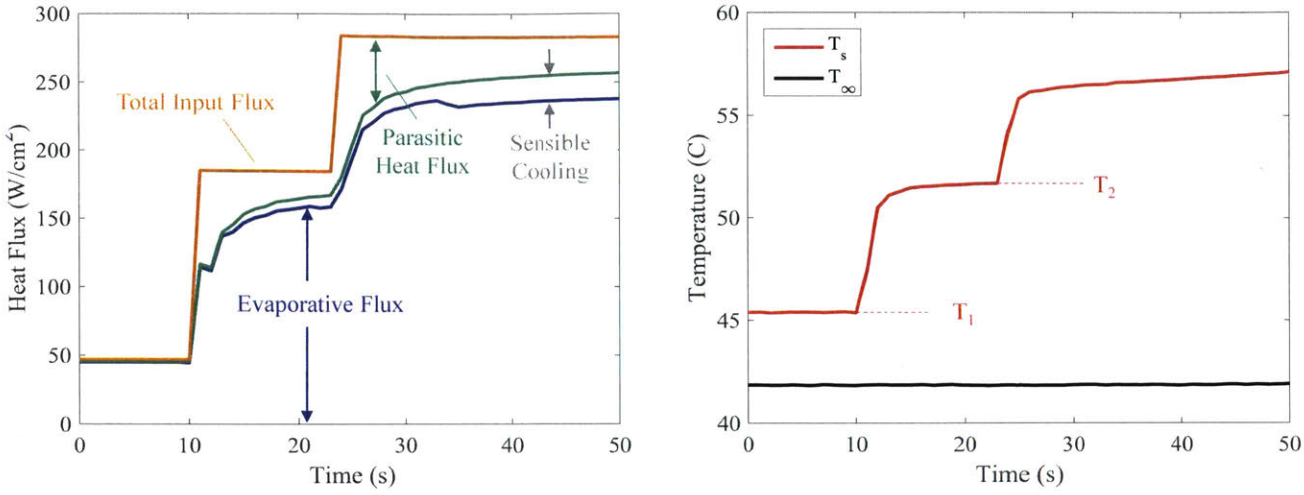

Figure 4-11: Transient heat loss calculation for multi-step increase in heat flux with methanol using sample H.

three step rise in heat flux and the parasitic loss at each point in time. The first step occurs at $t = -247$ s, therefore the parasitic loss is nearly constant when $0 < t < 9$ s. When the heat flux rises at $t = 9$ s and $t = 21$ s, the parasitic loss quickly decays over ~ 10 s, thus the evaporative flux increases. The parasitic heat loss is calculated using this stepwise procedure for every experiment. Since the sample takes ~ 3 s to reach a steady temperature, data is averaged between 6 - 30 s after a step in heat flux to capture steady evaporation, aside from parasitic loss. Six data points over six seconds are time-averaged to reduce random error in measurements. Between each experiment, the sample holder is allowed to cool for 5 minutes.

$$q_{HL}(t) = \begin{cases} h_{HL}(t+247)\cdot(T_s - T_\infty) & t < 9 \\ h_{HL}(t+247)\cdot(T_s - T_\infty) + h_{HL}(t-9)\cdot(T_s - T_1) & 9 \le t < 21 \\ h_{HL}(t+247)\cdot(T_s - T_\infty) + h_{HL}(t-9)\cdot(T_s - T_1) + \ldots & t \ge 21 \\ \qquad\qquad h_{HL}(t-21)\cdot(T_s - T_2) & \end{cases} \tag{4.14}$$

Uncertainty in Evaporative Heat Flux

The uncertainty in calculating evaporative heat flux is a combination of three factors: the accuracy in measurement of applied heat flux, the accuracy of calculating sensible cooling and the accuracy of calculating parasitic loss. The applied heat flux is known with high accuracy according to the voltage and current measurement with a maximum error of ± 10 mV and

± 2 mA, respectively, using a multimeter (2001, Keithley). The major source of error in calculating sensible cooling loss comes from measuring outlet liquid flow rate using the Alicat L-series flow meter. The measured outlet flow rate has a full scale accuracy of 0.04 mL/min with water. For other liquids, the full scale flow rate is proportional to the ratio of liquid viscosities. For example, $\mu_{\text{water}}/\mu_{\text{pentane}} = 4.3$, so the flow accuracy is 0.17 mL/min with pentane. The evaporative flow rate must be calculated iteratively because it is based on the total uncertainty in the heat flux. The sensible cooling error is propagated according to Eq. 4.10.

At early time scales ($\sim$100 s), parasitic heat transfer to the sample holder resembles conduction to a semi-infinite body. During calibration of the parasitic heat loss, a constant heat flux is applied to the sample, which is then absorbed by the sample holder. During an experiment, most of the applied heat is dissipated by evaporation, therefore the sample temperature is dictated by evaporation and the boundary condition, as seen by the sample holder, resembles a step rise in temperature. In the solution for heat conduction into a semi-infinite body, the ratio of $q_s''/(T_s - T_\infty)$ for a constant heat flux boundary condition is 57% smaller than the ratio for a constant surface temperature boundary condition [53], where q_s'' and T_s are the surface heat flux and surface temperature, respectively. That is, the heat transfer at the surface is dependent on the thermal history. Furthermore, the experiment and calibration involve unique thermal histories with respect to the boundary condition. Therefore, even with perfect measurements of temperature over time, the calculation used to account for parasitic heat loss is not exact. The error in calculating parasitic heat loss is bounded by 57%, the difference in the extreme cases. Since the parasitic heat loss accounts for only 7 - 24% of the total heat dissipation using the methods described above, the error in calculating evaporative heat flux is only 4 - 14% which is low enough to validate the experimental performance.

Temperature Measurement

The calibrated RTDs were observed to drift by up to 0.9 °C between calibration and experiments, a time period spanning 1 - 2 days, and by up to 0.3 °C during an experiment, a time period spanning 3 - 6 hours. The drift may be caused by changes in electrical contact resistance, which is not a function of temperature. The recorded RTD temperatures were offset by the average drift during the experiment in order to measure $\Delta T = T_{\text{RTD}} - T_{\text{vapor}}$ accurately, particularly at low heat flux. Without the correction, the data would imply $\Delta T = -0.5$ °C at 15 W/cm^2, which violates the second law of thermodynamics.

The vapor temperature matched room temperature during evaporation because the chamber walls were effectively a condenser with a very large area (0.3 m^2). However, when the chamber was heated for conducting experiments at elevated temperature, the vapor temper-

ature was not isothermal. Regions inside the chamber contain superheated vapor, due to non-uniform heating of the chamber walls. The temperature rise of the sample should be compared to saturated vapor conditions which can be calculated using the vapor pressure measured by the capacitance manometer and interpolation of the saturation curve. The interpolated saturation temperature was in good agreement with measured RTD temperatures when the sample was unheated and filled with saturated liquid, thus acting like a wet bulb at 100 % relative humidity.

Device-Level Model

The ridge-level model described in Section 2.2 captures heat conduction in the ridge and membrane, but assumes a substrate thickness of only 2 µm. In contrast, the samples had a substrate thickness of 650 µm, therefore heat spreading and conduction resistances must be accounted for. At the membrane surface, a heat transfer coefficient boundary condition was applied to the device-level model using the overall heat transfer coefficient from the ridge-level model (Figure 2-5) rather than simulating 5,000 ridge channels and 1 billion pores on a full device. For further computational efficiency, only a reduced area in the center 2 mm × 11.2 mm of the device was included in the model as shown in Figure 4-12, where spreading effects are significant. For even further computational efficiency, only one quarter of the the reduced area was simulated. The input heat flux boundary condition at the back side reflects the serpentine pattern of the heater. The four heating zones are clearly visible in Section B-B and the spreading effects of the serpentine pattern are faintly visible in the inset image. The handle wafer and manifold channels were not included in the model domain. The substrate temperatures were extracted from the model and represented by T_{back}, which corresponds to the exact location of each RTD according to Figure 3-4.

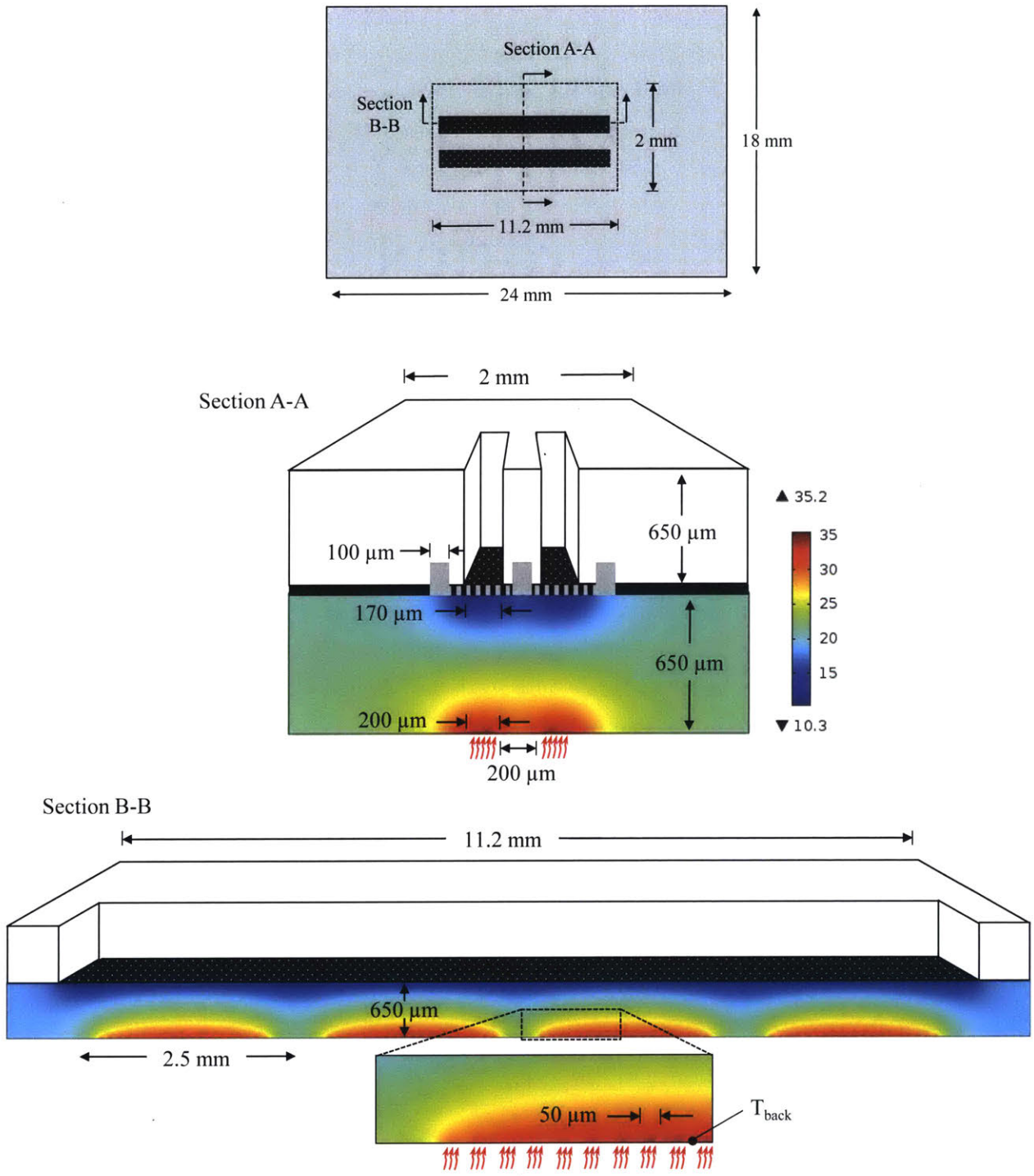

Figure 4-12: Device-level model to account for heat spreading effects for sample with 2 vapor channels. The model captures conduction in an area only 2 mm × 11.2 mm where heat spreading is important, but for computational efficiency the actual domain was only 1 mm × 5.6 mm due to quarter symmetry. The input heat boundary condition was applied in the shape of a serpentine pattern. The handle wafer (white) and manifold channels (gray in Section A-A) were not included in the model but are shown for illustration. The output of the model was the temperature rise at the specific location of the RTD on the substrate, T_{back}.

4.4 Results

We performed experiments with five different working fluids: water, isopropyl alcohol (IPA), methanol, pentane and R245fa with $T_v = 22\,°C$. Data is also reported for water and methanol at $T_v = 52\,°C$ and $T_v = 42\,°C$, respectively. The experiment configurations are summarized in Table 4-2. Methanol and IPA were tested using sample H with 2 vapor channels, which was cleaned using a 3:1 solution of H_2SO_4:H_2O_2 to remove residual, organic contaminants from previous experiments. Pentane and R245fa were tested with sample G with 1 vapor channel. Water was tested with sample K with 25 vapor channels. Samples G and K were tested directly after fabrication and were not cleaned immediately before experiments.

Samples with smaller membranes were more practical for tests at high heat flux because the total power was low, only 15.1 W for sample G. If the sample dries out at 15 W, the temperature will rise by approximately 15 °C per second which was enough time to turn off the heaters before causing damage to the sample and experimental apparatus. However, samples with smaller membranes had large parasitic heat loss relative to the membrane or heater area. For fluids such as pentane and R245fa, the overall heat transfer coefficient of evaporation was large compared to the effective heat transfer coefficient corresponding to parasitic loss. Conversely, water had a low overall heat transfer coefficient, so it was tested using sample K which had a larger heater area and therefore lower parasitic heat transfer coefficient.

In each figure, the experimental data is plotted with two curves that represent bounds of the device-level model. The bounds are determined by an upper and lower value of liquid area fraction, ξ, as described in Figure 2-6. The upper value corresponds to the case where the liquid meniscus spreads beyond the diameter of the pore, *i.e.* $\xi \to 1$. The lower value corresponds to the case where the meniscus is pinned inside the pore, *i.e.* ξ is equal to the porosity of the membrane as measured by the images in Figure 3-14.

Table 4-2: Summary of experiments: samples with small membrane area are better suited for fluids with high heat transfer coefficients.

Sample	**Membrane Area**	**Fluids Tested**	T_v	$h_{HL}(t = 10\text{ s})$
G	0.017 cm^2	Pentane	22 °C	5.6 W/cm^2K
		R245fa	22 °C	
H	0.032 cm^2	Methanol	22 °C, 42 °C	2.2 W/cm^2K
		IPA	22 °C	
K	0.424 cm^2	Water	22 °C, 55 °C	0.28 W/cm^2K

Alongside each plot of ΔT vs. q'' is a bar graph representing the order of experiments and breakdown of evaporative cooling, sensible cooling and parasitic cooling for each data point. During evaporation, contaminants accumulated in the membrane and then between experiments, contaminants were flushed out of the membrane. The bar graph validates that the there was no hysteresis between experiments that may be caused by clogging in membranes.

The same data from Figures 4-13, 4-14, 4-15 and 4-16 are organized by sample and plotted again in Figure 4-17 where the shaded regions represent the bounds of the model based on liquid area fraction. The comparison of evaporation using different working fluids or different vapor temperatures demonstrates the change in overall heat transfer coefficient while keeping the heat spreading in the substrate constant using the same sample.

Direct comparison of the data from Figures 4-13, 4-14, 4-15 and 4-16 is not appropriate because the heat spreading resistance is unique in each sample. Compensation for heat spreading in the substrate is necessary for proper comparison of the performance of each working fluid. Using the model of Figure 4-12 with experimentally measured heat flux and temperature rise, an overall heat transfer coefficient for the suspended membrane structure can be estimated. The results are shown in Figure 4-18. Fluids with high volatility, such as pentane, R245fa and methanol, demonstrated one order of magnitude higher heat transfer coefficients compared to fluids such as water and isopropyl alcohol. Since the membrane and ridge geometries are nearly identical for each sample, the results demonstrate that transport at the liquid-vapor interfacial is the dominant resistance to heat transfer. Furthermore, the overall heat transfer coefficients for pentane and R245fa exceed the program goals of 33 W/cm^{2}K which is needed to dissipate 1000 W/cm^2 with a temperature rise $\Delta T < 30$ K. The highest heat transfer coefficients occur at low heat flux when the liquid spreads to cover a large area fraction ($\xi \rightarrow 1$). The heat transfer coefficients are observed to decrease with rising heat flux, which is attributed to a change in wetting morphology as well as clogging in the membrane. For a clog-resistant device, the heat transfer coefficient is expected to stabilize at high heat flux when the liquid-vapor meniscus is pinned within the pore.

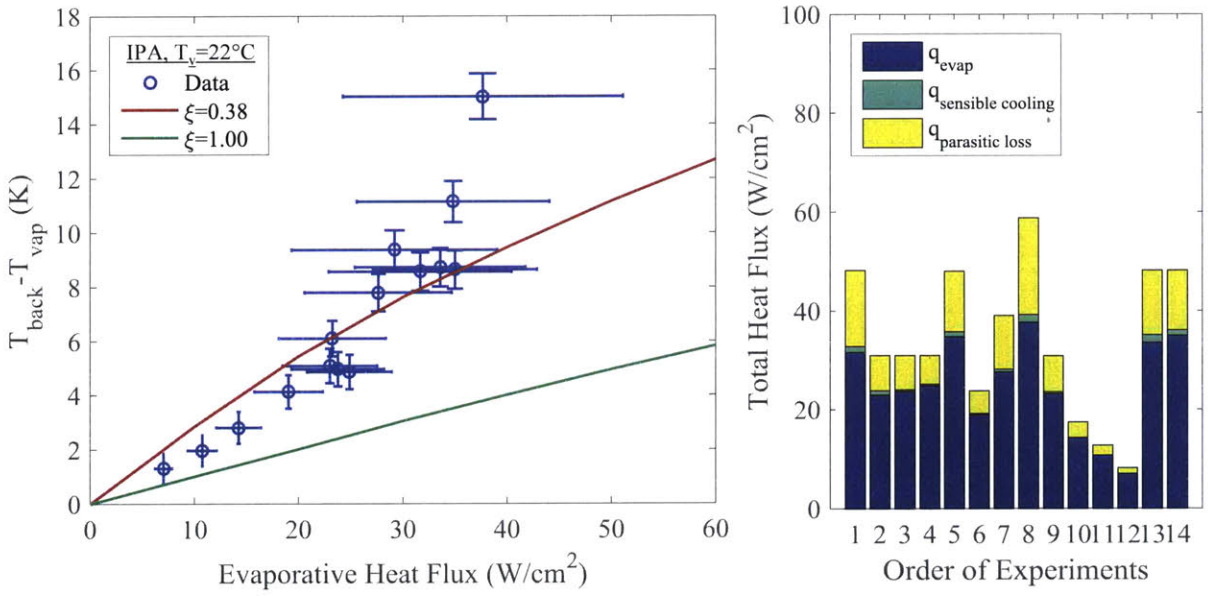

Figure 4-13: Experimental results for sample H (2 channels) with isopropyl alcohol at $T_v = 22\,^{\circ}\mathrm{C}$ after accounting for parasitic and sensible cooling.

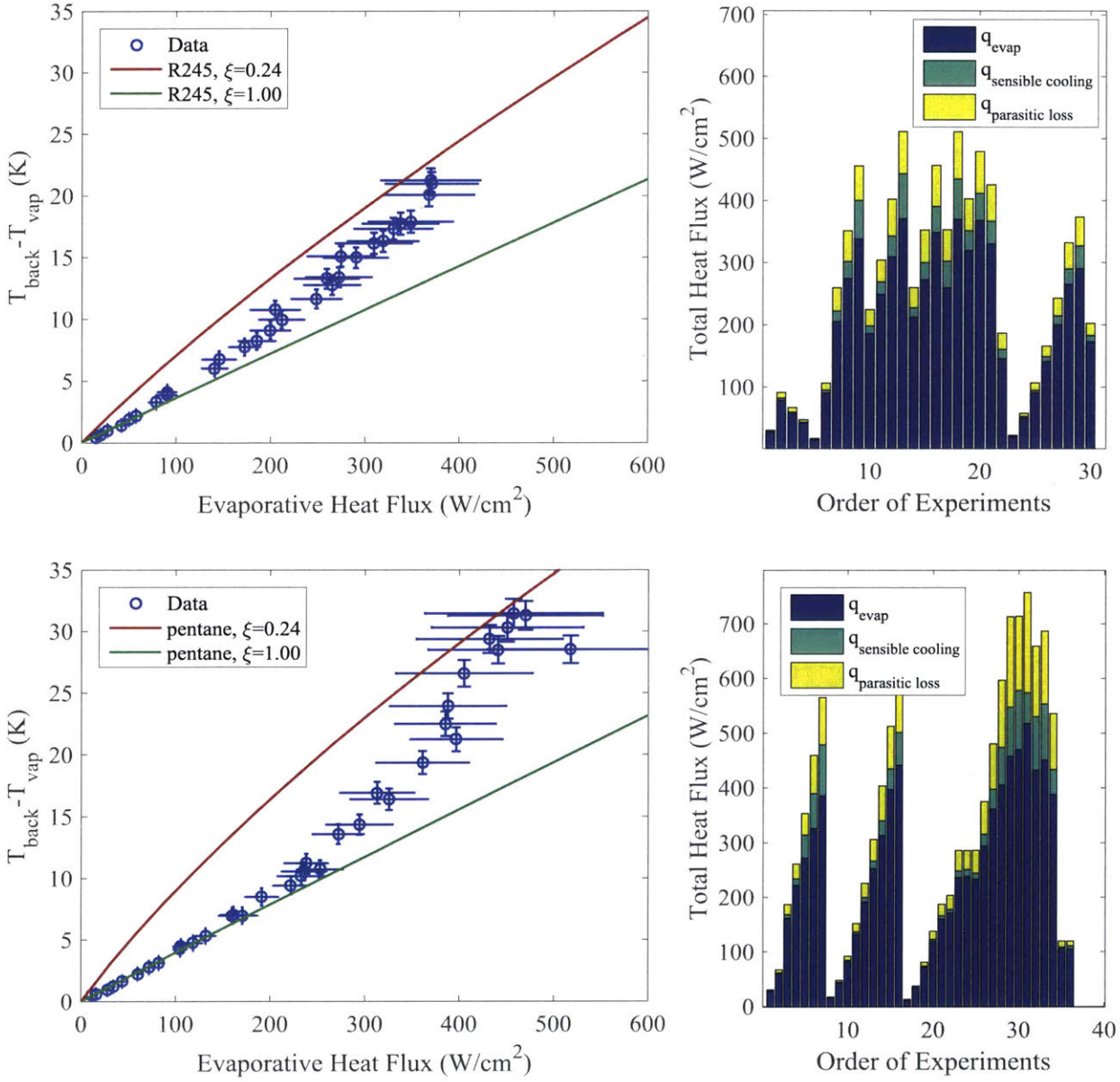

Figure 4-14: Experimental results for sample G (1 channel) with R245fa and pentane at $T_v = 22\,^{\circ}\mathrm{C}$ after accounting for parasitic and sensible cooling.

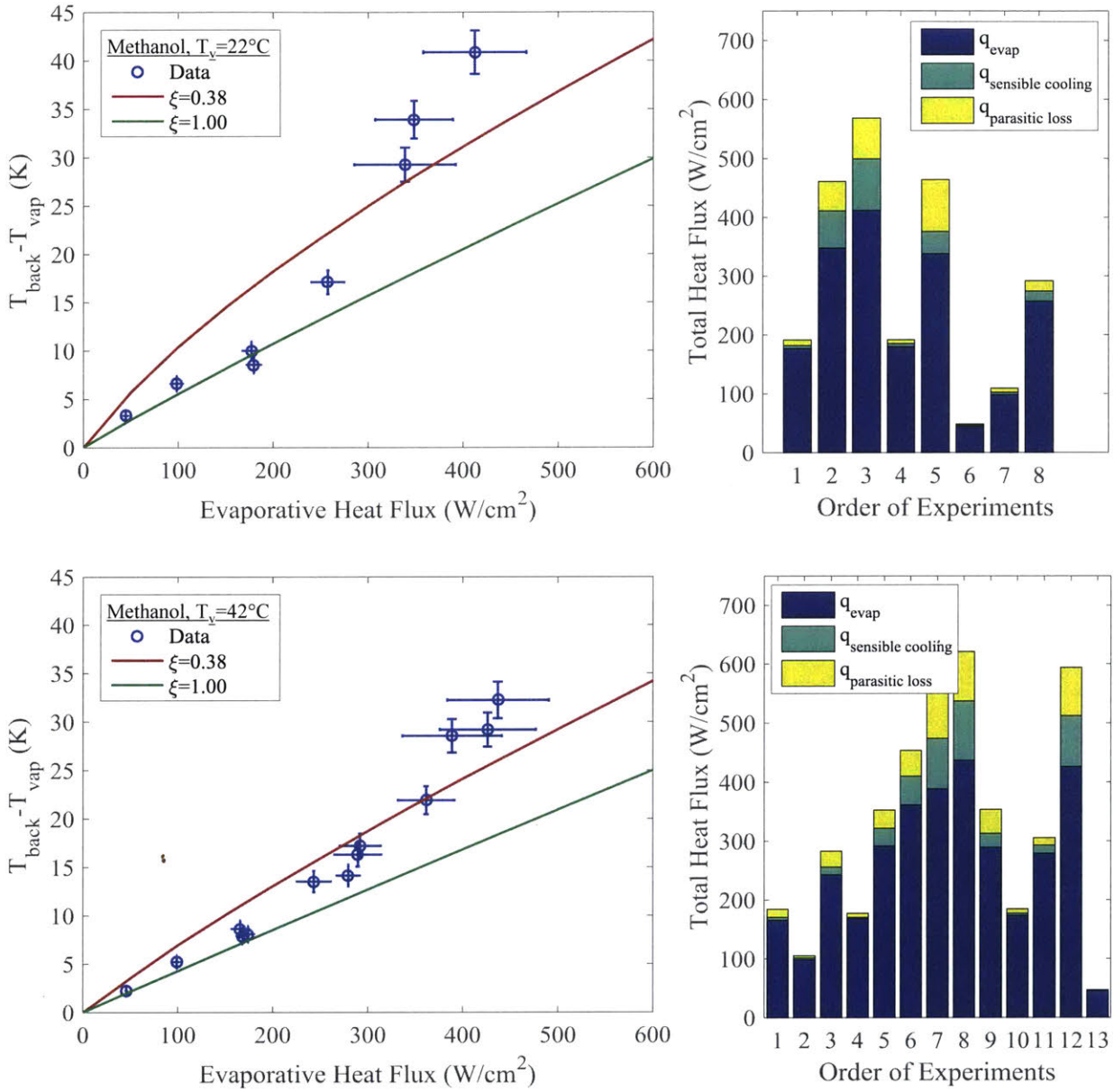

Figure 4-15: Experimental results for sample H (2 channels) with methanol at $T_v = 22\,^{\circ}\mathrm{C}$ and $42\,^{\circ}\mathrm{C}$ after accounting for parasitic and sensible cooling.

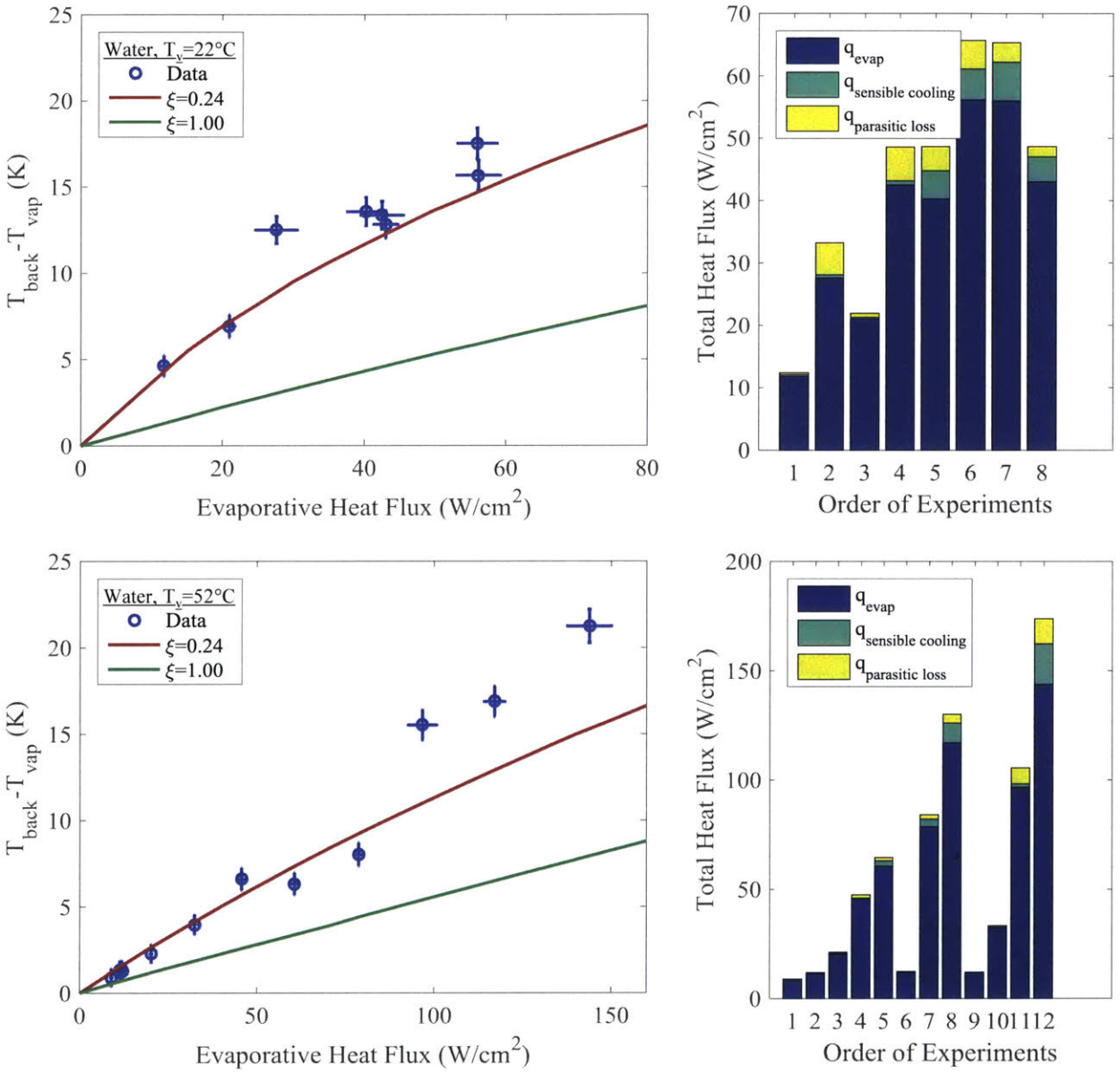

Figure 4-16: Experimental results for sample K (25 channels) with water at $T_v = 22\,^{\circ}\mathrm{C}$ and $52\,^{\circ}\mathrm{C}$ after accounting for parasitic and sensible cooling.

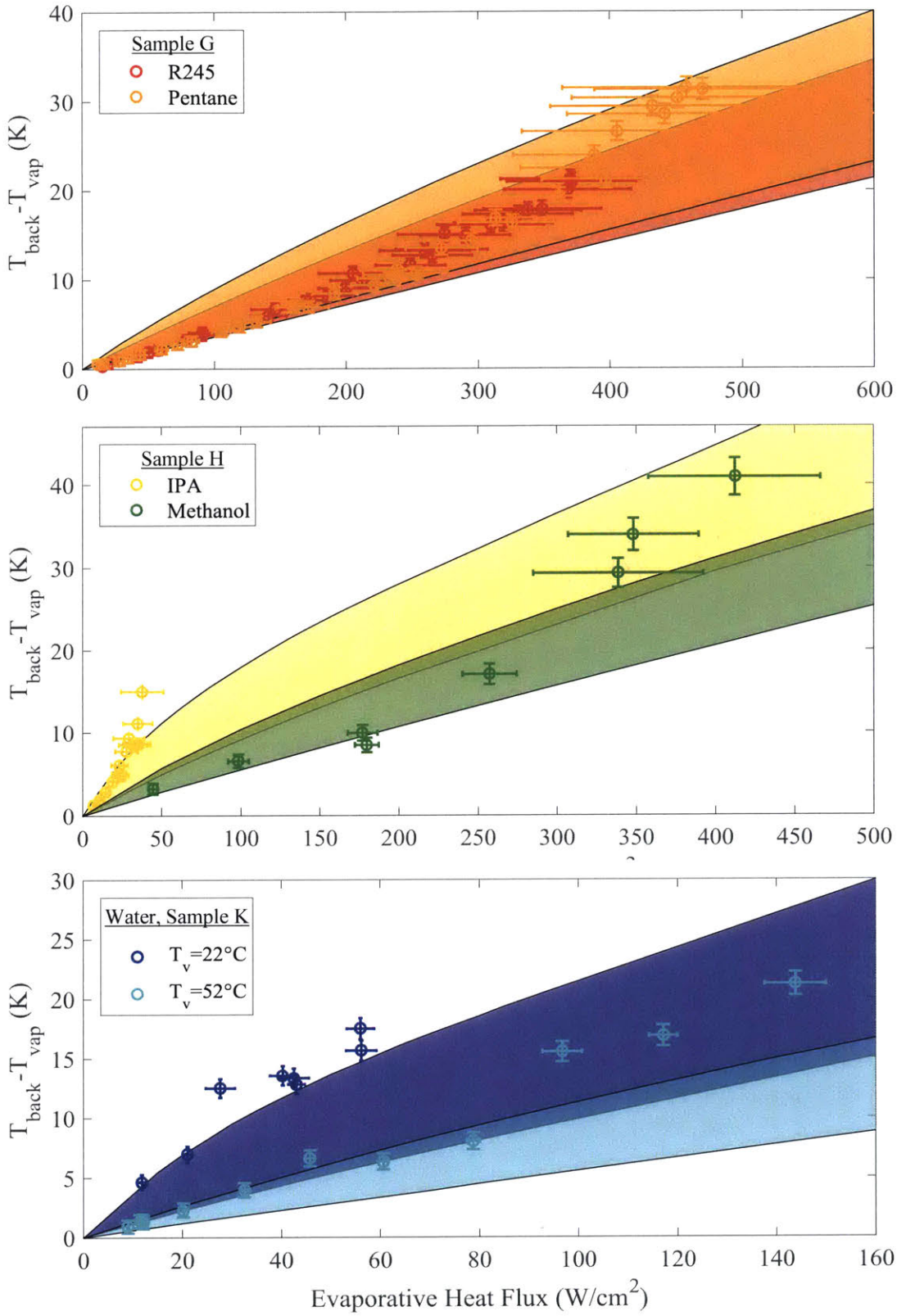

Figure 4-17: Comparisons for each sample. The heat transfer coefficient is related to the figure of merit $\rho_{\text{vap}} h_{fg}$ which is dependent on the working fluid and vapor temperature.

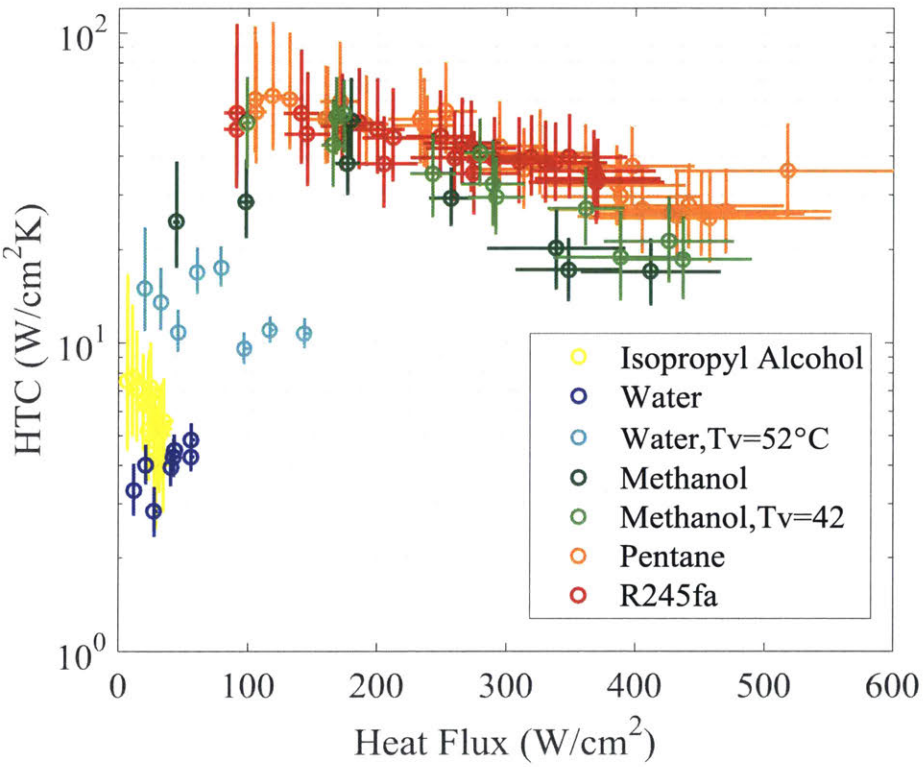

Figure 4-18: Overall heat transfer coefficient calculated using experimentally measured heat flux and temperature rise in combination with heat conduction model from Figure 4-12. The heat transfer coefficient of high volatility fluids such as pentane, R245fa and methanol is an order of magnitude higher compared to isopropyl alcohol and water. The vapor temperature, T_v, for each experiment is room temperature (22 °C) unless otherwise noted.

Experimental Challenges

Challenges encountered during experimental characterization are summarized below:

- The major challenge with experiments was clogging of the membrane due to nonvolatile contaminants. The experimental apparatus was modified by removing plastic wetted components which are prone to leaching. The liquid was distilled with limited success. The sample, sample holder, reservoir and environmental chamber were handled with the utmost cleanliness, yet contamination was still a major issue during experiments.

- Mounting the sample required precise alignment to make contact between pogo pins and gold pads. Precise force was required to seal the Viton or indium gasket to the ports without breaking the sample. The sample was connected to a helium leak detector (ASM-142, Adixen) with tape covering the vapor channels to check for leaks around the gaskets such that the sample could be clamped with the minimum pressure required.

- Current leakage between heater and RTD circuits was a major problem for RTD measurement at high voltage (over 40 V). The cause of current leakage was assumed to be damage to the Si_3N_4 dielectric layer during PECVD, a process which tends to form pin holes. The current leakage caused an artifact in the RTD signal when using a voltage divider to measure the resistance, because the RTD circuit and heater circuits shared a common ground. The issue was corrected by measuring the RTD resistance using the NI 9226 cDAQ which is isolated electrically from the heater circuits.

- The wettability of the membrane to water inhibited flushing of contaminants between experiments. The contact angle was hydrophilic, but not low enough that water would flood the membrane to purge contaminants. As a result, experiments were limited in duration before accumulation of contaminants significantly affected results.

- Control of the inlet liquid pressure was a challenge during priming of the device. Stability of evaporation at the membrane is sensitive to both the magnitude and timing of the inlet pressure during priming. The liquid supply valve (SS-4BRG, Swagelok) was chosen for its all-metal construction and bellows seal of the valve stem, but it is designed for shutoff rather than metering. A metering valve would enable more precise control of the pressure and flow rate.

4.5 Discussion

For all of the experiments, the data fall within the bounds of the model for low heat flux with the exception of water at $T_v = 22\,°C$. As the heat flux rises, the data eventually depart from a linear trend and the slope increases. The data corresponding to the abrupt rise represent a degradation in the heat transfer coefficient as a result of accumulation of soluble, nonvolatile contaminants in the membrane. The adverse effects of clogging are discernible by the unsteady rise of temperature over time, as shown in Figure 4-7, or as a function of heat flux, as shown in Figure 4-20. Contamination affects experiments at all heat fluxes, but the effects are more severe at high heat flux when contaminants accumulate at a higher rate. Therefore, the data at higher heat flux represent evaporation from a partially clogged membrane resulting in a greater slope in temperature vs heat flux compared to the slope at low heat flux. The distinction between "high" and "low" heat flux depends on the working fluid used. For isopropyl alcohol, a sharp increase in temperatures occurred when heat flux exceeds 30 W/cm^2. For pentane and methanol, the increase occurred above 400 W/cm^2. For water, the rise occurred above 60 W/cm^2. The discrepancy may be attributed to a combination of the liquid purity, the contaminant solubility and the volumetric energy density, $\rho_L h_{fg}$. When the accumulation rate of contaminants was too high as identified by the temperature rise rate, the experiments were halted, with the exception of R245fa.

During experiments using R245fa with $q'' > 300$ W/cm^2, the membrane was also observed to clog as identified by a moderate temperature rise rate. However, ultimately the heat flux was limited because the sample could not stabilize beyond 370 W/cm^2 when normalizing the applied heat by the heater area. Since the membrane of sample G is only 172.6 µm wide, the heat flux normalized by the membrane area is 429 W/cm^2. The reason for this limitation of stability may be related to inadequate control of the inlet liquid pressure. Alternatively, this limit may correspond to the critical heat flux, q''_{CHF}, which occurs when the maximum capillary pressure is reached, the meniscus recedes and the ridge channels dry out. According to the hydrodynamic model, the critical heat flux for this sample is expected at 610 W/cm^2. The reason for potentially reaching critical heat flux 29% lower than expected may be due to flow constrictions formed by contaminants or defects in the membrane such as two pores merging into one.

For methanol, R245fa and pentane, the trend in Figure 4-14 at low heat flux is along the boundary where the liquid spreads to cover almost the entire membrane area, *i.e.* $\xi = 1$ as defined in Figure 2-6. However, the trend deviates from the $\xi = 1$ boundary as the heat flux increases beyond 300 W/cm^2. While the accumulation of contaminants is definitely responsible for part of the rise, the liquid spreading may also be a factor. When the heat flux is low, the meniscus radius of curvature needed for capillary pumping of liquid is high relative to the pore radius. As the heat flux increases, the capillary radius decreases to pump

more liquid to the membrane. As the capillary radius decreases, the interface must recede into the membrane where it can be supported by the solid pore walls. When the interface recedes into the pores, ξ decreases and the temperature transitions from the green curve ($\xi \to 1$) to the red curve ($\xi = 0.24$). This trend is most distinguished in the cases of pentane and R245fa.

In the case of water, a different trend is observed as shown in Figure ??. The reason for higher temperature rise than expected may be due to an accommodation coefficient lower than unity or may be due to the absence of liquid spreading. While most nonpolar fluids have an accommodation coefficient $\hat{\sigma} \approx 1$, values reported for water range from 0.02 to 1.0 [43]. The accommodation coefficient, $\hat{\sigma}$, is related to the probability of liquid molecules at the interface escaping into the vapor phase when they reach sufficient energy. Equivalently, $\hat{\sigma}$ is related to the probability that a vapor molecule condenses into the liquid phase when it impinges onto an interface rather than reflecting. It is analogous to the emissivity of a surface in radiative heat transfer. Since there is controversy in the literature over the actual value of $\hat{\sigma}$, especially for water, all model simulations are conducted with $\hat{\sigma} = 1$. A concurrent reason for the higher temperature rise may be related to liquid spreading and the contact angle, θ, of water on the membrane surface. If the contact angle for water is $\theta = 45°$ as observed on surfaces made of silicon and exposed to air, the liquid is unlikely to spread, thus the liquid area fraction will be confined to the pores, *i.e.*, $\xi = 0.24$. From the available data it is impossible to discern the cause for higher temperature rise, however, the data is compelling that water is a low performance working fluid in this system with $h \approx 3.5$ W/cm^{2}K compared to pentane with $h \approx 27$ W/cm^{2}K at low heat flux.

According to the thermal model of Section 2.2, the figure of merit for maximizing heat transfer coefficient is the product of the saturated vapor density, ρ_{vap}, the latent heat, h_{fg}, and the molecular speed, $\sqrt{RT}$. There are two ways to change this figure of merit: by changing the working fluid and by changing the ambient temperature. Water and methanol were tested at room temperature and at elevated vapor temperature.The heat transfer coefficient is expected to be higher at elevated temperature as a result of much higher vapor density and only slightly lower latent heat. Indeed the heat transfer coefficient was observed to increase for water at $T_v = 52\,°\text{C}$ and for methanol at $T_v = 42\,°\text{C}$ as predicted by the thermal model. Additionally, data for isopropyl alcohol and methanol demonstrate a sharp contrast in heat transfer coefficient, which corresponds to a large difference in $\rho_{\text{vap}} h_{fg} \sqrt{RT}$. Moreover, the experimentally determined heat transfer coefficients from pentane and R245fa are almost identical because $\left(\rho_{\text{vap}} h_{fg} \sqrt{RT}\right)_{\text{R245fa}} \approx \left(\rho_{\text{vap}} h_{fg} \sqrt{RT}\right)_{\text{pentane}}$.

A maximum evaporative heat flux of 518 W/cm^2 over 0.02 cm^2 at ΔT=28.3 K was recorded using pentane as a working fluid before the experiment was halted due to contaminant accumulation. To our knowledge, this is the highest heat flux in pure evaporation of

any fluid and the highest heat transfer coefficient for a dielectric fluid. Furthermore, similar performance was observed with R245fa, a nonflammable, dielectric fluid. More importantly, a new regime of thin film evaporation was demonstrated in which conduction in the liquid film is insignificant. Rather, molecular emission at the liquid-vapor interface determines the rate of heat transfer.

4.6 Clogging of Membranes

Evidence for clogging during evaporation due to accumulation of nonvolatile contaminants was based on experimental observations of temperature rise and images of clogged membranes after experiments. A model was developed to understand the transport of contaminants in the pores and ridge channel in order to design a device that is resistant to contaminants.

The experimental trend in the data, for example that in Figure 4-13, resembles the behavior during boiling when the CHF is reached: temperatures rises abruptly at a finite heat flux. However, the limitation occurring during evaporation from nanopores is distinctly a consequence from the mechanism of clogging in the membrane, as shown in Figure 4-19. Unlike temperature rise due to CHF, a temperature rise due to clogging occurs at any heat flux.

Figure 4-20a shows the rise in temperature over time during evaporation with methanol at a relatively low heat flux of 48 W/cm^2. At this heat flux, even if dryout were to occur in the membrane, the capillarity of the ridge channels is high enough to wick liquid back into the ridge channels and membrane pores. Therefore, the temperature rise can only be attributed to clogging by nonvolatile contaminants. The temperature rise rate from the data set in Figure 4-20a is plotted as a function of heat flux in Figure 4-20b along with several other data sets at various heat fluxes. At higher heat fluxes, the temperature rise rate increases with $(q'')^2$. To understand this scaling behavior, we considered the temperature rise which changes over time as the membrane clogs. Taking the derivative with respect to time and applying the chain rule:

$$\Delta T = T_s - T_v = \frac{q''}{h(t)} \tag{4.15}$$

$$\frac{\partial T_s}{\partial t} = -\frac{q''}{h^2}\frac{\partial h}{\partial t} \tag{4.16}$$

where T_s is the sample temperature measured by the RTD. Assuming that the heat transfer coefficient h decays linearly with accumulation of contaminants, $\dot{m}_c$, by some proportionality

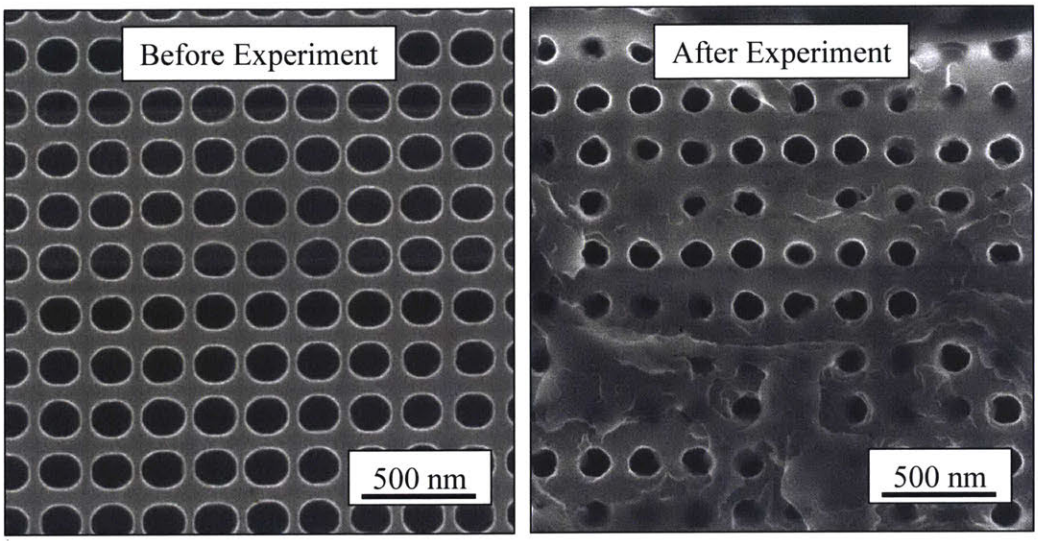

Figure 4-19: Images with scanning helium ion microscope of membranes from sample H before and after evaporation with methanol.

constant A,

$$\dot{m}_{\text{total}} = \dot{m}_{\text{evap}} + \dot{m}_c \approx \dot{m}_{\text{evap}} \tag{4.17}$$

$$\dot{m}_c = \dot{m}_{\text{evap}}\chi_c = \frac{q''}{h_{fg}}\chi_c \tag{4.18}$$

$$h(t) = h_o - A\int \dot{m}_c dt = h_o - A\int \frac{q''\chi_c}{h_{fg}} dt \tag{4.19}$$

$$\frac{\partial h}{\partial t} = -A\frac{q''\chi_c}{h_{fg}} \tag{4.20}$$

where $\dot{m}_{\text{total}}$ is the total mass flow rate, $\dot{m}_c$ is the mass flow rate of contaminants, $\dot{m}_{\text{evap}}$ is the mass flow rate of working fluids, and χ_c is the concentration of contaminants. Using a first order approximation, $h(t) \approx h_o$. Then combining Eq. 4.16 and 4.20:

$$\frac{\partial T_s}{\partial t} \approx \frac{q''}{h_o^2} A \frac{q''\chi_c}{h_{fg}} \tag{4.21}$$

$$\frac{\partial T_s}{\partial t} \propto (q'')^2 \tag{4.22}$$

Before the concept of evaporation from nanoporous membranes can be implemented for electronics cooling, higher heat flux must be dissipated for longer duration. While the problem of contaminant accumulation limits heat flux and longevity in the prototype devices of this thesis, it is a problem that can be addressed with a new design involving bypass flow

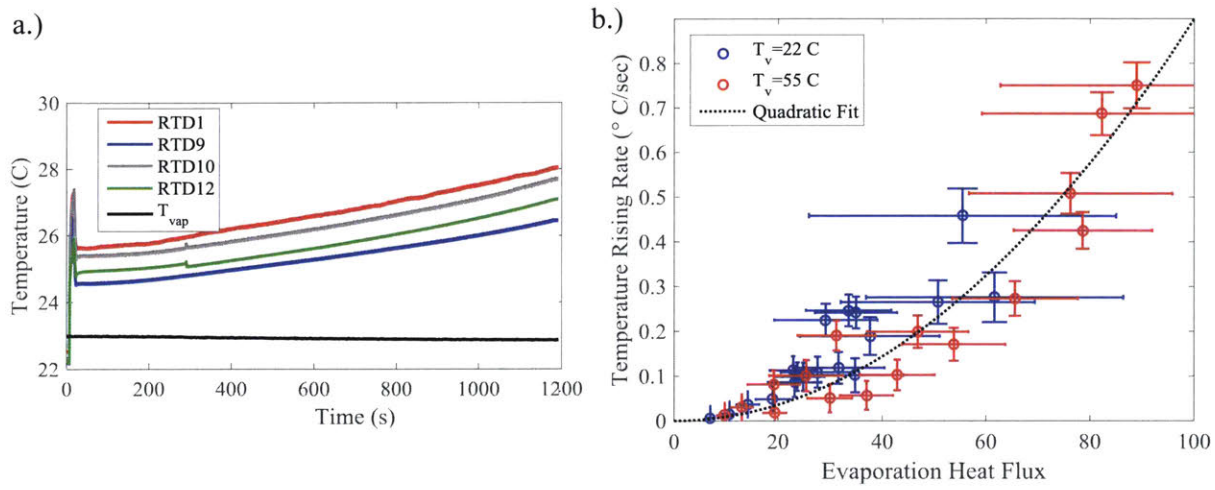

Figure 4-20: a.) Substrate temperature rise over time during evaporation with methanol at 48 W/cm^2 using sample H. b.) Temperature rise rate due to clogging during evaporation with isopropyl alcohol using sample H.

in the ridge channels, which is described in Section 5.3.

Contamination Model

With a high surface-to-volume ratio, microfluidic devices are plagued by contamination that is present in commonplace environments. The samples fabricated and tested for this thesis were designed without detailed consideration for accumulation of contaminants in the membrane. After observation of clogged membranes after evaporation and degradation of performance during evaporation, a model was developed to understand the physics of contaminant transport within the device and suggest a new design which is resistant to clogging.

There are two types of contamination that can potentially clog the membranes: particles that are insoluble in the working fluid and nonvolatile molecular compounds that are soluble in the working fluid (e.g., hydrocarbons or salts). Solid particles can be separated from the working fluid using an external filter. However, the current contamination issue is with nonvolatile, soluble contaminants. As the contaminants build up in the supported membrane evaporation device, a concentration gradient forms, as shown schematically in Figure 4-21.

As liquid flows into the ridge channels and membrane pores during evaporation, there are two competing transport effects: advection of contaminants carried within the working fluid and diffusion of contaminants against the advective flow. A balance of advective and diffusive flux can be achieved at steady state through design of an appropriate fluid network using a model of contaminant transport in the pores and ridge channels. The steady state

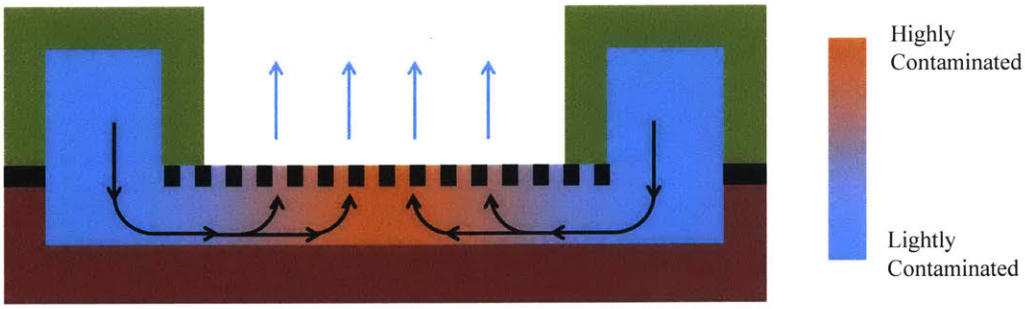

Figure 4-21: Schematic of contaminant accumulation during evaporation. Contaminants enter the ridge channel by advection from a stream of lightly contaminated liquid. As the contamination builds up, a concentration gradient forms.

concentration profile of the contaminant is governed by the Maxwell-Stefan equation:

$$\nabla \chi_c = -\frac{\chi_w N_c - \chi_c N_w}{c D_m} \tag{4.23}$$

where χ_c is the molar fraction of the contaminant, χ_w is the molar fraction of the working fluid, N_c is the molar flux of the contaminant, N_w is the molar flux of the working fluid, c is the total molar concentration of the solution and D_m is the Maxwell-Stefan diffusivity. Although the composition of contaminants is not known, a diffusivity of $D_m = 1 \times 10^{-9}\,\mathrm{m}^2/\mathrm{s}$ is assumed, a typical value in liquids [54]. The Maxwell-Stefan equation is the more general form of the classical Fick's diffusion theory. It describes the transport phenomena for liquid binary mixtures without the dilute solution assumption for either one of the species [55]. At a steady state, N_c is zero based on the continuity equation, since the time variation of $c\chi_c$ is zero at a steady state and N_w is dictated by the evaporative flux (or the heat flux dissipated by the device).

$$\nabla \cdot N_c + \cancelto{0}{\frac{\partial (c\chi_c)}{\partial t}} = 0 \tag{4.24}$$

$$N_c = 0 \tag{4.25}$$

$$N_w(y) = \frac{q''}{\phi h_{fg} M} \tag{4.26}$$

where M is the molar mass of contaminant. By solving equation 4.23 for χ_c within the pore and applying the boundary condition $\chi_c(y = 0) = \chi_{c,0}$, the solution form is an exponential

rise in concentration χ_c as a function of the position along the pore, y:

$$\chi_c(y) = \chi_{c,y=0} \exp\left(\frac{q''y}{\rho_L \phi h_{fg} D_m}\right) \tag{4.27}$$

where ρ_L is the density of the liquid and $\rho_L = cM$. The concentration of contaminants is greatest at the surface of the membrane, $y = t_m$.

$$\chi_{c,max} = \chi_{c,y=0} \exp\left(\frac{q''t_m}{2\rho_L \phi h_{fg} D_m}\right) \tag{4.28}$$

where t_m is the thickness of the membrane or equivalently the length of the pore. For pentane at $q'' = 500$ W/cm^2, $\phi = 0.378$ and $t_m = 600$ nm, the contaminant concentration rises by a factor of 10^{16} across the membrane. By similar analysis, the contaminant concentration as a function of the position in the ridge channel, x, can also be estimated using one dimensional analysis since $L \gg h$:

$$N_w(x) = \frac{q''L}{2\rho_L h_{fg} h} \frac{(L/2 - x)}{L/2} \tag{4.29}$$

$$= \frac{q''(L/2 - x)}{\rho_L h_{fg} h} \tag{4.30}$$

$$\chi_c(x) = \chi_{c,x=0} \exp\left(\frac{q''x(L - x)}{2\rho_L h_{fg} D_m h}\right) \tag{4.31}$$

$$\chi_{c,max} = \chi_{c,(x=L/2)} \exp\left(\frac{q''L^2}{8\rho_L h_{fg} D_m h}\right) \tag{4.32}$$

where L is the total length of the channel and h is the height of the ridge channel. The maximum rise in concentration occurs at the middle of the ridge channel $x = {}^{L}/_{2}$. For pentane with $q'' = 500$ W/cm^2 and $h = 2\,\mu$m, the concentration rises by a factor of 10^{1290}. In total, the concentration rise is 10^{1306}, indicating that diffusion will never balance advection of contaminants with the current channel configuration. For a liquid purity of 1 ppm as specified by the chemical supplier, the fraction of contaminants at the interface is over 1 which is unphysical. The time scale to reach steady state in the pore (t^*_{pore}) and ridge

channel (t^*_{ridge}) can be estimated by:

$$t^*_{\text{pore}} = \frac{t_m^2}{D_m} \tag{4.33}$$

$$= 3.6 \times 10^{-4}\,\text{s} \tag{4.34}$$

$$t^*_{\text{ridge}} = \frac{(L/2)^2}{D_m} \tag{4.35}$$

$$= 10\,\text{s} \tag{4.36}$$

Evaporation experiments with liquid pentane from sample H lasted for $\sim$ 30 seconds with a 40% rise in temperature. The predictions for steady state concentration profile in the pore and time to reach steady state do not agree with experimental observations. A recent study with evaporation at 600 W/cm^2 using FC-72 from nanopores that were 50 µm long did not report clogging [56]. A separate study with evaporation at 90 W/cm^2 using isopropyl alcohol from nanopores that were 100 µm long did not report clogging [28]. It is possible that the nonvolatile contaminants actually have evaporation rates that are one million times lower than pentane. For example, the vapor pressure of vacuum pump oils is well documented and falls within the range of 10^{-7} to 10^{-2} Pa at 25 °C. Therefore, the assumption that the flux of contaminants equals zero (Equation 4.26) breaks down. Without knowing the composition of contaminants, the precise distribution remains unknown. However, using the assumption that the contaminants do not evaporate provides a conservative estimate for the design of clog-resistant devices.

The vulnerability of the current design is that the ridge channel is too long and the membrane is too thick for diffusion to drive the contaminants out of the membrane. However, if liquid channels can be reconfigured such that the maximum contaminant concentration is at an acceptably low level, there will not be clogging of the membrane. More specifically, if liquid is pumped through the ridge channels such that contaminants are continuously flushed out from under the membrane, there will not be accumulation of contaminants in the ridge channels. The concentration rise in the membrane can be mitigated by decreasing the membrane thickness and increasing the membrane porosity. For pentane at $q'' = 1000$ W/cm^2, $\phi = 0.45$ and $t_m = 200$ nm, the concentration rises by 3.9×10^4 times. For a liquid purity of 1 ppm, this corresponds to a pentane concentration of 96.1% at the liquid-vapor interface. For a first-order estimate of heat transfer performance, it is assumed that the presence of nonvolatile contaminants on the surface blocks the emission of liquid molecules, but the molecules do not interact otherwise. Therefore, translating contamination into degradation in cooling performance, a 3.9% reduction in the interfacial heat transfer coefficient is expected.

4.7 Chapter Summary

A nanoporous membrane evaporation device was experimentally characterized and found to perform in good agreement with predictions from a high fidelity model. Specifically, the experimental data show good agreement with the device-level model for high liquid area fraction when the heat flux is low and good agreement for low liquid area fraction when the heat flux is high, suggesting that liquid spreading is responsible for the trend. A custom environmental chamber was used to test the membrane devices in pure vapor ambient conditions. The liquid used for evaporation was distilled to delay clogging in the membranes. The samples tested had total membrane areas of 0.017, 0.032 and 0.424 cm^2. The back side temperature was measured using custom RTDs deposited on the sample while the ambient vapor temperature was measured with two thermocouples. Evaporative heat flux was calculated by accounting for sensible cooling effects and transient conduction in the sample holder. Five working fluids were tested (isopropyl alcohol, water, methanol, pentane and R245fa) which demonstrated a wide range of interfacial heat transfer coefficients. The highest heat transfer coefficients were with pentane and R245fa which reached 20 ± 2 and 18 ± 3 W/cm^2K at heat fluxes of 370 ± 52 and 518 ± 87 W/cm^2, respectively. The critical heat fluxes and heat transfer coefficients are much larger than the highest reported values of pure evaporation from wicking structures and comparable to boiling from capillary-fed wicking structures. The maximum heat flux was ultimately limited by accumulation of nonvolatile contaminants in the membrane, which was distinguished from CHF in boiling by the occurrence of clogging at low heat flux. Finally, the distribution of contaminants was modeled by analyzing the competing effects of advection and diffusion within pores and ridge channels.

Chapter 5

Conclusions

5.1 Summary of Present Work

Thermal management is a critical limitation to performance of electronics, particularly for devices with high power density such as GaN power amplifiers. Significant improvements in cost, reliability and power density of the electronic devices can be realized with the implementation of a phase change cooling solution capable of dissipating high heat flux with a high heat transfer coefficient and low power consumption. This thesis demonstrates the feasibility of a novel evaporator that utilizes a nanoporous membrane to address these requirements.

The introduction of a nanoporous membrane offers three key advantages for an evaporator: 1. high capillarity for enhancing critical heat flux, 2. reduction in liquid meniscus size to reduce conduction resistance in the liquid and promote thin-film evaporation and 3. capillary pumping to reduce external pumping power requirements. To avoid high viscous resistance associated with nanopores, the membrane is ultra thin (600 nm) and is bonded to a high-permeability microchannel support structure. Traditionally, water is chosen as the highest performing working fluid, but with this bi-porous configuration, the viscous pressure loss through the nanopores is decoupled from the capillarity of the nanopores. Therefore, fluids with relatively low surface tension but high volatility can be used, promising over 10× improvement in the interfacial heat transfer coefficient compared with water, which has low volatility and a low interfacial heat transfer coefficient. A model was developed to predict the critical heat flux based on capillary and viscous pressures and a separate model was developed to predict the overall heat transfer coefficient based on heat conduction and mass transport at the liquid-vapor interface. The complete model informs the choice of working fluid and device geometry. The model results suggest that heat fluxes up to 1.3 kW/cm^2 at $\Delta T = 32.7\,^{\circ}\mathrm{C}$ can be dissipated using pentane, corresponding to a heat transfer coefficient

of 41 W/cm^{2}K, more than double the state of the art devices with any fluid.

To validate the model predictions, samples were fabricated using silicon micromachining and tested experimentally. The performance enhancements of evaporation from suspended nanoporous membranes depend on precise control of the membrane and ridge channel geometries. A single defect in the membrane can lead to dryout, therefore uniformity of the membrane pores is imperative for reaching high heat flux. The membrane was fabricated using interference lithography and reactive ion etching to yield highly uniform pore arrays with 200 nm pitch and 110 - 130 nm diameter. Trenches were fabricated with projection photolithography and deep reactive ion etching to form the ridge channels for liquid supply, which are 2 µm wide and 2 µm deep. The top side of the membrane was fusion bonded to the trenches and then the back side was released to form channels for the vapor to escape. A platinum heater was patterned with photolithography and deposited on the substrate to heat the sample alongside platinum RTDs to measure temperature of the sample. Three samples were successfully fabricated for experiments with total membrane areas of 0.017, 0.032 and 0.424 cm^2.

The samples were tested in a custom environmental chamber with pure vapor ambient conditions that emulated the condenser of a flow loop which would be used in electronics cooling applications. Five working fluids were tested: water, isoproyl alcohol, methanol, pentane and R245fa. HPLC grade liquid was used as the working fluid for its high purity and metal was used for all wetted components (*e.g.,* tubing, filters, valves) to reduce leaching. The liquid was distilled to purify it of soluble, nonvolatile compounds yet issues with contamination still hindered performance, limiting the duration of experiments to $\sim$ 30 s at $q'' \sim 400$ W/cm^2 over 0.017 cm^2. The duration of experiments was long enough for evaporation to reach steady behavior, but not long enough for the parasitic loss to become steady. Nonetheless, a method was developed to predict transient conduction loss and capture performance before significant clogging occurred. From the experimental measurements, unprecedented heat transfer coefficients and heat flux in pure evaporation (without nucleate boiling) were achieved. The results demonstrate that the liquid conduction resistance in 120 nm pores is negligible while the interfacial mass transport dominates the overall thermal resistance.

Although the prototype devices demonstrated high heat dissipation over only 0.017 – 0.032 cm^2, the arrangement of heaters to match the membrane area along with models to capture spreading in the substrate suggest that the concept could be scaled to areas larger than 1 cm^2.

Clogging of membranes by non-evaporating residue was the crucial limitation of the designed devices. Whereas the critical heat flux with pentane was expected to occur at 1.3 kW/cm^2, the maximum observed was only 518 W/cm^2 due to accumulation of con-

taminants. For a nanoporous evaporation device to operate for years at a time, the liquid channels need to be arranged such that contaminants are constantly flushed out of the membrane pores. The mass transport of contaminants in the membrane and ridge channels due to advection and diffusion was investigated and a comprehensive model was developed to advise the design of a clog resistant membrane device.

This thesis experimentally demonstrates the highest recorded heat transfer coefficient with a dielectric fluid and the highest heat flux and heat transfer coefficient in a pure evaporation regime, *i.e.*, without nucleate boiling, for any type of fluid. By leveraging the capillarity and thin film evaporation of liquid in 120 nm pores, the benefits of a highly volatile, dielectric liquid can be exploited. Evaporation from nanoporous membranes has the potential to exceed the performance limitations of traditional heat pipes and vapor chambers and enters a regime in which molecular emission from the liquid-vapor interface is the principle thermal resistance.

5.2 Contributions

The following contributions were made during the completion of this thesis:

- A novel design for enhanced evaporation was proposed. Models were experimentally validated to understand the fluidic transport and thermal transport through the structure. Tools were developed to optimize the heat flux and heat transfer coefficient for a given working fluid, pore size, porosity, membrane thickness and ridge channel size.

- A suspended membrane device was fabricated using interference lithography and silicon microfabrication. The precise control of feature sizes and high uniformity of the membrane were critical in the success of the evaporation device. Potential applications beyond thermal management include chemical detection, chemical separation, desalination and energy storage.

- Proof-of-concept devices were experimentally characterized to investigate the performance and limitations with five working fluids representing a diverse set of thermophysical properties. We performed a priming procedure for repeatable, stable startup. We developed a regime map to identify the proper inlet liquid pressure and flow conditions for stable operation.

- A regime of phase change heat transfer was explored in which the interfacial heat transfer resistance dominates thermal transport and the thermal conductivity in the liquid is negligible. A figure of merit for this regime was identified to define performance for a given working fluid: $M = \rho_{\text{vap}} h_{fg} \sqrt{T/R_s}$, where R_s is the specific gas constant.

- A record high heat transfer coefficient for phase change with any dielectric fluid was demonstrated using pentane (41 W/cm^{2}K) and R245fa (43 W/cm^{2}K). A record high heat flux for any fluid in pure evaporation was achieved using pentane (518 W/cm^2) and R245fa (370 W/cm^2), over 4× higher than the previous record using water in sintered copper wicks.

- A method was developed for calculating transient parasitic heat loss from a silicon sample to the sample holder. This method was used to extrapolate steady state performance without the effects of clogging.

- The effects of clogging by soluble, nonvolatile contaminants were studied and a model was developed to understand transport of contaminants by advection and diffusion in order to design clog-resistant device.

Implications for GaN Power Amplifiers

Significant improvements to power density and reliability of GaN HEMT power amplifiers are possible with the implementation of a monolithic evaporation device with a nanoporous membrane. The mean time to failure for GaN HEMTs is empirically estimated to improve by 2× for every 10 K reduction in junction temperature [57]. Using a state-of-the-art thermal packaging solution with a CuW shim and silicon carbide substrate, an effective heat transfer coefficient of 10 W/cm^{2}K results in a simulated junction temperature of 222 °C. However, using a monolithic silicon evaporator and silicon carbide substrate, we demonstrated experimental heat transfer coefficients over 40 W/cm^{2}K with R245fa and suggested with models that 125 W/cm^{2}K is possible with R134a. With a heat transfer coefficient of 50 W/cm^{2}K, the simulated junction temperature is only 183 °C. The reduction in junction temperature by 39 K can enable an increase in the device power density or lead to 16× improvements in device lifetime.

5.3 Future Work

This proof-of-concept device is a novel approach to phase change cooling and has already demonstrated major improvements in its current form for thermal management applications. However, the technology is in its infancy with many improvements to be explored in the future. The most important aspect for this concept to succeed is the experimental validation of a clog-resistant device. In addition, suggestions for enhanced understanding and enhanced performance are discussed.

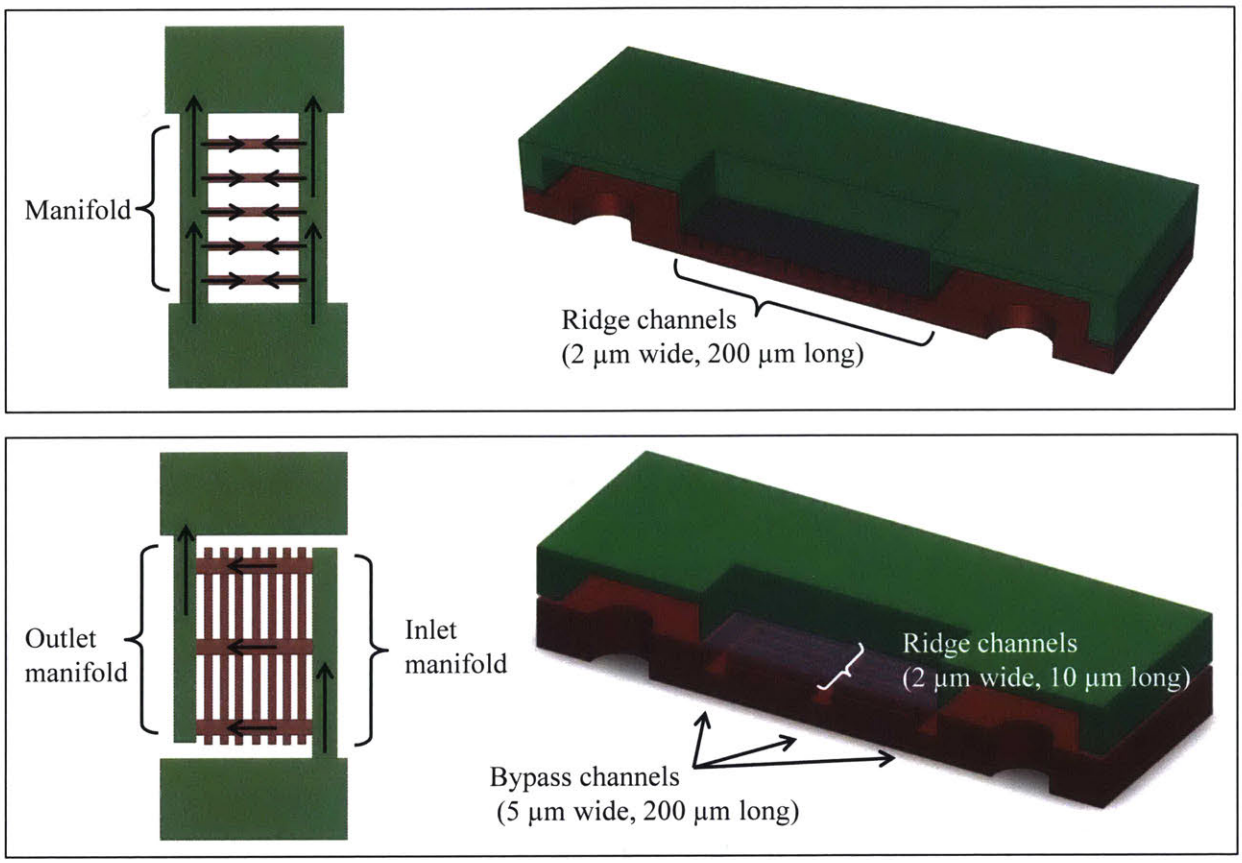

Figure 5-1: Comparison of original ridge channel design to new bypass channel design. By shortening the ridge channels to 10 μm and adding bypass channels, diffusion can balance advection of contaminants which results in a negligible effect on performance.

Clog-resistant Evaporation Devices

To avoid failure due to contamination build-up, the ridge channel must be configured with bypass flow that continuously flushes contaminants. A mass transport model from Section 4.6 suggests that with this geometry, diffusion is effective to discharge contaminants from the membrane against the entrainment flow of liquid. However, with ridge channels only 2 μm wide and 200 μm long, the pressure required to pump liquid through the ridge channels is 1.3 MPa. For this positive pressure differential and a pressure drop of 0.04 MPa through the pores, the membrane will flood. Furthermore, the pumping power requirements are 200× larger than the power to pump liquid through the manifold channels with only a 6 kPa pressure drop. To distribute flow into 2 μm channels over a 200 μm span, another level of liquid supply channel is required. In place of the original ridge channel, these new channels are labeled "bypass channel tier #1" and "bypass channel tier #2". Flow is directed first through the tier #1 channels by separating the previous manifold into an inlet manifold

and outlet manifold, as shown schematically in Figure 5-1. The tier #1 channels connect to either the inlet or outlet manifold, therefore flow is then directed into the tier #2 channels. Rather than integrate the new supply channels into the handle wafer with the manifold channels, both tier #1 and tier # bypass channels can be integrated more compactly into the same wafer as the original ridge channels. By sizing the tier #1 bypass channels 5 µm wide and 20 µm deep, the added pressure drop is only 23 kPa for pentane at 1000 W/cm^2. If the tier 2 channels are 2 µm wide and 2 µm deep, identical to the original ridge channels, but 20 µm long, the added pressure drop is 13 kPa. All together, the highest pressure under the membrane is 42 kPa which is not much higher than the original pressure difference of 6 kPa required to drive flow through the manifold channels.

Even with continuous circulation of liquid in the liquid supply channels, there is still a risk of clogging in the membrane if the pores are too long. Using Equation 4.28, a membrane 100 nm thick with $\phi = 0.45$, $q'' = 1000$ W/cm^2, inlet purity $\chi_{c,o} = 1$ ppm and pentane as the working fluid, the maximum impurity concentration is 3.9%. To prevent flooding across such a thin membrane, the pore diameter needs to be less than 34 nm to maintain a pressure drop of 42 kPa. With these modifications, the bypass channel design is expected to operate at steady state indefinitely as long as the inlet liquid is below 1 ppm nonvolatile impurity concentration. Furthermore, with liquid pumped through a bypass channel network, the critical heat flux before dryout is not dependent on the ridge channel geometry but rather the membrane thickness, pore diameter and fluid properties. For a pumped configuration with pore diameter of 34 nm and membrane thickness of 100 nm, the theoretical critical heat flux from Equation 2.12 is 12.8 kW/cm^2 with R134a compared to a theoretical critical heat flux of only 320 W/cm^2 using the fabricated samples with pore diameter of 120 nm and thickness 600 nm.

Suggestions for Enhanced Understanding

Experimental validation of the contaminant diffusion model is necessary to design robust devices which are resistant to clogging. Uncertainty regarding the composition of contaminants in each working fluid, the diffusion rate and solubility of each contaminant make it difficult to accurately predict when a membrane will clog. To characterize clogging behavior, a nonvolatile compound with a known solubility and diffusion coefficient could be added to a working fluid to validate the mass transport model. Similarly, low concentrations of a low volatility compound such as isopropyl alcohol could be added to methanol for evaporation. As methanol quickly evaporates, the remaining liquid is mostly isopropyl alcohol and the substrate temperature will rise.

The highest heat flux recorded during experiments was confirmed to be higher than conventional wicks with pure evaporation, but the dryout limits were not reached due to

accumulation of contaminants. To validate the dryout limit even before addressing the clogging issue, samples with larger pores, narrower ridge channels or longer ridge channels could be used for which the anticipated dryout limit is lower.

The test conditions for experimental validation were designed to mimic the operation of an evaporator in a loop. For full characterization, the evaporator should be evaluated in series with a condenser. A loop will demonstrate the true performance of this technology for applications where size, weight and power are critical. If the membrane device is integrated into a loop with a compressor, the high vapor quality ($x = 1$) and steady evaporation should benefit the performance and reliability compared to a two-phase compressor for flow boiling with ($x < 1$).

At low heat flux, the heat transfer coefficient is high due to the liquid spreading to cover a larger liquid area fraction ($\xi \to 1$). To validate this assertion and improve the heat transfer coefficient, a nanostructure could be added to the membrane surface to increase roughness and extend the highly wetting regime to higher heat flux. Candidate nanostructures include titanium oxide nanowires, copper oxide and carbon nanotubes.

Measurement accuracy for determining the heat transfer coefficient could be improved using a temperature detector at the membrane surface. A thin film metal RTD on the membrane surface may interfere with evaporation, but an optical technique such as infrared microscopy, thermoreflectance or Raman thermometry could measure the temperature non-invasively. An optical interference technique could also be used to measure the liquid film thickness and liquid area fraction at the surface to confirm the liquid spreading hypothesis.

Suggestions for Enhanced Performance

As discussed in Section 2-1, the optimum pore diameter for 2 µm × 200 µm ridge channels is approximately 30 nm. Furthermore, the optimum pore size is independent of the working fluid used. The critical heat flux for 30 nm pores and 44 nm pitch is 2.83 kW/cm^2 using pentane, 2.1× higher than CHF with 120 nm pores and 200 nm pitch. Additionally, hexagonal arrays of pores will improve the packing density by 15% compared to square arrays resulting in higher heat flux and heat transfer coefficients. Block copolymer lithography is capable of defining periodic hexagonal pore arrays as small as 20 nm diameter, making it a good candidate fabrication technique for increasing performance. Smaller pores will be necessary for the most volatile working fluids which typically have the lowest surface tension, such as R134a ($\sigma = 0.0048$ N/m at 50 °C).

The priming conditions for devices as fabricated depends on the time scale before excess liquid in the vapor channels evaporates. If the time scale is short and heat flux is large, the liquid inside the manifold will boil before thin film evaporation is reached. If the depth of the vapor channels is reduced, the maximum heat flux for priming can be increased. Potentially,

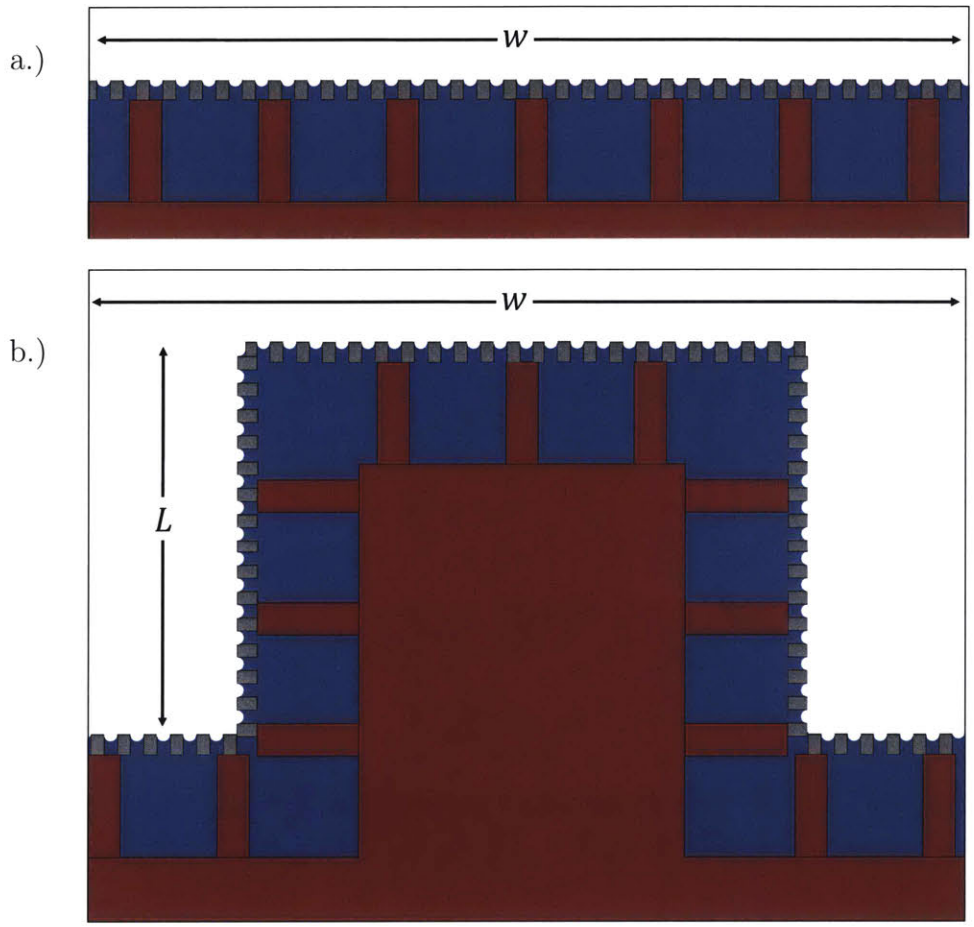

Figure 5-2: a.) As fabricated by fusion bonding, the supported membrane has an interface to heated area ratio of 1:1. b.) If a membrane can be conformally bonded to a ridge support structure, the ratio is increased by $(2L + w)/w$. The extended substrate behaves like a fin to conduct heat to a larger membrane area.

priming will not be necessary for any startup condition.

A minor component of the overall heat transfer coefficient with the fluids tested comes from the conduction resistance in the ridge and membrane structure, representing 6 - 11% of the total thermal resistance. For evaporation with R134a, however, conduction in the ridge and membrane represent 34% of the total thermal resistance. While bulk silicon has a high thermal conductivity, the thermal conductivity of the membrane is assumed to be 7× lower than bulk silicon as a result of phonon scattering. To improve upon the conduction resistance, the membrane and ridges could be fabricated using metals if the metal could be bonded without mechanical instabilities which arise from thermal expansion coefficient mismatch. Metals such as copper, gold and silver have higher intrinsic thermal conductivity that is only limited by electron scattering in structures smaller than 10 nm.

If water has such a high interfacial resistance to evaporation, the question may arise: how

is any phase change heat transfer device capable of reaching 500 W/cm^2 at $\Delta T \approx 50$ K with water, including flow boiling and boiling from wicks? The answer is a combination of sensible liquid cooling and extended surface area. In microchannel flow boiling, the extended surface area refers to the perimeter of a channel cross-section. For a square channel with annular flow, the interfacial area could be up to 4× larger than the heated area. Both q''_{CHF} and h are enhanced as a result of the channel wall behaving like a fin. Likewise during boiling in a sintered copper wick, the interface is extended across a larger surface in the wick. Similar enhancements can be achieved using nanoporous membranes, as shown in Figure 5-2. In the first schematic, the heated area is equal to the membrane area. In the second schematic, showing a unit cell of a fin structure, the membrane area is enhanced by a factor of $w + 2L$. For a fin with $h = 10\,\mu$m, the Biot number is:

$$\mathrm{Bi} = \frac{hL}{k} \tag{5.1}$$

$$= \frac{(10^5\ \mathrm{W/m^2K})(10^{-5}\ \mathrm{m})}{(130\ \mathrm{W/mK})} \tag{5.2}$$

$$= 0.077 \tag{5.3}$$

therefore, the fin efficiency is high and enhancement in q''_{CHF} and overall heat transfer coefficient will be nearly 3× for $w = L = 10\,\mu$m. The challenge to realizing this improvement lies in fabrication of the structure. A more realistic approach would be bottom-up self assembly rather than top-down etching and wafer bonding.

While this thesis demonstrates the feasibility of high heat flux evaporation from nanoporous membranes, there is potential for considerable improvements in critical heat flux, heat transfer coefficient and reliability.

Appendix A

Fluid Properties

A.1 Water

T [°C]	P_{sat} [kPa]	σ [N/m]	h_{fg} [kJ/kg]	ρ_{liq} [kg/m^3]	ρ_{vap} [kg/m^3]	μ_{liq} [µPa s]
0	0.612	0.0756	2501	999.8	0.00485	1791.2
10	1.23	0.0742	2477	999.6	0.00941	1305.6
20	2.34	0.0727	2454	998.2	0.0173	1001.4
30	4.25	0.0712	2430	995.6	0.0304	797.2
40	7.39	0.0696	2406	992.2	0.0513	652.8
50	12.4	0.0679	2382	988.0	0.0832	546.7
60	20.0	0.0662	2358	983.2	0.130	466.3
70	31.2	0.0645	2333	977.7	0.199	403.8
80	47.4	0.0627	2308	971.8	0.294	354.3
90	70.2	0.0608	2282	965.3	0.424	314.4
100	101.	0.0589	2256	958.3	0.598	281.7
110	143.	0.0570	2230	950.9	0.827	254.7
120	199.	0.0550	2202	943.1	1.12	232.0
130	270.	0.0529	2174	934.8	1.50	212.9
140	362.	0.0509	2144	926.1	1.97	196.5
150	476.	0.0487	2114	917.0	2.55	182.4

A.2 Methanol

T [°C]	P_{sat} [kPa]	σ [N/m]	h_{fg} [kJ/kg]	ρ_{liq} [kg/m^3]	ρ_{vap} [kg/m^3]	μ_{liq} [µPa s]
-10	2.1	0.0252	1218.3	819.0	0.03110	931
-5	2.9	0.0248	1211.8	814.3	0.04275	862
0	4.1	0.0243	1205.1	809.6	0.05801	798
5	5.5	0.0239	1198.2	805.0	0.07776	738
10	7.4	0.0235	1191.2	800.3	0.1030	684
15	9.9	0.0231	1183.9	795.6	0.1350	634
20	13.0	0.0227	1176.6	790.9	0.1751	589
25	17.0	0.0223	1169.0	786.2	0.2250	547
30	21.9	0.0218	1161.2	781.5	0.2863	509
35	28.0	0.0214	1153.2	776.8	0.3613	475
40	35.5	0.0210	1145.0	772.1	0.4521	444
45	44.6	0.0206	1136.5	767.3	0.5614	416
50	55.7	0.0202	1127.9	762.5	0.6920	390
55	68.9	0.0198	1118.9	757.7	0.8470	367
60	84.7	0.0193	1109.7	752.8	1.030	346
65	103.4	0.0189	1100.0	747.8	1.245	328
70	125.4	0.0185	1090.2	742.8	1.495	310
75	151.2	0.0180	1079.9	737.7	1.786	294
80	181.1	0.0176	1069.2	732.6	2.123	280
85	215.8	0.0171	1058.2	727.3	2.511	266
90	255.7	0.0167	1046.5	722.0	2.955	253
95	301.5	0.0162	1034.6	716.5	3.463	240
100	353.7	0.0157	1022.0	711.0	4.042	227
105	413.1	0.0152	1009.0	705.3	4.699	214
110	480.2	0.0147	995.3	699.4	5.444	201

A.3 Isopropyl Alchohol

T [°C]	P_{sat} [kPa]	σ [N/m]	h_{fg} [kJ/kg]	ρ_{liq} [kg/m^3]	ρ_{vap} [kg/m^3]	μ_{liq} [µPa s]
-10	0.514	0.0254	795	812	0.0141	6434
-5	0.766	0.0250	790	808	0.0207	5372
0	1.12	0.0246	785	804	0.0297	4514
5	1.62	0.0242	779	799	0.0421	3816
10	2.30	0.0238	774	795	0.0587	3244
15	3.22	0.0234	768	791	0.0808	2772
20	4.44	0.0230	762	786	0.110	2381
25	6.06	0.0226	755	781	0.147	2055
30	8.16	0.0222	749	777	0.195	1782
35	10.9	0.0218	742	772	0.255	1552
40	14.3	0.0214	735	767	0.330	1357
45	18.6	0.0210	727	763	0.423	1192
50	24.0	0.0206	720	758	0.537	1050
55	30.7	0.0202	712	753	0.676	929
60	38.9	0.0198	704	748	0.844	824
65	48.8	0.0194	696	743	1.04	734
70	60.8	0.0191	687	737	1.28	656
75	75.1	0.0187	678	732	1.56	588
80	92.1	0.0183	669	727	1.89	528
85	112.	0.0179	659	721	2.26	121
90	136.	0.0175	649	716	2.70	120
95	163.	0.0171	639	710	3.20	119
100	195.	0.0167	628	704	3.77	118
105	231.	0.0163	617	698	4.42	117
110	273.	0.0159	606	692	5.15	116

A.4 Pentane

T [°C]	P_{sat} [kPa]	σ [N/m]	h_{fg} [kJ/kg]	ρ_{liq} [kg/m^3]	ρ_{vap} [kg/m^3]	μ_{liq} [µPa s]
-20	9.03	0.0205	399	663.4	0.312	332.6
-15	11.8	0.0199	395	658.8	0.400	315.6
-10	15.2	0.0193	392	654.2	0.507	300.0
-5	19.4	0.0188	388	649.6	0.636	285.5
0	24.4	0.0182	385	644.9	0.789	272.2
5	30.6	0.0177	381	640.1	0.972	259.8
10	37.8	0.0171	378	635.4	1.19	248.3
15	46.4	0.0166	374	630.6	1.44	237.4
20	56.6	0.0160	370	625.7	1.72	227.3
25	68.3	0.0155	366	620.8	2.06	217.8
30	82.0	0.0149	362	615.8	2.44	208.8
35	97.7	0.0144	358	610.8	2.88	200.3
40	116.	0.0138	354	605.7	3.37	192.3
45	136.	0.0133	350	600.5	3.93	184.7
50	159.	0.0128	346	595.3	4.55	177.4
55	185.	0.0122	342	590.0	5.26	170.5
60	215.	0.0117	337	584.6	6.04	163.9
65	247.	0.0112	333	579.1	6.91	157.6
70	283.	0.0107	328	573.5	7.88	151.5
75	324.	0.0102	323	567.8	8.96	145.7
80	368.	0.0097	318	562.0	10.1	140.0
85	417.	0.0091	313	556.1	11.5	134.6
90	470.	0.0086	308	550.0	12.9	129.4
95	529.	0.0081	302	543.8	14.5	124.3
100	593.	0.0077	296	537.4	16.2	119.4

A.5 R245fa

T [°C]	P_{sat} [kPa]	σ [N/m]	h_{fg} [kJ/kg]	ρ_{liq} [kg/m^3]	ρ_{vap} [kg/m^3]	μ_{liq} [µPa s]
-20	19.7	0.0198	215.5	1453.3	1.270	786
-15	25.7	0.0192	212.9	1441.2	1.633	721
-10	33.2	0.0185	210.3	1428.9	2.077	665
-5	42.4	0.0179	207.6	1416.6	2.611	615
0	53.6	0.0173	204.9	1404.0	3.251	570
5	67.0	0.0166	202.2	1391.4	4.010	530
10	82.9	0.0160	199.4	1378.5	4.903	494
15	101.8	0.0153	196.6	1365.5	5.946	462
20	123.8	0.0147	193.8	1352.2	7.157	432
25	149.4	0.0140	190.9	1338.8	8.555	405
30	179.0	0.0134	187.9	1325.1	10.16	381
35	213.0	0.0128	184.8	1311.2	11.99	358
40	251.8	0.0121	181.7	1297.0	14.08	337
45	295.8	0.0115	178.6	1282.5	16.44	317
50	345.4	0.0109	175.3	1267.7	19.11	299
55	401.2	0.0102	171.9	1252.5	22.12	282
60	463.5	0.0096	168.4	1237.0	25.50	266
65	533.0	0.0090	164.8	1221.1	29.29	250
70	610.0	0.0083	161.1	1204.7	33.53	236
75	695.1	0.0077	157.3	1187.7	38.27	223
80	788.8	0.0071	153.3	1170.3	43.57	210
85	891.7	0.0065	149.1	1152.1	49.50	198
90	1004.4	0.0059	144.8	1133.3	56.13	186
95	1127.4	0.0054	140.2	1113.7	63.56	175
100	1261.4	0.0048	135.5	1093.1	71.89	165

Appendix B

Labview Code

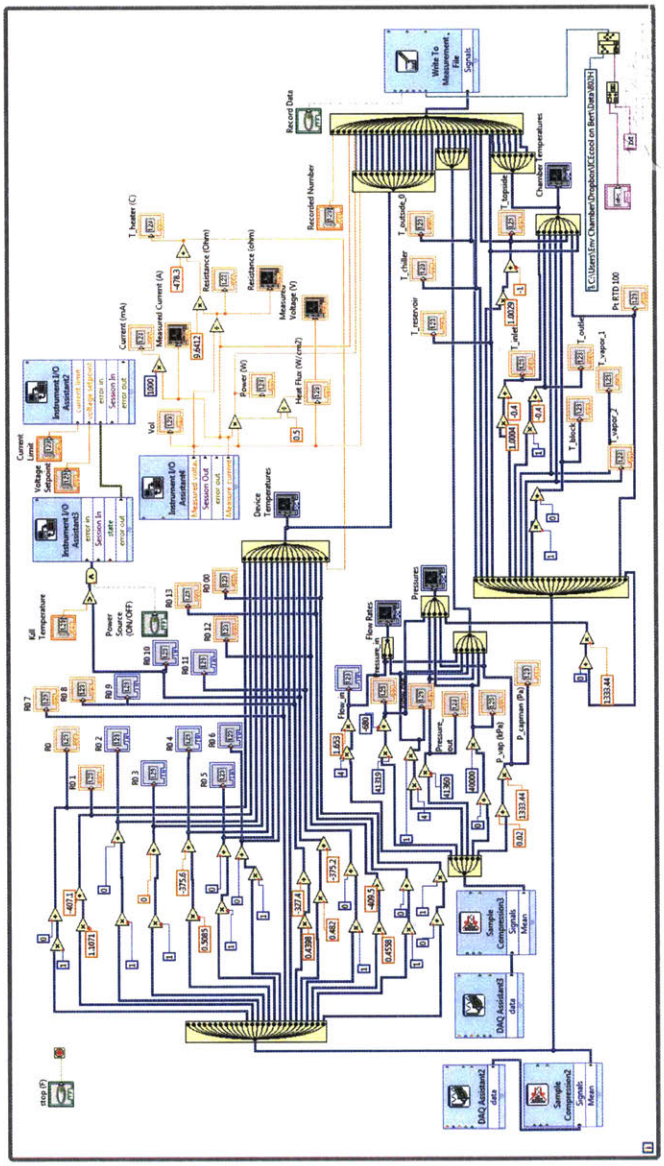

Bibliography

[1] U. K. Mishra, L. Shen, T. E. Kazior, and Y. F. Wu. Gan-based rf power devices and amplifiers. *Proceedings of the IEEE*, 96(2):287–305, Feb 2008.

[2] RJ Trew, MW Shin, and V Gatto. High power applications for gan-based devices. *Solid-State Electronics*, 41(10):1561–1567, 1997.

[3] Y. f. Wu, M. Moore, A. Saxler, T. Wisleder, and P. Parikh. 40-w/mm double field-plated gan hemts. In *Device Research Conference, 2006 64th*, pages 151–152, June 2006.

[4] Zhengmao Lu, Todd Salamon, Shankar Narayanan, Kevin Bagnall, Daniel Hanks, Dion Antao, Banafsheh Barabadi, Jay Sircar, Maria E. Simon, and Evelyn N Wang. Design and modeling of membrane-based evaporative cooling devices for thermal management of high heat fluxes. *IEEE Transactions on Components, Packaging and Manufacturing Technology.*

[5] Kevin Robert Bagnall. *Device-level thermal analysis of GaN-based electronics.* PhD thesis, Massachusetts Institute of Technology, 2013.

[6] Avram Bar-Cohen. Broad agency announcement: Intrachip/interchip enhanced cooling fundamentals. *Microsystems Technology Office*, 2012. DARPA-BAA-12-50.

[7] Avram Bar-Cohen[1], Joseph J Maurer, and Jonathan G Felbinger. DARPAs intra/interchip enhanced cooling (icecool) program. In *CS MANTECH Conference, May 13th-16th*, 2013.

[8] Warren M Rohsenow. A method of correlating heat transfer data for surface boiling of liquids. 74:969–976, 1952.

[9] Poh-Seng Lee and Suresh V. Garimella. Saturated flow boiling heat transfer and pressure drop in silicon microchannel arrays. *International Journal of Heat and Mass Transfer*, 51(34):789 – 806, 2008.

[10] Issam Mudawar. Assessment of high-heat-flux thermal management schemes. *Components and Packaging Technologies, IEEE Transactions on*, 24(2):122–141, 2001.

[11] MB Bowers and I Mudawar. High flux boiling in low flow rate, low pressure drop mini-channel and micro-channel heat sinks. *International Journal of Heat and Mass Transfer*, 37(2):321–332, 1994.

[12] XF Peng and B-X Wang. Forced convection and flow boiling heat transfer for liquid flowing through microchannels. *International Journal of Heat and Mass Transfer*, 36(14):3421–3427, 1993.

[13] Mark E Steinke and Satish G Kandlikar. An experimental investigation of flow boiling characteristics of water in parallel microchannels. *Journal of Heat Transfer*, 126(4):518–526, 2004.

[14] Jaeseon Lee and Issam Mudawar. Two-phase flow in high-heat-flux micro-channel heat sink for refrigeration cooling applications: Part iiheat transfer characteristics. *International Journal of Heat and Mass Transfer*, 48(5):941–955, 2005.

[15] Avram Bar-Cohen, Jessica R Sheehan, and Emil Rahim. Two-phase thermal transport in microgap channelstheory, experimental results, and predictive relations. *Microgravity Science and Technology*, 24(1):1–15, 2012.

[16] Shou-Shing Hsieh and Chih-Yi Lin. Subcooled convective boiling in structured surface microchannels. *Journal of Micromechanics and Microengineering*, 20(1):015027, 2009.

[17] Ali Koşar, Chih-Jung Kuo, and Yoav Peles. Suppression of boiling flow oscillations in parallel microchannels by inlet restrictors. *Journal of Heat Transfer*, 128(3):251–260, 2006.

[18] David B Tuckerman and RFW Pease. High-performance heat sinking for vlsi. *Electron Device Letters, IEEE*, 2(5):126–129, 1981.

[19] Sungwon S Kim, Justin A Weibel, Timothy S Fisher, and Suresh V Garimella. Thermal performance of carbon nanotube enhanced vapor chamber wicks. In *2010 14th International Heat Transfer Conference*, pages 417–424. American Society of Mechanical Engineers, 2010.

[20] Changsong Ding, Gaurav Soni, Payam Bozorgi, Brian D Piorek, Carl D Meinhart, and Noel C MacDonald. A flat heat pipe architecture based on nanostructured titania. *Microelectromechanical Systems, Journal of*, 19(4):878–884, 2010.

[21] Youngsuk Nam, Stephen Sharratt, Gilhwan Cha, and Y Sungtaek Ju. Characterization and modeling of the heat transfer performance of nanostructured cu micropost wicks. *Journal of Heat Transfer*, 133(10):101502, 2011.

[22] Justin A Weibel, Suresh V Garimella, and Mark T North. Characterization of evaporation and boiling from sintered powder wicks fed by capillary action. *International Journal of Heat and Mass Transfer*, 53(19):4204–4215, 2010.

[23] JW Palko, C Zhang, JD Wilbur, TJ Dusseault, M Asheghi, KE Goodson, and JG Santiago. Approaching the limits of two-phase boiling heat transfer: High heat flux and low superheat. *Applied Physics Letters*, 107(25):253903, 2015.

[24] GS Hwang, Y Nam, E Fleming, P Dussinger, YS Ju, and M Kaviany. Multi-artery heat pipe spreader: experiment. *International Journal of Heat and Mass Transfer*, 53(13):2662–2669, 2010.

[25] Dušan Ćoso, Vinod Srinivasan, Ming-Chang Lu, Je-Young Chang, and Arun Majumdar. Enhanced heat transfer in biporous wicks in the thin liquid film evaporation and boiling regimes. *Journal of Heat Transfer*, 134(10):101501, 2012.

[26] Qingjun Cai and Chung-Lung Chen. Design and test of carbon nanotube biwick structure for high-heat-flux phase change heat transfer. *Journal of Heat Transfer*, 132(5):052403, 2010.

[27] John G Collier and John R Thome. *Convective boiling and condensation.* Clarendon Press, 1994.

[28] Rong Xiao, Shalabh C Maroo, and Evelyn N Wang. Negative pressures in nanoporous membranes for thin film evaporation. *Applied Physics Letters*, 102(12):123103, 2013.

[29] Hao Wang, Suresh V Garimella, and Jayathi Y Murthy. Characteristics of an evaporating thin film in a microchannel. *international journal of heat and mass transfer*, 50(19):3933–3942, 2007.

[30] Daniel F Hanks, Teresa B Peters, John G Brisson, and Evelyn N Wang. Characterization of a condenser for a high performance multi-condenser loop heat pipe. In *ASME 2011 International Mechanical Engineering Congress and Exposition*, pages 147–152. American Society of Mechanical Engineers, 2011.

[31] Zheji Liu and W Soedel. An investigation of compressor slugging problems. In *International Compressor Engineering Conference*, 1994.

[32] Karin Hermansson, Ulf Lindberg, Bertill Hok, and Göran Palmskog. Wetting properties of silicon surfaces. In *Solid-State Sensors and Actuators, 1991. Digest of Technical Papers, TRANSDUCERS'91., 1991 International Conference on*, pages 193–196. IEEE, 1991.

[33] T Liu and CJ Kim. Turning a surface superrepellent even to completely wetting liquids. *Science*, 346(6213), 2014.

[34] Tobias D Wheeler and Abraham D Stroock. The transpiration of water at negative pressures in a synthetic tree. *Nature*, 455(7210):208–212, 2008.

[35] Frédéric Caupin and Eric Herbert. Cavitation in water: a review. *Comptes Rendus Physique*, 7(9):1000–1017, 2006.

[36] YY Hsu. On the size range of active nucleation cavities on a heating surface. *Journal of Heat Transfer*, 84(3):207–213, 1962.

[37] Amir Faghri. *Heat pipe science and technology*. Global Digital Press, 1995.

[38] Jeremy A Johnson, AA Maznev, John Cuffe, Jeffrey K Eliason, Austin J Minnich, Timothy Kehoe, Clivia M Sotomayor Torres, Gang Chen, and Keith A Nelson. Direct measurement of room-temperature nondiffusive thermal transport over micron distances in a silicon membrane. *Physical review letters*, 110(2):025901, 2013.

[39] Jinyao Tang, Hung-Ta Wang, Dong Hyun Lee, Melissa Fardy, Ziyang Huo, Thomas P Russell, and Peidong Yang. Holey silicon as an efficient thermoelectric material. *Nano letters*, 10(10):4279–4283, 2010.

[40] Patrick E Hopkins, Charles M Reinke, Mehmet F Su, Roy H Olsson III, Eric A Shaner, Zayd C Leseman, Justin R Serrano, Leslie M Phinney, and Ihab El-Kady. Reduction in the thermal conductivity of single crystalline silicon by phononic crystal patterning. *Nano letters*, 11(1):107–112, 2010.

[41] DA Labuntsov and AP Kryukov. Analysis of intensive evaporation and condensation. *International Journal of Heat and Mass Transfer*, 22(7):989–1002, 1979.

[42] Zhengmao Lu, Shankar Narayanan, and Evelyn N Wang. Modeling of evaporation from nanopores with nonequilibrium and nonlocal effects. *Langmuir*, 31(36):9817–9824, 2015.

[43] R Marek and J Straub. Analysis of the evaporation coefficient and the condensation coefficient of water. *International Journal of Heat and Mass Transfer*, 44(1):39–53, 2001.

[44] Michael H Rausch, Lorenz Kretschmer, Stefan Will, Alfred Leipertz, and Andreas P Froba. Density, surface tension, and kinematic viscosity of hydrofluoroethers hfe-7000, hfe-7100, hfe-7200, hfe-7300, and hfe-7500. *Journal of Chemical & Engineering Data*, 60(12):3759–3765, 2015.

[45] E.W. Lemmon, M.O. McLinden, and D.G. Friend. Thermophysical properties of fluid systems. In P.J. Linstrom and W.G. Mallard, editors, *NIST Chemistry WebBook*, NIST Standard Reference Database Number 69, chapter 15. National Institute of Standards and Technology, Gaithersburg MD, 20899, 2016.

[46] Miri Park, Christopher Harrison, Paul M Chaikin, Richard A Register, and Douglas H Adamson. Block copolymer lithography: periodic arrays of~ 1011 holes in 1 square centimeter. *Science*, 276(5317):1401–1404, 1997.

[47] Tsutomu Sato, Ichiro Mizushima, Shuichi Taniguchi, Keiichi Takenaka, Satoshi Shimonishi, Hisataka Hayashi, Masayuki Hatano, Kazuyoshi Sugihara, and Yoshitaka Tsunashima. Fabrication of silicon-on-nothing structure by substrate engineering using the empty-space-in-silicon formation technique. *Japanese Journal of Applied Physics*, 43(1R):12, 2004.

[48] I Mizushima, T Sato, S Taniguchi, and Y Tsunashima. Empty-space-in-silicon technique for fabricating a silicon-on-nothing structure. *Applied Physics Letters*, 77(20):3290–3292, 2000.

[49] James R Black. Electromigrationa brief survey and some recent results. *Electron Devices, IEEE Transactions on*, 16(4):338–347, 1969.

[50] Michael DiBattista and Johannes W Schwank. Determination of diffusion in polycrystalline platinum thin films. *Journal of applied physics*, 86(9):4902–4907, 1999.

[51] JM Carter, RC Fleming, TA Savas, ME Walsh, TB OReilly, ML Schattenburg, and HI Smith. Interference lithography. *MTL Annual report*, 2003:186–188, 2003.

[52] Pedro Cuatrecasas, Meir Wilchek, and Christian B Anfinsen. Selective enzyme purification by affinity chromatography. *Proceedings of the National Academy of Sciences*, 61(2):636–643, 1968.

[53] Anthony F Mills. *Basic heat and mass transfer*. Pearson College Div, 1999.

[54] Edward Lansing Cussler. *Diffusion: mass transfer in fluid systems*. Cambridge university press, 2009.

[55] R Byron Bird. Transport phenomena. *Applied Mechanics Reviews*, 55(1):R1–R4, 2002.

[56] Shankar Narayanan, Andrei G Fedorov, and Yogendra K Joshi. Gas-assisted thin-film evaporation from confined spaces for dissipation of high heat fluxes. *Nanoscale and Microscale Thermophysical Engineering*, 13(1):30–53, 2009.

[57] Mark Rosker, Christopher Bozada, Harry Dietrich, Alfred Hung, Dave Via, Steve Binari, Ed Vivierios, Eliot Cohen, and Justin Hodiak. The DARPA wide band gap semiconductors for rf applications (wbgs-rf) program: Phase ii results. *CS ManTech*, 2009.